SPARSE LAGRANGIAN MMC-LES COMBUSTION MODELLING OF LIQUID SPRAYS

BY

NAZMUL KHAN

A THESIS SUBMITTED IN FULFILLMENT OF THE REQUIREMENTS OF FOR THE DEGREE OF DOCTOR OF PHILOSOPHY

THE UNIVERSITY OF SYDNEY, AUSTRALIA

Authorship attribution statement

As a part of this study, some of the contents of this thesis has been presented in conferences.

The relevant papers are:

1. Khan, M., Cleary, M. (2017). Sparse-Lagrangian MMC-LES Modelling of Liquid Sprays. Combustion and Flame (In preparation) ....Contents of thesis Chapter 5, 6 and 7.

   • Author's contribution: 70%

2. Khan, M., Cleary, M. (2017). Sparse-Lagrangian MMC-LES Modelling of Reacting Acetone Spray. 11th Asia-Pacific Conference on Combustion, Sydney, New South Wales, Australia.The University of Sydney, NSW Australia (submitted) ... Contents of thesis Chapter 7.

   • Author's contribution: 70%

3. Khan, M., Cleary, M. (2015). Large Eddy Simulation of Evaporating Acetone in a Turbulent Multiphase Flow. Australian Combustion Symposium 2015, Melbourne, Victoria: The Combustion Institute Australia and New Zealand. ....Contents of thesis Chapter 6.

- Author's contribution: 70%

4. Khan, M., Zhao, L., Cleary, M., Bilger, R., Stein, O., Kronenburg, A. (2014). A Mixture Fraction-Based Model for Evaporation, Pyrolysis and Char Conversion of Dilute Fuel Dispersions. 19th Australasian Fluid Mechanics Conference, Melbourne: RMIT University.....Contents of thesis Chapter 5.

   - Author's contribution: 50%

As supervisor for the candidature upon which this thesis is based, I can confirm that the authorship attribution statements above are correct.

Supervisor Name : Matthew Cleary

Statement of originality

I hereby declare that this submission is my own work and to the best of my knowledge it contains no materials previously published or written by another person, or substantial proportions of material which have been accepted for the award of any other degree or diploma at University of Sydney or any other institution, except where due acknowledgement is made in the thesis. Any contribution made to the research by others, with whom I have worked at the University of Sydney or elsewhere, is explicitly acknowledged in the thesis. I also declare that the intellectual content of this thesis is the product of my own work, except to the extent that assistance from others in the project's design and conception or style, presentation, and linguistic expression is acknowledged.

Nazmul Khan
December 12, 2017

Acknowledgments

I would like to acknowledge my supervisor Dr Matthew Cleary. Matthew has given a lot of his valuable time to the OpenFOAM coding. I would like to express my sincerest appreciation to Matthew for his kind guidance, encouragement and every support during this project's progression.

I would also like to thank my friend and fellow student Longfei Zhao. Since the beginning of our candidature, his friendship and support have made this time for both of us rewarding and enjoyable. Our conversations in code development has been very productive and a fruitful contribution in our works. The proof reading and editorial assistance provided by Trigger Wise, Sydney University, is gratefully acknowledged.

I am grateful to my family members for providing me mental support all the time otherwise it would not have been possible for me to finish my study.

Finally, I acknowledge the financial support of the Australian Research Council, the University of Sydney and the School of Aerospace, Mechanical and Mechatronic Engineering.

Nazmul Khan
December 12, 2017

Summary

This thesis provides a detailed investigation of turbulent combustion modelling of liquid sprays. Modelling of liquid sprays is a challenging task due to the existence of a wide range of complexities in both liquid and gas phases and their interaction in the spray and combustion process. In such multiphase flow, there is a need to address all physical processes involved in each individual phase and jointly in the interaction of phases. In a multiphase flow, there are physical processes with respect to flow, energy, chemical reactions, and flame propagation. In the liquid phase, the physical processes include dispersion, evaporation, volatile formation and exchange of heat and mass transfer with the gas phase. In the gas phase, there is turbulent flow, mixing and chemical reactions. The model that is derived and validated in this thesis extends the existing capabilities of liquid spray modelling by introducing a novel model for heat and mass transfer in the liquid phase that is coupled with the gas phase simulation. In this study, a mixture fraction based modelling approach is applied for both gas and liquid phases to address those complex processes in a single LES computational framework. This sparse Lagrangian MMC-LES model combines the advantage of detailed flow field description in LES with accurate, yet computationally affordable, turbulent chemistry interaction. The model is comprised of an Eulerian LES model for the gas phase mass, momentum, and reference mixture

fraction, a Lagrangian fuel particle (LFP) model for the dispersion, evaporation, heat and mass transfer and volatile formation, and a second Lagrangian stochastic particle model based on a multiple mapping conditioning (MMC) to represent the turbulent reacting chemistry. The coupling between LES, MMC, and LFP is done elegantly following the OpenFOAM coding style, which is a robust numerical tool in simulating combustion modelling of liquid sprays.

This study simulates three experimental validation cases from the University of Sydney combustion lab: non-reacting kerosene, evaporating acetone and reacting acetone [1]. The dispersion of liquid fuel particle is studied in the non-reacting kerosene cases, where the LES and Lagrangian fuel particle simulation results are found in good agreement with experimental data for both axial and radial velocity profiles. The second simulation is conducted for evaporating acetone cases, where the results also show good agreement with experimental data. The evaporating acetone cases are also tested for liquid flow rate, which qualitatively matches experimental measurement. The simulation is then applied for the reacting acetone cases. The axial and radial profiles of droplets, gas velocity and gas phase temperature are in good agreement with experimental measurements. Importantly the results of the finite volume and Lagrangian stochastic particle schemes are shown to be consistent with each other.

Nomenclature

Abbreviations

CFD computational Fluid Dynamics

CMC conditional moment closure

DNS direct numerical simulation

EBU eddy break up model

EDM eddy dissipation model

FDF filtered density functions

LES large eddy simulations

LFP Lagrangian fuel particle

MMC multiple mapping conditioning

PDF probability density functions

PSIC particle source in cell

RANS Reynolds-averaged Navier-Stokes

RMS root mean square

Greek symbols

α thermal diffusivity

β conserved scalar or constant

δ_H characteristic thickness layer

ϵ turbulence Kinetic energy dissipation rate

γ level set function

ν kinematic viscosity

Ω weights for stochastic particle

ω rotational rate tensor

θ phase indicator

ρ density

$\bar{\rho}$ Mean density

σ Stephan-Boltzman constant

τ_η Kolmogorov time scale

$\tau_{i,j}$ viscous stress tensor

τ_G^{eu} Eulerian timescale

τ^{fp} relaxation timescale for fuel particle

τ_G^{sp} mixing timescale for stochastic particle

τ_N subfilter dissipation time scale

ς fine grained density

$\bar{\varphi}$ filtered mean

ξ The LES reference mixture fraction (model equations)

Miscellaneous symbols

B_H Spalding tranfer number for heat transfer

B_M Spalding trasnfer number for mass transfer

$\mathscr{D}$ diffusivity

Ka Karlovitz number

Le Lewis number

MW_{air} molecular weight of air

MW_α molecular weight of species

Nu Nusselt number

Pr Prandle number

Re Reynolds number

Sc Schmidt number

Sh Sherwood number

St Stokes number

Normal symbols

I ignition

Q quenching

Operators

$\bar{op}$ LES spatial filtering

$\Delta_v.$ divergence operator with respect to velocity components

$\dot{op}$ time derivative, $\partial/\partial t$

$\langle\rangle$ expected value

$\langle|\rangle$ conditional average

$\sum$ summation

$\widetilde{op}$ density-weighted Favre filtering

Roman symbols

A Area

a acceleration by the other phase

A, B chemical reactants

C_d^{fp} drag coefficient for spherical particles

C, D chemical products

C_{EBU} EBU constant

C_m constant

$C_{p,D}$ specific heat of liquid fuel particle

U Droplet Velocity

Δ filter width

D^{fp} fuel particle diameter

D_f fractal dimension

D jet diameter

Δ_L length scale to the nearest particle

dm^{sp} change of mass in stohcatic particles due to gas production

d inter-droplet separation

$\mathscr{D}_t$ turbulent diffusivity

E_a activation energy

F Fuel species

f The LES reference mixture fraction (for results and analysis)

A_f fractal area

f_m The characteristic distance of particles in mixture fraction space

G LES filtering karnel

G	group combustion or Kernel function
g_i	gravity vector
$\hat{h}$	specific enthalpy
$\hat{h}_D$	enthalpy of dispersed phase
$\hat{h}_G$	enthalpy of gas phase
$\hat{h}_S$	enthalpy of surface state
H	heaviside function
h_f^r	reference enthalpy of formation
$J_{\alpha,i}$	mass diffusion
$J_{h,i}$	heat diffusion
$k(T)$	biomolecular reaction rate
L	fuel particle length scale
l_f	isoscalar surface thickness
l_k	Kolmogorov length scale
l_λ	Taylor micro-scale
l_m	macro-scale
l_T	turbulent integral legnth scale
$\dot{m}''$	mass flux

n	surface normal vector pointing from phase 1 into phase 2
n_s	number of species
OX	Oxidizer
Π	transfer rate
p, q	mixing particles
P	pressure
Ψ	sample space for the reactive species field Y
$\dot{Q}''$	heat flux
$\dot{Q}_D$	total heat flux
q_D	internal heating
$\dot{Q}_R$	total radiation heat
q_R	radiation heat transfer rate
R	gas constant
r_i	charateristic mixing distance in each spatial direction
r_m	Physical distance of stochastic particles
P_α	vapour pressrue of evaporative species
S	Oxygen-fuel stoichiometric mass fraction ratio or nondimensional separation distance

S_L laminar burning velocity

$\dot{S}$ differetn source terms

T temperature

T_r reference temperature

T_D temperature of dispersed phase

T_G temperature of gas phase

T_S surface temperature

T_w temprature of wall

$\widetilde{u}$ velocity vector

u' velocity fluctuation

u_η Kolmogorov velocity

$u_x(0)'$ fluctuating velocities

V volume

V^{eu} filtered volume

v_m volume of mixing particles

W RMS velocity

W_α reaction rate of species

W_h radiation transer rate

ξ_{jet} jet mixture fraction

Y species composition

Z exponent of internal heat equation

z Stochastic particle mixture fraction

Subscripts

α species index

e Eulerian index

i, j direction indices

k phase index

r turbulent (viscosity/diffusivity)

sc supercell

D dispersed phase

G gas phase

S surface state

Superscripts

eu Eulerian index

fp fuel particle index

sgs subgrid scale

sp stochastic index

I interface

Table of contents

List of Figures

List of Tables

Chapter 1

Introduction

1.1 Motivation

Energy demand is increasing with the advent of new technology and lavish modern life. The conventional energy sources are oil, coal, natural gas, hydro, nuclear and some renewable. The contribution of liquid fuel is the single largest among all types of sources of fuel [3]. Liquid fuels are used in many engineering devices for transportation, power generation, aviation industries and in many other industry applications. According to world energy consumption scenarios published by BP Statistical review [3], the contribution of oil is increasing with the increased demand of energy in the market. The consumption of liquid fuel will continue to grow in future as there is no immediate alternative yet in the market. Figure 1.1 shows the energy consumption pattern of nearly the last 50 years' statistics, where oil source maintains most contribution in the energy market. On the other hand, combustion of liquid fuels produces various harmful pollutants, such as CO2, NOx, SOx gases and particulate objects. These pollutants are a

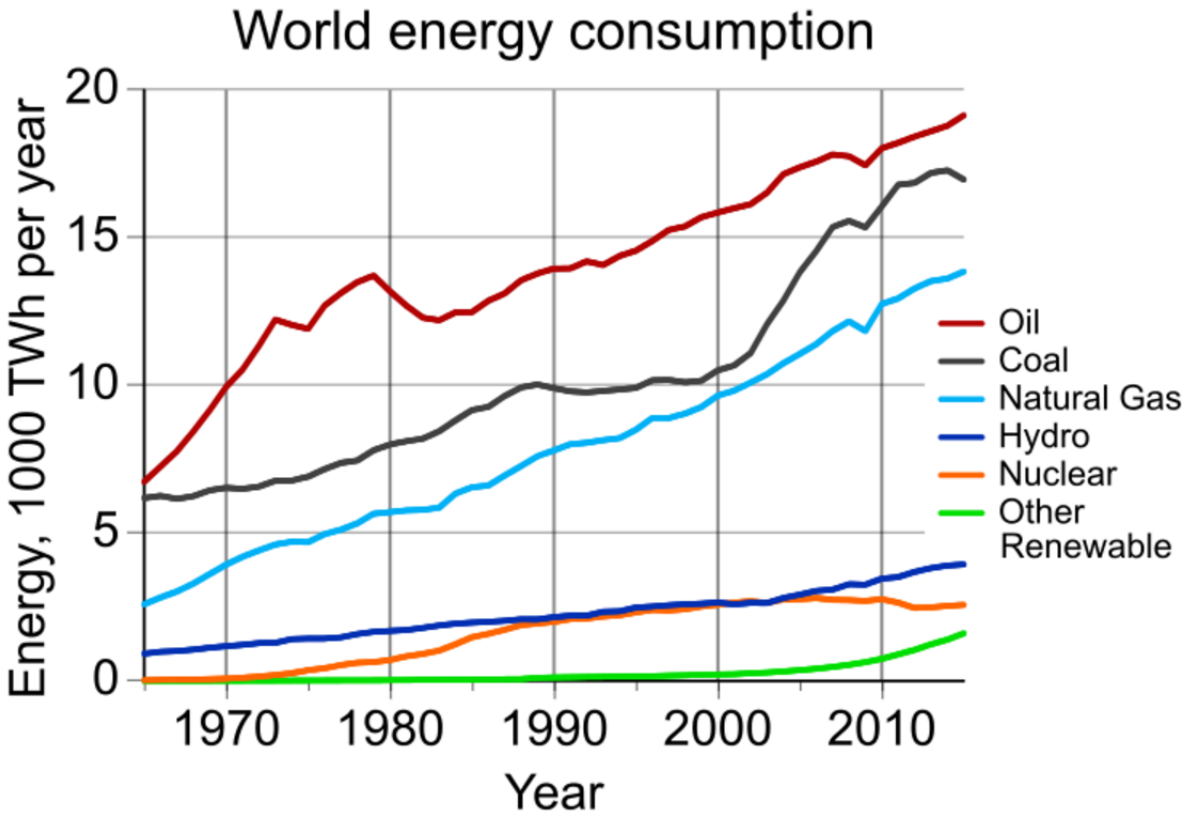

Figure 1.1: World Energy Consumption scenarios - [3].

threat to the environment and human health. In order to avoid worsening local pollution, it is necessary to understand the combustion process and pollution contribution of various liquid fuels. Moreover, there is rising concern about environmental pollution, and political motivation to use clean energy for sustainable development. There is a need to design modern devices to optimise combustion and minimise pollution. However, combustion of liquid fuel is not fully understood by the research community due to the complex physics of droplet dynamics and the combustion process [4]. Turbulent combustion modelling of gaseous fuels is relatively mature [5] comparing to liquid fuels. Combustion of liquid fuels is complex due to droplet dynamics, turbulent flow, the existence of multiple phases and chemical kinetics.

The evolution of combustion technology has a long history of gradual improvement

of devices and methods for burning fuels to meet the specific energy demand. In this process, scientific research has played an important role in characterising different combustion processes. Combustion is a complex process involving a broad range of disciplines. At the centre of the challenge is the presence of a broad range of length and time scales. These scales are spanned by various processes governing combustion and the degree of coupling between these processes across all scales [6]. The conventional fluid dynamics theory follows the Navier-Stokes equations, which are based on convective and diffusive transport phenomena. Computational fluid dynamics has made impressive progress in the last decade in the field of turbulent combustion modelling for both premixed and non-premixed combustion by applying those numerical methods [7]. However, their continues to be suboptimal accuracy of turbulence models, particularly for two-phase combusting flows, and more research is required to improve their practical implementations. The multiphase flow will experience the following processes: atomisation and dispersion, vaporisation, de-volatilisation and heterogeneous and homogeneous combustion. However, the turbulent combustion modelling of such multiphase fuels is still to be fully explored properly.

This study will follow the pathway to developing a more comprehensive multiphase combustion model addressing the key issues of multiple scales of turbulent flow, mixing, phase interaction and chemical kinetics using a computational fluid dynamics (CFD) model. The main objective of this study is to develop a robust numerical model so as to implement multiphase combustion modelling of liquid fuels. To be more specific, this study would implement the following objectives:

(i) Develop a multiphase combustion model for liquid spray using a probabilistic

approach based on sparse MMC-LES.

(ii) Validate the developed combustion model against experimental data for non-reacting kerosene, evaporating and reacting acetone cases of Sydney University.

(iii) Test the sensitivity of the model for different numbers of particles in both stochastic and liquid fuel, different evaporation rates and different input parameters of MMC models.

(iv) Make recommendations for further improvement of this liquid spray model toward the modelling of multi-components fuels.

1.2 Background

Combustion is an important part of modern scientific life where the use of energy in different devices has created an avenue for research and development of multiple modes of flow and combustion chemistry. The research community in the last few decades or more has made an enormous contribution towards developing energy efficient and sophisticated devices high performing applications used by normal industries through to the advanced aviation industry. In this journey the research community was involved in both experimental and computational studies to contribute to the research and development. These experimental and computational studies have improved remarkably in the last few decades due to the improvement of the computational power of the computer and the use of modern experimental techniques (e.g. laser diagnostics) for understanding the complex science of combustion. In this section, the state of the art of up-to-date research

development in the field of combustion is reviewed starting from simple governing equations to complex implementations of modelling strategies.

1.2.1 Turbulent flow

Turbulent flow is defined by a range of characteristic scales. In turbulent flow, small scale, the chaotic nature of the fluid flow is influenced by low momentum diffusion, high momentum convection and rapid change of pressure variation and flow velocity. The unsteady turbulent flow creates vortices in many scales which interact with each other. The formation of different eddies can be explained by the energy cascade phenomenon as the kinetic energy is dissipated into internal energy by viscous shear stress from large-scale to small-scale. The large-scale structures contain most of the energy compared to small-scale eddies and the turbulent flow can be explained as a superposition of spectrum of flow velocity fluctuations and eddies on mean flow velocity. The eddies can be divided into different scales based on the energy spectrum that measures the energy on the flow velocity fluctuations for each wave number. These eddies can be written as decreasing in order as follows:

1.2.1.1 Macroscale (l_m)

The macroscale or characteristic width of flow is the largest possible length scale and is defined by the actual size of the model or device under consideration.

1.2.1.2 Integral scale (l_T)

The integral scale represents the mean size of the large eddies in a turbulent flow. These eddies have low frequency, large wavelength, and large velocity fluctuation. The integral scale is always smaller than the macroscale but is of the same order of magnitude. The integral scales can be calculated [8] by integrating the correlation coefficient for the fluctuating velocities as a function of the distance between two points as,

$$l_T = \int_0^\infty R_x(r)dr \tag{1.1}$$

where

$$R_x(r) = \frac{\overline{v'_x(0)v'_x(r)}}{v'_{x,rms}(0)v'_{x,rms}(r)} \tag{1.2}$$

where $v_x(0)'$ and $v_x(r)'$ are the fluctuating velocities.

1.2.1.3 Taylor microscale (l_λ)

The Taylor microscale is the intermediate length scale between integral and Kolmogorov but is weighted towards the smaller scales. This scale is expressed [9] as mean rate of strain as,

$$l_\lambda = \frac{v'_{x,rms}}{\left[\overline{(\frac{\partial v_x}{\partial_x})^2}\right]^{1/2}} \tag{1.3}$$

where the denominator in the above equation represents the mean strain rate.

1.2.1.4 Kolmogorov microscale (l_k)

The Kolmogorov microscale is the smallest length scale in turbulent flows at which viscosity dominates and turbulent kinetic energy is dissipated into heat [10, 11]. This

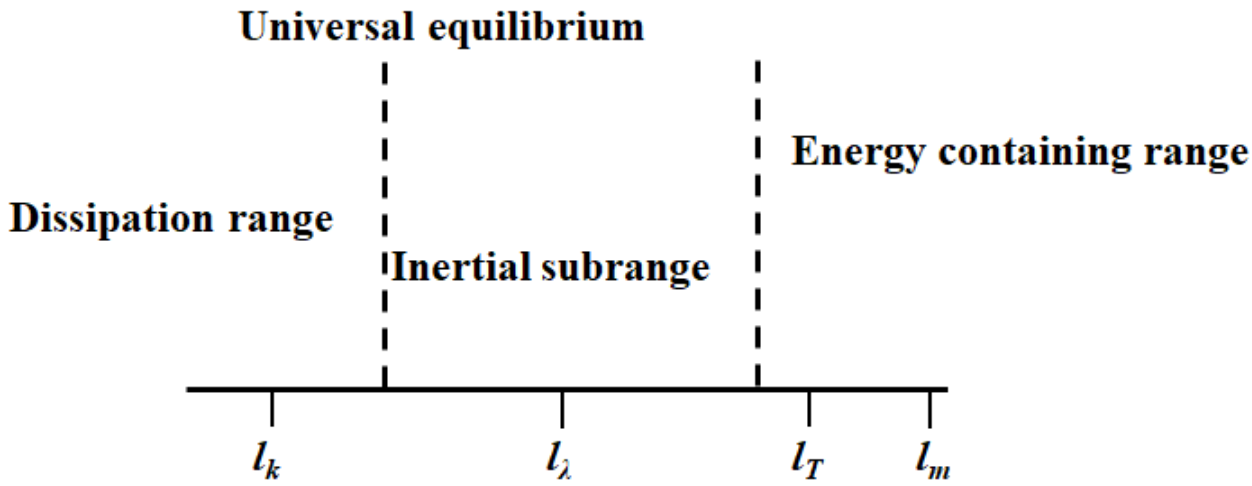

Figure 1.2: Turbulent length-scales [12].

allows for scaling laws or scale invariance in the inertial subrange. The Kolmogorov length, velocity and time scale is defined by

$$l_k = \left(\frac{\nu^3}{\epsilon}\right)^{\frac{1}{4}} \tag{1.4}$$

$$u_\eta = (\epsilon\nu)^{1/4} \tag{1.5}$$

$$\tau_\eta = \left(\frac{\nu}{\epsilon}\right)^{\frac{1}{2}} \tag{1.6}$$

where ν is kinematic viscosity and ϵ is the kinetic energy dissipation rate of turbulence flow. For high Reynolds number flows, the eddy cascade hypothesis, Kolmogorov's similarity laws, and dimensional analysis form the basis for closure of turbulence models. Figure 1.2 illustrates the relationship between the four scales. As combustion involves a large number of chemical reactions which can occur on different time scales to turbulence, the process is further complicated. If all chemical time-scales interacted with all time scales within the inertial range, no simple scaling laws could be found. However, there are still remaining a few cases where both chemical and turbulent time scales interact in

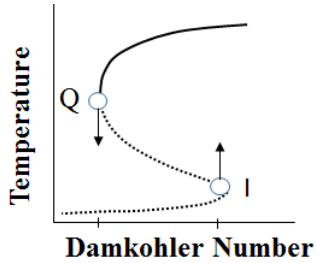

Figure 1.3: Showing maximum temperature as a function of Damkohler number, where dashed lines between Q(quenching) and I(ignition) is unstable [12].

the inertial subrange.

Typical combustion phenomena such as ignition and extinction are illustrated in the S-shaped curve in Figure 1.3. The figure shows maximum temperature in a perfectly stirred reactor plotted as a function of the Damkohler number, which represents the ratio of mixing time to chemical time scales. Chemical reactions on the upper branch occur at high temperature near equilibrium and are fast compared to all turbulent time scales. They concentrate in those layers smaller than the Kolmogorov scale. The fast reactions do not influence inertial range scaling. If temperature decreases then the lower branch of the curve close to the non-reacting state is accessed. Chemistry becomes slower and mixing can be described by classical inertial range scaling. The dashed middle branch between quenching (Q) and ignition (I) states is unstable and the probability of finding realisations here is small [13]. Turbulence increases mixing which enhances reactions and combustion, in turn, releases heat and generates flow instability by buoyancy and gas expansion. There are two classes of flames which are related to the mixedness of the reactants - premixed and non-premixed. In a premixed flame, fuel and oxidizer are mixed at the molecular level prior to the occurrence of any significant chemical reaction, whereas non-premixed combustion occurs when the fuel and oxidizer are injected separately into the combustor, and experience simultaneous mixing and burning. However, in practice,

both premixed and non-premixed flames exist together in a combustor.

1.2.2 Turbulent combustion

Turbulent takes place in almost all practical combustion devices. Numerical Modelling of turbulent combustion is always a challenging task as it needs in-depth understanding of a set of well defined and spatially resolved forms of conservation equations for continuity, momentum, and species. These are common forms of equations, which need modifications or additions of some source terms to address specific features of different flames. Modelling of unclosed source terms introduces another layer of complexity in the solution process and their coupling with the various forms of models. For combustion of liquid fuels, evaporation and radiation processes need to be modelled for a realistic turbulent combustion model. Numerical cost is also an important matter for choosing the right modelling schemes for grid and subgrid fields. Research activities on various platforms, such as DNS, RANS, and LES are aimed based on the optimisation of numerical cost and accuracy. Moreover, grid and subgrid models have many issues with respect to coupling between them for the accuracy of the overall analysis. Bilger *et al.* [5] reviewed various paradigms of turbulent combustion modelling techniques. A radical shift in these paradigms is the separation of scales for grid and subgrid models to overcome the complexity of multi-scale turbulent combustion. Bilger *et al.* [5] also identified recent trends in turbulent combustion modelling, which are motivated by the need to include finite-rate chemistry and non-equilibrium chemistry effects. The importance of a chemistry model in turbulent combustion simulation is also remarkable since the work of Libby and Williams [14]. LES modelling framework over conventional

RANS is also inspiring for many modellers for solving momentum and species transport equations and has become a viable framework in the 1980s. LES has been applied successfully in many practical combustion devices [15] incorporating unsteady flow effects. In this subsection, a comprehensive discussion is attempted to review the up-to-date development of turbulent combustion modelling and strategies adopted by researchers.

1.2.2.1 Governing equations

The numerical simulation of turbulent combustion flows is based on the solution of a set of governing equations expressed in different forms. They are represented by transport equations for continuity, momentum, and other equations for different scalars. The LES filtered governing equations for gaseous combustion can be written as [7] as following

• **Continuity**

$$\frac{\partial \bar{\rho}}{\partial t} + \frac{\partial \bar{\rho}\widetilde{u}_i}{\partial x_i} = 0 \tag{1.7}$$

• **Momentum**

$$\frac{\partial \bar{\rho}\widetilde{u}_i}{\partial t} + \frac{\partial \bar{\rho}\widetilde{u}_i\widetilde{u}_j}{\partial x_j} = -\frac{\partial P}{\partial x_i} + \frac{\partial \tau_{ij}}{\partial x_j} \tag{1.8}$$

• **Species continuity**

$$\frac{\partial \bar{\rho}\widetilde{Y}_\alpha}{\partial t} + \frac{\partial \bar{\rho}\widetilde{u}_i\widetilde{Y}_\alpha}{\partial x_i} = -\frac{\partial J_{\alpha,i}}{\partial x_i} + \bar{\rho}\widetilde{W}_\alpha \tag{1.9}$$

• **Enthalpy**

$$\frac{\partial \bar{\rho}\widetilde{h}}{\partial t} + \frac{\partial \bar{\rho}\widetilde{u}_i\widetilde{h}}{\partial x_i} = -\frac{\partial J_{h,i}}{\partial x_i} + \bar{\rho}\widetilde{W}_h \tag{1.10}$$

In the above equations, $\bar{\rho}$ is the mean density ; $\widetilde{u}$ is the velocity vector; P is the pressure; τ is the viscous stress tensor; $\alpha = 1, ..., N$ for number of species; $\widetilde{h}$ is the specific enthalpy; W_α is reaction rate for chemical species; W_h is the radiation transfer rate with the surrounding for standardised enthalpy; $J_{\alpha,i}$ and $J_{h,i}$ are the mass and heat diffusion respectively.

The solutions of the above equations are not straightforward as there are a number of unclosed terms and their solutions are not available in resolved scales. The filtered reaction rate source term is one of the most complex turbulent closure problem, which is highly non-linear and simple solution is not available, as

$$\widetilde{W_\alpha(T, Y)} \neq W_\alpha(\widetilde{T}, \widetilde{Y}) \tag{1.11}$$

The solution of filtered radiation transfer rate term is also difficult for the same reason. A number of modelling techniques have been reviewed in subsection 1.2.4 for the treatment of such complex turbulent closure problems.

1.2.2.2 Premixed turbulent combustion

Premixed turbulent combustion is growing as strict environmental legislation is forcing many commercial devices to reduce emissions. Premixed flame usually produces less unburned products as the higher degree of premixing provides effective control of combustion in the stoichiometry of flame. It is possible to use a lean mixture of fuel-air which can reduce a significant amount of unburned fuel, CO or particulates by virtue of chemistry. Combustion of premixed flames occurs in mostly thin, highly-wrinkled reaction surfaces, in which robust flame structures are observed by experimentalists. Flamelet modelling is successful for such a flame in many practical applications. The

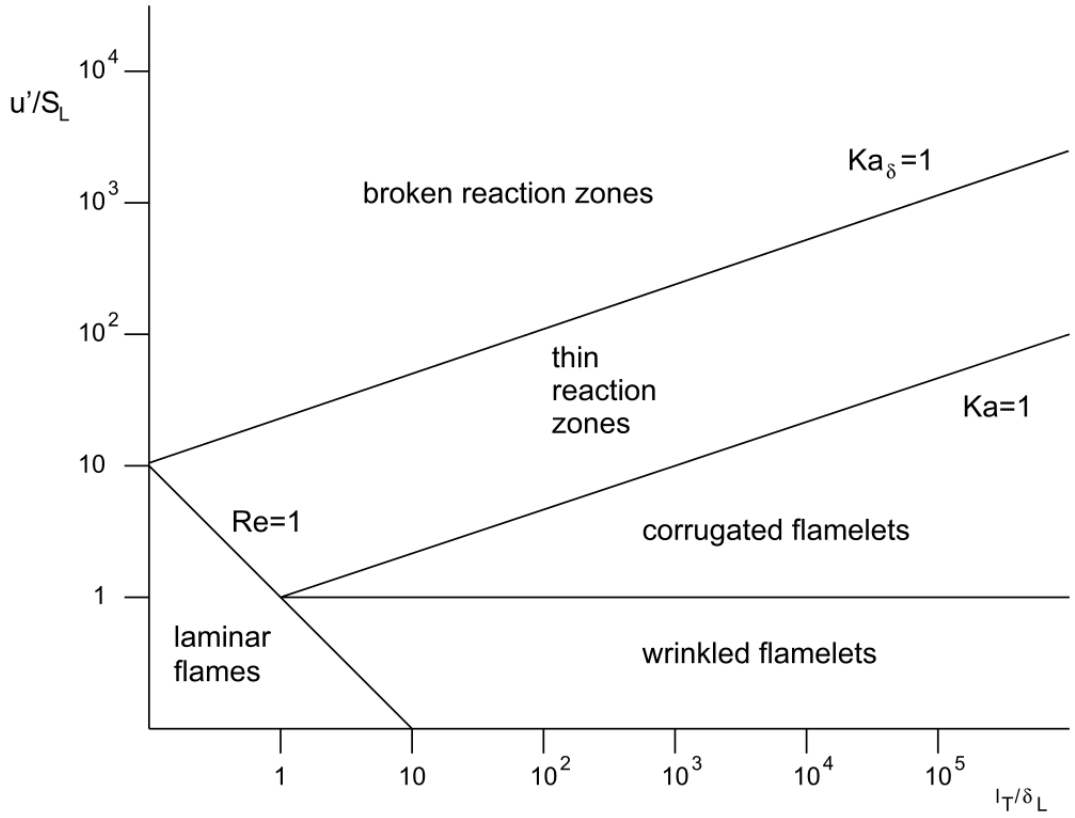

Figure 1.4: Regimes of premixed flame [16].

turbulent premixed regimes can be well defined by laminar burning velocity (S_L), velocity fluctuations (u'), laminar flame thickness (δ_L) and integral length scale (l_T). Figure 1.4 shows different regimes of premixed flames as described by Borghi's diagram and later modified by Peter [17]. The regimes are characterised by dimensionless Reynolds (Re) and Karlovitz numbers (Ka) and the five zones can be identified as follows: laminar flames, broken reaction zones, thin reaction zones, corrugated flamelets and wrinkled flamelets. Premixed flames are modelled successfully by both RANS and LES applying various reaction models: EBU, flame surface density approach, the G-equation, and scalar dissipation rate model [18].

1.2.2.3 Non-premixed turbulent combustion

There are many industrial applications where non-premixed combustion is necessary for safety reasons. Moreover, there is no need to design premixing devices for non-premixed combustion as the injection of fuel and oxidizer is done separately at the same time in the combustion chamber. There are many non-premixed combustion devices, for example, furnaces, diesel engines or gas turbines that are used in many commercial applications. Non-premixed flames are known as diffusion flames as the controlling mechanism implies the name diffusion. In the past, modellers consider infinitely fast chemistry for simulating such diffusion flames [19, 20, 21]. Diffusion flames cannot be characterised as premixed flames with well-defined time and length scales that is why modellers use the "flamelet approach" to describe basic features of the flames and then introduce the required scales. However, the interaction of diffusion flames with turbulence is sensitive due to front wrinkling and the effect of stretch. The local extinction and re-ignition make the flamelet approach less justified, and the finite rate chemistry has emerged for the modelling of non-premixed flames by the PDF approaches. The importance of finite rate chemistry will increase for the next generation clean and efficient combustion systems with high pressure, lower temperatures, extremely lean and/or dilute mixtures of different fuels with reactant mixture of H2, O2 and syngas and/or exhaust gas recirculation [7].

1.2.2.4 Partially premixed combustion

There are many combustion systems, including reciprocating devices or gas turbine engines, which do not meet the classical assumptions of premixed or non-premixed combustion theories. Most of the practical combustion processes, in fact, occur

in partially premixed mode. The composition of the combustible mixture can be non-uniform with all fuel-rich or all fuel-lean and the stoichiometric mixtures do not occur, will be referred to as stratified premixed flames. On the other hand, if the composition includes stoichiometric mixture with fuel-rich or fuel-lean then the possibility is that local burning structures may represent both premixed or non-premixed flames. The standard case for partially premixed flame is the lifted jet flames, where the prediction of lifted-off height is done by fully premixed or strictly non-premixed models [22]. The present modelling strategies have been developed based on the combination of both premixed and non-premixed situations in RANS [23] or LES [22] using flamelet approaches. However, it is not yet known how much of the flame structure is required or how to extend the applicability of different modelling approaches for partially premixed turbulent combustion.

1.2.3 Combustion of liquid spray

Liquid sprays are used in many industrial devices for a potential source of energy, which includes gas turbines, industrial furnaces, liquid-fuel rocket engines, diesel engines. The small size of droplets is usually desirable for efficient evaporation, combustion and mixing. The details of droplet dynamics and multiphase combustion modelling are available in many textbooks [24] and review papers [25, 26, 27, 28]. There are some interesting phenomena of droplets dynamics and their modelling in numerical simulation. In the following sub-subsections, some established theories are discussed to understand the features of such phenomena.

1.2.3.1 Preferential droplet concentration

The behaviour and distribution of droplets in turbulent flow can be explained by preferential concentration, which explains how the droplets are accumulated in a high concentration, where the strain rate is high and the vorticity is low. The Stokes number, St, which is expressed as the ratio of the droplet to carrier-phase inertia, plays an important role in preferential concentration. With very low St, droplets can follow all the motions of the carrier-phase and disperse as carrier-phase elements. The droplets that tend to accumulate with high St, can explain by taking the divergence of droplet velocity as

$$\nabla.v = -St(1-\beta)(||S||^2 - ||\Omega||^2) \tag{1.12}$$

where $||S||$ and $||\Omega||$ are the local strain rate and rotation-rate tensor respectively [25]. Droplets tend to accumulate($\nabla.v < 0$) when it is heavier $(0 < \beta < 1)$ than carrier-phase elements in regions where strain rate dominates over vorticity, whereas lighter droplets and bubbles $(0 < \beta < 3)$ tend to accumulate in the intense vorticity regions. The validity of Eqn. 1.12 on preferential concentration depends on the value of St. For a high value of St, the droplets are sluggish and have a small response on turbulence eddies' lifetime, whereas turbulent eddies have a significant coherent motion on droplets for intermediate St which justifies the importance of preferential concentration when $St \approx 1$.

1.2.3.2 Evaporation and micro-mixing

Evaporation and micro-mixing play a significant role in the chemical reaction rate in turbulent multiphase flow by influencing the distribution of gas species in the combustion

Figure 1.5: Schematic of droplet micro-mixing [30].

process. Bilger [29] explained the generalised method of mixture fraction to deal with both liquid and gas phases by the mixture fraction approach. The mixing between evaporated fuel vapour and other species can be expressed in terms of a mixture fraction. The gradient of a mixture fraction can influence the scalar dissipation rate, which in turn affects the reaction rate [30]. In premixed flames, the reaction rate is controlled by the flame propagation rate in quasi-laminar embedded flames based on the equivalent ratio, which is also in turn mixing. Figure 1.5 shows various scenarios of droplet evaporation in the presence of gas surrounding. In scenario 1, the isolated droplets are evaporating very early with very little vapour concentration in the surrounding. In scenario 2, droplets are clustering in high vapour concentration regions due to the modulation in droplet-droplet interface and evaporation rate decreases drastically within the droplet cluster. In scenario 3, droplet transportation between low and high vapour concentration occurs resulting in an additional dominant effect on evaporation. However, scalar gradients are highly enhanced in the micro-mixing process in the vicinity of the droplet surface, which is difficult to implement in the multiphase simulation [30].

1.2.3.3 Turbulence modulation

The droplet can change the characteristics of turbulence depending on the Stokes number [25]. The momentum coupling between dispersion phase and carrier phase can significantly change the turbulence of the flow. For a small droplet ($D^{fp} << \eta$) and a small carrier-phase gas containing a small volume fraction in a flow can have the same equivalent turbulence as in a single phase flow, whereas the larger droplet ($D^{fp} >> \eta$) or higher carrier-phase volume fraction can contribute to turbulent production, distortion and dissipation and the turbulent stresses can be either increased or decreased. Mechanisms of turbulence modulation are poorly understood because of the difficulty in accessing the carrier-phase data for a wide range of droplet sizes from small to largest eddies in carrier phases which causes problems in simulations. Therefore, turbulent modulation occurs due to the following mechanisms; damping due to larger droplets leading to enhanced dissipation, transfer of kinetic energy from the droplets to the continuous phase, and the formation of wakes and vortex shedding behind the particles [25].

1.2.3.4 Group combustion

Chiu *et al.* [31, 4] developed a series of group combustion models for studying the combustion behaviour of droplet clouds in a different cluster. The schematic of group combustion models is shown in Figure 1.6 based on the total droplet numbers, N, and a non-dimensional separation distance, S. Spherical droplet clouds are considered in the experimental studies and the spray combustion of droplets is classified according to group combustion number, G, which is defined as the ratio of heat exchange between two phases

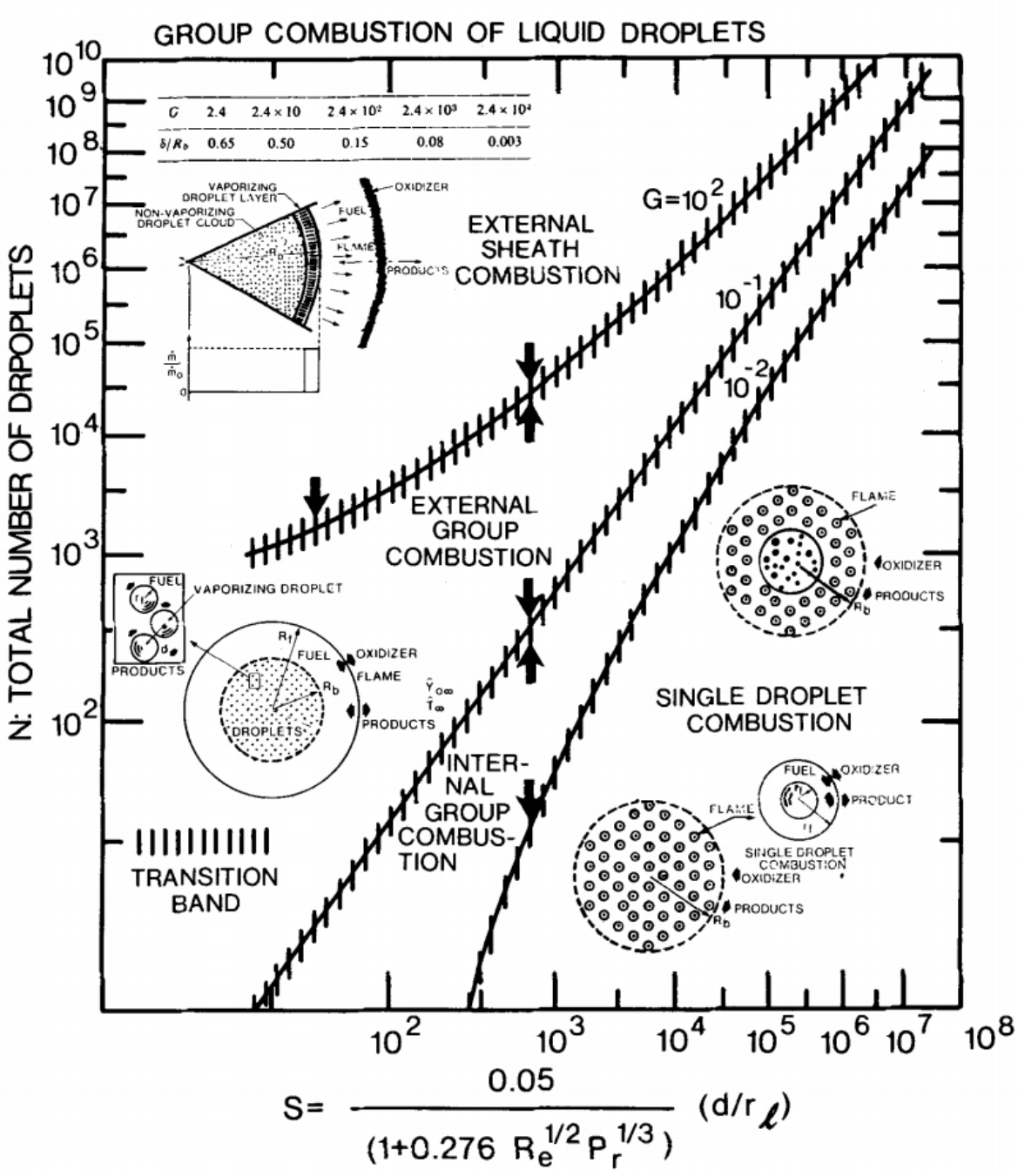

Figure 1.6: Schematic of group combustion modes for droplet clouds [31].

to the rate of heat of vaporisation as following [31]

$$G = 3\left(1 + 0.276Re^{1/2}Sc^{1/3}\right) LeN^{2/3}\left(\frac{r_l}{d}\right) \tag{1.13}$$

where Le is the Lewis number and d is the inter-droplet separation, r_l is the reference droplet size. The non-dimensional separation is also defined as

$$S = 0.05\frac{d/r_l}{1 + 0.276Re^{1/2}Pr^{1/3}} \tag{1.14}$$

Figure 1.6 shows four group combustion zones for a different range of group numbers. For a high value of G ($G > 10^2$) external sheath burning occurs, where there is an inner non-vaporising droplet surrounded by a layer of vaporising droplets. The flame of the external sheath burning is at a distance away from the spray boundary, for such high G sprays have higher burning rates and low core temperature. The external group combustion zone, which is in the marginally high-G sprays ($G > 1$), consist of an inner vaporising cloud with a diffusion flame from the boundary of the droplets. The internal combustion group stands in the range of $10^{-2} < G < 1$, where the flame locates within the boundary but the individual droplet burns in the outer regions of spray. For low-G values ($G < 10^{-2}$), the mode becomes single combustion in the cloud associated with the envelope flame surrounding the droplet.

Although the group combustion model is instrumental in understanding various possible scenarios of droplet combustion, it is very complex and difficult to apply in real combustion modelling applications [32]. Moreover, droplet size, cluster, and distribution is not uniform in the real droplet clouds in the spray. Despite such limitations, recent studies [33, 34, 35] have applied group combustion both experimentally and numerically. Moreover, the group combustion model can be used for the post-processing analysis of

spray flames.

1.2.4 Turbulent combustion chemistry modelling

1.2.4.1 Chemical reaction

Chemical reaction plays an important role in the turbulent combustion process, where a number of elementary reactions are involved in different species. A typical chemical reaction for reactants and products is,

$$A + B \rightarrow C + D \tag{1.15}$$

where A and B represent reactants and C and D are products of the bimolecular elemental reaction. In practical combustion, there are thousands of such reactions and products taking part in the combustion process. The rate of reaction is directly proportional to the concentration of reactants as following,

$$\frac{d[A]}{dt} = -k(T)[A][B] \tag{1.16}$$

where, $k(T)$ is bimolecular reaction rate, which is a function of temperature. For small temperature range, the Arrhenius form of equation is used for calculation of the reaction rate as following,

$$k(T) = Aexp(-E_a/RT) \tag{1.17}$$

where E_a is the activation energy, R is gas constant, A is pre-exponential factor. The values of A and E_a are dependant on the reaction. For large temperature change, the pre-exponential factor is not constant and an extended form of the equation is used for

calculating reaction rate constant as

$$k(T) = AT^{b}exp(-E_a/RT) \tag{1.18}$$

The above reaction rate, $k(T)$, is a function of temperature and species, which is highly non-linear and adds extra complexity for solving governing equations of turbulent combustion and their associated modelled equations. Turbulent combustion modelling approaches are greatly influenced by the way the filtered reaction rate is calculated. In the following subsection, the details of combustion models are reviewed highlighting the different numerical techniques for calculation of accurate reaction rate.

1.2.4.2 Algebraic approach

1.2.4.2.1 Eddy breakup model The eddy breakup model (EBU) was proposed by Spalding [36] and later modified by Magnussen and Hjertager[37]. The EBU was developed based on the physical assumption that the reaction rate is faster than the rate of mixing of species. The reaction rate in turbulent flow is assumed to be the same as the rate of scalar dissipation rate although the reaction rate for the laminar flow depends on the mixing of species.The reaction rate for the EBU model can be represented as

$$\widetilde{W_p} = C_{EBU}\frac{\epsilon}{k}\sqrt{\widetilde{Y_p''}} \tag{1.19}$$

where p is the product species, C_{EBU} is EBU constant, $\widetilde{Y_p^{"}}$ is the variance of the product mass fraction. Assuming there is no intermediate combustion state, the Eqn. 1.19 is further modified by

$$\widetilde{W_p} = C_{EBU}\frac{\epsilon}{k}\widetilde{Y}_p(1-\widetilde{Y}_p) \tag{1.20}$$

Although the EBU model has already been applied widely, it is not successful for the species like NO, which is not represented by fast chemistry.

1.2.4.2.2 Eddy dissipation model The EBU model is the earliest model successfully applied for both premixed and non-premixed combustion cases. However, in the EBU model, the reaction rate in Eqn. 1.19 is only related to turbulent dissipation of product gas. The eddy dissipation model (EDM) [38] was developed extending the concept of EBU for all fuels, oxidizer, and products as following,

$$\widetilde{W_p} = A\frac{\epsilon}{K} min\left(\widetilde{Y_F}, \frac{\widetilde{Y_{OX}}}{S}, B\frac{\widetilde{Y_p}}{1+S}\right) \tag{1.21}$$

where F and OX denotes fuel and oxidizer respectively, S is the oxygen-fuel stoichiometric mass fraction ratio, and A and B are model parameters.

Both EBU and EBM are still used in many CFD packages, but they can be only applied to the infinitely fast chemistry unless explicitly chemical time scales are taken into account [38].

1.2.4.3 Low dimensional manifold approach

1.2.4.3.1 The Burke-Schumann analysis The earliest theories of laminar jet diffusion flame are the Burke Schumann's approximate solutions [39] for one-step irreversible fast chemistry. According to Burke-Schumann's solutions, fuel and oxidizer react in stoichiometric proportions at the flame. The flame can be represented by an infinitely thin sheet which is also known as a flame-sheet. Burke-Schumann describes the flow field in terms of single fuel species, for which the mass fraction takes a value of unity in the fuel stream and zero in the pure oxidizer. Both fuel and oxidizer are zero at

the flame. This solution provides a linear relation between species and mixture fraction. The profile can be improved by assuming the chemical equilibrium is fast and reversible. It assumes the chemical equilibrium timescales of major species are faster than the flow time scale and the application of equilibrium solutions to LES is in good agreement with experimental data [40]

1.2.4.3.2 The flamelet modelling approach The laminar flamelet modelling approach appeared in the early 1980s with the underlying concept that the flame reaction zone is as thin as laminar flames subjected to the same scalar dissipation. Peters [41] showed that species conservation equations could be transformed into a set of stationary laminar flamelet equations by assuming transient terms and the gradient of the mixture fraction to be small. However, there are questions about the validity of this approach when there is a variation of scalar dissipation through flamelets and the influence of neglected advection terms in the transport equation. It is clear that the laminar flamelet cannot remain valid in the presence of local extinction and re-ignition when unsteady and flame edge effects [42] must become important. It is also a concern that the laminar flamelet approach will not be appropriate when the turbulence length and time scales are relatively smaller than the laminar flame. The laminar flamelet equation has been modified to include transient effects [20, 21], which allows [17] strong fluctuations of scalar dissipation and accommodates advection terms in Lagrangian fashion. Large Eddy simulation incorporating such a viewpoint has been successful [43]. The broadening of the flamelet and its extinction are the two factors also affecting the flamelet model which are governed by the local Damkohler number and the level of mixture fraction fluctuations [44]. However, most experiments are conducted in room temperature reactants and

low-density gas velocities, which favour flamelet formation.

1.2.4.3.3 The conditional moment closure The conditional moment closure (CMC) is a modelling approach that has been motivated by the need to implement an accurate closure of the non-linear turbulent reactive source term. The CMC transport equations for turbulent reacting flows were derived by Klimenko [45] and Bilger [46] and jointly reviewed by Klimenko and Bilger [47]. The CMC modelling was inspired by laser-diagnostic measurement of jet diffusion flames and by experiments of the reacting mixing layer, where the flamelet model would not be applicable for the slow chemical reactions of nitric oxide and ozone [48]. The basic concept of CMC is to exploit a strong correlation between reacting scalar species and the mixture fraction space [18]. The conditioning of reacting species based on the mixture fraction leads to small fluctuations around the conditioning mean, and simple first order closure is found to be sufficient. The first order CMC is applied for some simple turbulent diffusion flames [49, 50, 51] and the solution of the temporal and spatial evolution of the conditional moments gives a good prediction of finite-rate chemistry effects. Although the fluctuation around the conditional mean is very important, it does not mean that the CMC will be invalid if conditioned and conditioning quantities are not well correlated. As the fluctuations of conditional averages are small, the conditional average reaction rates are well approximated using conditional averages of temperature and mass fractions. Many non-premixed flames, including flows with recirculation and auto-ignition of sprays, have been successfully modelled using first-order CMC [5]. However, first order CMC is not sufficiently accurate for the cases of flames with local extinction and re-ignition [52] and the second order CMC has been sought [47] to incorporate the variances and co-variances in the conditional reaction rates.

Kronenburg *et al.* [53] implemented second order CMC by a reduced mechanism for the reaction rate of hydrogen for improving the prediction of temperature sensitive species, NO.

An alternative to second order conditioning is to apply double conditioning for the closure of average conditioned reaction rates. Kronenburg [54] implemented such a double conditioning technique for both mixture fraction and sensible enthalpy. The average reaction rate is found in excellent agreement with DNS in homogeneous turbulence with multi-step chemistry with strong local extinction and re-ignition. Double conditioning has promising capability provided that other unclosed terms are modelled accurately, for example, closure of dissipation terms. It is also important to derive correct forms of CMC equations to satisfy the boundary conditions correctly. The fully conservative forms of equations are sought as the problem of finite difference forms arises due to auto-ignition of a jet in hot co-flow regions where the probability density of mixture fraction may be zero in part of its range [47].

In the CMC method, the conditional velocity, and the conditional scalar dissipation must be modelled in such a way to be consistent with CFD flow and mixing fields to get the full advantage of CMC. In earlier work, a linear model [47] has been used for conditional velocity, but this was inconsistent with the gradient model commonly used for closure of the turbulent flux of the variances of mixture fraction [5]. A gradient model for the conditional velocity is fully consistent with the CFD modelling [5], which leads to significant modelling capability of the conditional scalar dissipation by integrating the PDF transport equation using a presumed form of PDF of mixture fraction.

The modelling of partially premixed flames is ideally suited for the approach of

double conditioning, where both mixture fraction and sensible enthalpy are conditioned. The reacting flames with local extinction and later re-ignition due to turbulent and/or molecular diffusion leading to partially premixed regions is a good candidate for the double conditioning approach in many studies, for example, the DNS study of Cha *et al.* [55] and the similar studies of Kronenburg *et al.* [54, 56]. The CMC predictions of later studies agree very well with DNS data.

1.2.4.4 Stochastic approaches

1.2.4.4.1 The PDF approach The PDF methods have emerged as one of the promising approaches for CFD modelling of turbulent reacting flows. Dopazo and O'Brien [57, 58] were the first to introduce the PDF approach in modelling mixing and chemical reaction in turbulent reacting flows. The PDF transport equation can be solved with finite volume and finite difference methods but cost increases exponentially with the number of dimensions. The PDF methods emerged as a powerful tool when Pope [59] established the relationship between particle models and PDF methods [59]. In PDF methods, Monte Carlo Lagrangian particle methods are used in many applications, while this method is still computationally expensive, cost increases linearly with the dimensionality of the problem. In the Lagrangian approach, particles are not bound to grid nodes. Particles are notional, have a position, move through the domain and are characterised by values of the reacting scalars. In some publications, Lagrangian particles are termed as Pope particles [60]. Using N_p number of particles, error is proportional to the reciprocal of $\sqrt{N_p}$ per cell. Conventionally, there are over a few particles in each cell in the numerical model. For grids with thousands of cells, this can result in the order of

thousands to millions of particles in LES context [61]. Performing reactions over so many particles is computationally expensive and costs can be prohibitive. Tabulation and sparse methods have been developed to reduce the cost [2].

The PDF method was introduced in the 1970s to address the degree of scattering observed in hydrocarbon flames, especially the occurrence of composition outside of the steady laminar flamelet regime [58, 62]. The PDF method provides an elegant and effective resolution to the closure problems that arise from averaging or filtering chemical source terms and other non-linear terms in the equations that govern chemically reacting turbulent flows [21]. Although in the Eulerian [63] and Lagrangian [59] Monte Carlo particle methods developed and applied to piloted jet flames in reduced mechanisms, the scatter plot results were qualitatively in agreement with measurement, further improvement is required for both calculations and measurements. Some noticeable success was found in laser diagnostic measurement of Sandia Flame D, E and F [64] and the PDF calculation of Xu and Pope [65]. Although there is success in the PDF modelling approach, there are still questions about the physical realism of the mixing model. The primary mixing models are IEM [58], modified Curl [66] and EMST [67] which are found to yield substantially different distributions and also predict extinctions at various Damkohler numbers [68]. There are three major problems in PDF mixing models. First, there is no coupling between mixing and reaction. Second, there is no locality in composition space in MC and IEM models. The EMST model is developed to address this second issue. Third, none of the models includes the physical realisation of the fluctuations of scalar dissipation. PDF methods are applied to complex flames like bluff body stabilised jet flames [69] and swirling bluff-body flames [70]. The PDF

methods have now been matured enough and are included in the CFD code for both research and industrial applications.

1.2.4.4.2 Multiple mapping conditioning MMC is a modelling framework introduced by Klimenko and Pope [23], which unifies the concept of PDF [71, 59] and the CMC method [47] including a generalisation of the mapping closure [72, 73] method. The key features of MMC are to use reference variables, which are related to the physical quantities in turbulent combustion. The reference variables can be mixture fraction, sensible enthalpy, velocity and scalar dissipation or other quantities as desired. MMC allows all the generality of PDF methods with the addition of some advantages of CMC. Both deterministic and stochastic MMC exist. Deterministic MMC is the natural extension of CMC, while stochastic MMC is a complete joint PDF method with MMC playing the role of mixing model to enforce locality within a defined manifold. Some specific MMC models [74, 75, 76, 77, 78, 79, 80, 81] have been developed since the MMC framework was proposed [23].

In deterministic MMC, the reference variables are used as a conditioning variable, and fluctuation around the quantities is conditionally averaged on that reference space. These fluctuations are considered to be small and known as minor fluctuations. In the deterministic MMC, these minor fluctuations are not considered for calculating reaction rates. The major species are allowed to fluctuate in any physically realisable way, whereas the minor species are only allowed to fluctuate jointly with the major species. The reference variables and physical scalars are modelled according to the mapping closure concept, which was first introduced by Chen $et\ al.$ [72]. The statistical information of scalars and species is then obtained from the modelled mapping functions from the

prescribed reference space of joint PDF.

The stochastic MMC is based on the use of Lagrangian particles following the PDF method as described by Pope [59], which is equivalent to the deterministic MMC. In stochastic MMC, the reference values are assigned to stochastic particles [2]. Moreover, MMC is a complete joint PDF method with MMC playing the role of a mixing model, which enforces localness with a defined manifold [7]. The sparse distribution of particles is used to model the Lagrangian filtered Density function (FDF), which is computationally less expensive compared to normal PDF that resolves all the distribution of turbulent scales. The treatment of large scales is resolved by LES, while the subgrid distributions are modelled by FDF technique using sparse particles.

The deterministic and stochastic MMC are the basic framework of MMC that assumes the major species manifold is known and the minor fluctuations are negligibly small. In the basic MMC, the minor fluctuations are neglected and therefore composition is modelled as conditional mean. In the stochastic MMC, although the minor fluctuations are permitted they are dissipated towards conditional mean as a minor dissipation operator. To expand the purpose of reference variable beyond conditioning or localisation, MMC has been generalised to make it more amenable to practical implementation, which is known as generalised MMC. The generalised MMC accepts minor fluctuations in the model that can assist in modelling, but which are not used for the conditioning purposes. Practically, this is how the mixing is localised on conditioning variable space only, while non-conditioning variables complement the conditioning variables and improve the emulation of the physical quantities [7]. The generalised MMC was first proposed by Klimenko [82] to expand the purpose of reference variables beyond the conditioning

and localisation. The generalised MMC is more open to practical implementation and a series of studies [75, 76, 83] were done for the DNS/LES regime and replaced Markov reference variables with Lagrangian variables. The generalised MMC with MMC-Curl mixing model has been applied for this study.

1.3 Present contributions

Combustion of liquid fuel is a relatively immature field in the combustion research community. The modelling challenges of liquid sprays are implementing the processes: evaporation, heat and mass transfer, volatile formation and radiation for heterogeneous or homogeneous combustion. The gas phase simulation must be coupled with the dispersed phase to account for gas production due to the above processes. On the other hand, the dispersed phase needs to be coupled with gas phase properties to calculate heat and mass transfer between gas and dispersed phase particles. Following this, coupling between LES and the dispersed phase is also necessary for updating the source term in LES momentum equation for mass and drag. Therefore, two-way coupling among multiple phases with LES is an important aspect of realistic modelling. In this study, a dispersed phase Lagrangian fuel particle model is developed following the approach described by Spalding [84]. Some contemporary studies [85, 86] applied the Spalding method for dispersed phase modelling by applying the mass fraction approach, which is inconsistent with combustion cases where the mass fraction is totally consumed at stoichiometric regions. The mixture fraction approach has no such issues as atomic elements are always conserved in combustion and the method is consistent for entire regions of mixture fraction values. In this study, the mixture fraction approach is applied

for both gas and liquid phase formulations following Bilger's formulation [29]. Moreover, a separate Lagrangian particle model for the dispersed phase is an advantage for easy tracking of individual particles and their statistical properties.

The research community needs a platform to advance the existing combustion modelling of liquid sprays. OpenFOAM is a free open source software, and it is easy to customise the specific modelling needs. In this study, a new source code is developed for liquid phase modelling. This is a new addition to the existing MMC source code, which is devoted to gas phase simulation. From the perspective of gas phase simulation, MMC is promising for implementing the advanced stochastic Lagrangian particle approach for gas phase mixing, chemical reaction and closure of the chemical reaction source term. For multiphase modelling, a dispersed phase particle model is needed. This study has successfully implemented such a model in the Lagrangian fuel particle approach and coupled with LES and MMC. The developed new source code is tested and compared to the experimental data of non-reacting kerosene, evaporating acetone, and reacting acetone cases [1] for accuracy.

1.4 Outline

The outline of this thesis is as follows: The state of the art of multiphase combustion modelling of liquid sprays is reviewed in Chapter 1. Chapter 2 reviews the behaviour and modelling approaches of the liquid phase in the context of multiphase combustion. Following the approach described by Spalding [84], the heat and mass transfer to and from the liquid phase is derived with the introduction of the Lagrangian fuel particle. The formulations are derived starting from a simple heat and mass transfer principle to

detail the derivation of formulations and closure equations for heat and mass transfer for homogeneous combustion and radiation. The governing equations are derived in Chapter 3 for the proposed multiphase combustion model by applying the newly developed Lagrangian fuel particle model with other subgrid models. The filtered transport equations are derived with the introduction of a phase-weighted indicator to represent the multiphase flow field in LES. The filtered density function (FDF) formulations are also derived in the gas phase simulation and for the chemical reactions. Chapter 3 includes all formulations of LES and FDF methods including source terms and their coupling. The details of model, geometry and boundary conditions are described in Chapter 4. The simulation results of non-reacting kerosene cases are presented in Chapter 5. The results of evaporating and reacting acetone cases are presented in Chapter 6 and 7, respectively. The validation cases include the comparison of simulation results with experimental data, analysis, and conclusions. Chapter 8 is devoted for conclusions and recommendations for future work.

Chapter 2

The liquid phase model

Liquid phase modelling is far more complex compared to single carrier-phase flames in CFD modelling. The stochastic nature of carrier-phase turbulence and the various distributions of dispersed particles are highly complex to implement in a modelling framework for the simulation. On the other hand, the profile of the carrier phase flame structure can be influenced by dispersed phase particles due to heat and mass transfer to and from the carrier phase. There are many modelling techniques of droplet dynamics and multiphase combustion depending on the purposes, flow conditions and liquid droplet model. A realistic numerical spray model must involve the characteristic consideration of injection, dispersion of individual particles, the turbulence of multiphase flow and the exchange of heat and mass between phases. In this study, a Lagrangian fuel particle model is used for easy tracking of individual particles in a parcel for obtaining detailed information about a particle and then coupling the liquid phase with the carrier phase. In this chapter, different modelling approaches of the liquid phase are reviewed in section 2.1 and the formulation of the Lagrangian fuel particle model is presented in section 2.2.

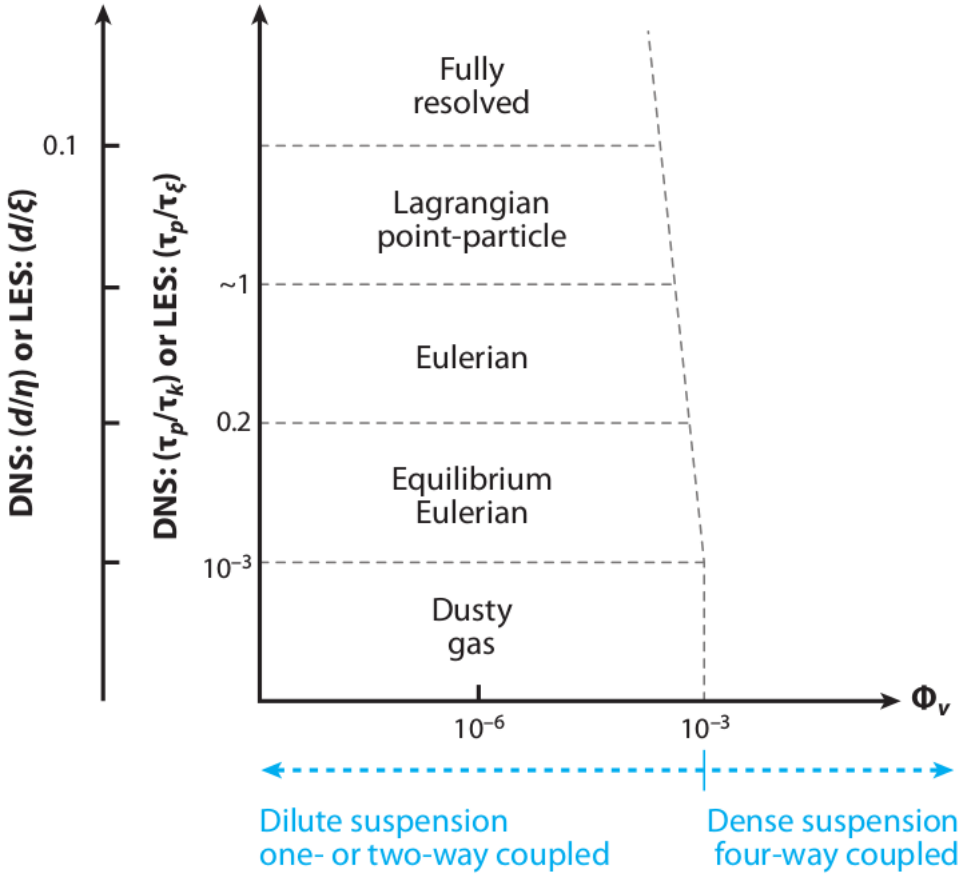

Figure 2.1: Schematic of different approaches of dispersed multiphase flows in terms of particle sizes and volume occupied by liquid phase (Φ_v) [25].

2.1 Liquid phase modelling approaches

Figure 2.1 shows different computational approaches that can be used in modelling of dispersed multiphase flows [25]. The applicability of different approaches is explored with respect to relative particle size and time scale with a fraction of the volume occupied by the dispersed phase (Φ_v). This is explained with the introduction of Stokes number, St, defined by $St = \tau_p/\tau_k$, where τ_p and τ_k are particle and Kolmogorov time scales respectively. The length scales are d, η and ξ which represent particle length, Kolmogorov length and the smallest resolved LES length respectively. For the DNS case, Kolmogorov length and Kolmogorov time scale are used, whereas for the LES context, the Kolmogorov

length and time scales are replaced by the smallest resolved LES length, ξ, and the time scale of the smallest resolved eddy, τ_ξ respectively. The details of these modelling approaches are discussed in the following subsections.

2.1.1 Dusty gas approach

The dusty gas approach is applicable for perfectly small particles which follow the local carrier phase in a particle laden-compressible flow [25]. This approach was matured by Carrier [87] and Frank [88]. This is considered as a single fluid approach whose density depends on the mass fraction of particles. This one-fluid approach is widely used for both compressible and incompressible flows. The advantage of this approach is simplicity and the solution of only particles concentration is needed in addition to mass, momentum and energy equations. However, this approach works only for the small time constant (see Figure 2.1).

2.1.2 Equilibrium Eulerian approach

In the equilibrium Eulerian approach, particle velocity is assumed to be different from the carrier phase [25] and their velocity is dictated by the surrounding fluid [89]. The particle velocity, v, is calculated based on the carrier fluid velocity, u, as following

$$v = u + \begin{cases} -St(1-\beta)\frac{Du}{Dt} & \text{for } |w| << St \\ w - St(1-\beta)\frac{Du}{Dt} & \text{for } |w| \sim O(St) \\ w - St\left[(1-\beta)\frac{Du}{Dt} + w.\nabla u\right] & \text{for } |w| \sim O(1)\} \end{cases} \tag{2.1}$$

where $\tau_p = (D^{fp})^2\rho[18\nu\phi(Re)]$, $\beta = 3/(2\rho + 1)$, particle to fluid density, $\rho = \rho_p/\rho_f$ and D^{fp} is particle diameter, ν is the kinematic viscosity, w is the particle settling parameter. The velocities u, v and w are normalised by Kolmogorov velocity, v_k.

The equilibrium Eulerian approach captures particle motion more accurately and validates important phenomena of preferential particle concentration and turbophoresis [90]. The accuracy of equilibrium has been tested by Ferry and Balachandar [91] for a variety of turbulent flows and fairly good accuracy is found with $St \lessapprox 0.2$.

2.1.3 Eulerian approach

This is a two-fluid approach, where the carrier and the dispersed phases are interacting with each other in fluid media and exchange momentum and energy. The energy exchanges are considered as source and sink terms [25]. The dispersed phase properties are given Eulerian field representation [92, 93, 94] and the additional momentum and energy equations for the dispersed phase are solved, unlike the dust gas and the equilibrium approach, where only carrier-phase equations are taken into care. The advantage of this method is to allow a higher Stokes number i.e. larger particles are applicable for the Eulerian approach. The Eulerian approach is computationally expensive as more equations are solved for polydisperse systems with a wide range of particle sizes. Then again, polydispersity can be handled in the Eulerian approach by using the PDF method for a wide variety of particle sizes [95].

2.1.4 Lagrangian point-particle approach

The Lagrangian point-particle approach has been applied to many dispersed multiphase flow studies [96, 97, 98]. In this approach, the equation of motion is solved to track the position, mass, momentum and energy of particles and then applied to the interface coupling. In the Eulerian approach, a unique flow field representation for particle velocity and the temperature is needed, which indirectly restricts the maximum St number that can be applied [89]. For violation of uniqueness, either the probabilistic method or the ensemble average of particle properties in Eulerian fields is adapted. For the Lagrangian approach, there is no restriction on maximum St as there is no requirement for uniqueness. This method is used in this study for taking advantage of separate particle models for the carrier phase and the dispersed phase and coupling between them with the LES field. The application of different Lagrangian particle approaches is described in the following subsubsections.

2.1.4.1 DNS-Lagrangian approach

Most of the DNS studies resolve all scales of flow field down to particle size. The size of the Lagrangian particles must be smaller than the Kolmogorov scale and thus the particles are assumed as point particles. Early studies of DNS with Lagrangian particles were one way carrier-phase coupling [96, 99, 100] followed by two-way coupling in later works [101, 102, 100]. The investigation of dispersion and preferential concentration of particles was done by DNS study for different Stokes numbers [103]. The mixing of evaporating fuel particles was studied by Le *et al.* [104]. A number of DNS studies are available in the literature for various conditions implementing the Lagrangian particle approach

[105, 106, 107, 108].

2.1.4.2 LES-Lagrangian approach

The Lagrangian particle scheme has been used in a number of LES simulations [86, 109, 110, 111] in the recent past for implementing dispersion and evaporation of particles. Most of the studies updated momentum source terms for drag and mass due to dispersion and evaporation respectively. Jones *et al.* [112, 85, 113, 111] included stochastic dispersion terms in the simulation and found that it can influence the flow field. Pozorski and Apte [114] studied the randomizing effect of the residual velocity field reconstructed by filtered particle tracking method. They found that the randomizing effect of small scales is destroyed for droplets larger than the maximum preferential concentration ($St = 1$), since the model is based on one-point statistics only. Moreover, the stochastic dispersion model may not reproduce the instantaneous field correctly. For this study, the stochastic dispersion of the LES subgrid effect is not considered to avoid numerical instability.

2.1.4.3 RANS-Lagrangian approach

In the RANS-Lagrangian approach, a number of models [115, 116, 117, 118] have been proposed which include stochastic dispersion and the evaporation source term. Since all turbulent fluctuation remains unresolved in the RANS context, the modelling of the dispersion phase is critical in the RANS-Lagrangian approach. The stochastic dispersion can be modelled by Fokker-Plank equations in Eulerian formulations of Langevin equation. However, using the Fokker-Plank equation, PDF can be solved up to higher moments [119, 120]

2.1.5 Fully resolved approach

The fully resolved approach is a costly method as all scales are considered down to particle size. In the above methods, the size of particles is restricted to being smaller than either the Kolmogorov scales or the smallest resolved eddies. For a most precise approach, the ultimate options are to implement turbulence, and all flow scales up to fully resolved DNS according to particle size. For the Lagrangian context, it is based on the point-particle assumption, whereas for the Eulerian approach, the particle size may be even smaller than the flow scales such as the size of the particles used in the analysis of force or heat transfer laws [121]. Fully resolved approaches are applied for a single particle [121, 122, 123]. Similar studies for fully resolved cases are also available, for example, the studies of Stauch and Maas [124] for auto ignition in a laminar convection condition, Zoby *et al.* [125, 33] for tracking gas-liquid interface, droplet arrays and droplet statistics, Berton and Elton [123] for isotropic turbulence. Imaoka and Sirignano [126, 30] studied droplet arrays in quasi-steady combustion. Some studies applied a fully resolved approach to a collection of one thousand particles [127, 128, 129]. However, most of the applications are limited in far more particles and the fully resolved approach for a large number of particles is not yet possible.

2.1.6 Methodology for this study

According to the above discussion, the Lagrangian point-particle approach is suited for both large ($St > 1$) and small particles ($St < 1$). However, the Eulerian approach can be a better alternative for smaller particles in the context of computational efficiency. For $St < 0.2$, both dusty and equilibrium approaches can be a good option. In the

range of $0.2 \lessapprox St \lessapprox 0(1)$, both Lagrangian point-particle and Eulerian approaches are good candidates [121]. For the LES carrier phase simulation, a Lagrangian point-particle method is a viable approach provided that particle time scale is larger than the timescale of the smallest resolved eddy. Moreover, the Lagrangian point-particle approach is easy to track individual particle's properties and particle clouds compared to the Eulerian approach. Again, the Lagrangian point-particle approach is easy to solve the liquid phase governing equations and close the source terms in the LES and Gas phase MMC simulation, and is the reason why the Lagrangian point-particle approach has been chosen for this study.

2.2 Lagrangian fuel particle model

2.2.1 Particle dispersion

The dispersion of fuel particles is tracked in Lagrangian fashion in parcels which represent many identical particles. Here, a method for modelling of polydispersed, spherical fuel particles is adapted that is based on the approach of Dukowicz [130], which is commonly used in both spray dispersion [85, 117] and solid particle modelling [131]. The governing equations of location and velocity of the fuel parcels are

$$\frac{dx_i^{fp}}{dt} = u_{D,i}^{fp} \tag{2.2}$$

$$du_{D,i}^{fp} = (a_{D,i}^{fp} + g_i)dt + b_{D,i}^{fp} dw_i \tag{2.3}$$

where g_i is the acceleration due to gravity and $b_{D,i}^{fp} dw_i$ is a stochastic term which simulates the subfilter differential velocity. $b_{D,i}^{fp} dw_i$ has a very small effect in LES and may be

neglected as a first approximation [86]. $a_{D,i}^{fp}$ is modelled by relaxation to the filtered gas phase for spherical particles [132]. In return, the particles impart a momentum change on the gas-phase, appearing as a source term in the Navier-Stokes equation. The Eqn. 2.3 may have some other terms such as effect of pressure gradient, the Basset force, and the Saffman and Magnus lift forces but these are neglected here for simplicity as they have negligible effect on particle dispersion. The velocity of the inertial fuel particles is a response to drag forces imparted by the gas-phase and gravity. The deterministic acceleration is modelled as a relaxation to the gas-phase velocity as

$$a_{D,i}^{fp} = \frac{\widetilde{u}_{G,i}^{fp} - u_{D,i}^{fp}}{\tau^{fp}} \tag{2.4}$$

where the timescale

$$\frac{1}{\tau^{fp}} = \frac{3}{4}\frac{\rho_G^{fp}}{\rho_D^{fp}}\frac{C_d^{fp}}{D^{fp}}\left|\widetilde{u}_G^{fp} - u_D^{fp}\right| \tag{2.5}$$

is a function of drag coefficient for spherical particles

$$\begin{aligned} C_d^{fp} &= \frac{24}{Re^{fp}}\left(1 + \frac{(Re^{fp})^2/3}{6}\right), \quad \text{for} \quad 0 < Re^{fp} < 1000 \\ &= 0.424, \quad \text{for} \quad Re^{fp} >= 1000 \end{aligned} \tag{2.6}$$

In additional to the above dispersion modelling, the Lagrangian fuel particle model also requires expressions for the rate of change of fuel particle mass and temperature with time. The expressions for heat and mass transfer depend on the evaporation process. For this study, such expressions are derived in the next section.

2.2.2 Heat and mass transfer with homogeneous combustion and radiation

Models for the turbulent combustion of gaseous fuels are widely reviewed in the literature [5], and among those, the mixture fraction-based models for non-premixed combustion are highly regarded for their accuracy and computational efficiency [47]. However, practical combustion processes involve liquid fuels inflow continuing of atomisation and dispersion, vaporisation, and heterogeneous and homogeneous combustion. Each process is affected by turbulence. Just as the closure of turbulent gas-phase reaction rates is complicated by their non-linearity, so too is the closure of the turbulent heat and mass transfer rates between the continuous and dispersed phases. In the context of a single, evaporating liquid droplet, Spalding [84] derived heat and mass transfer relations for both with and without gas-phase reactions. He showed that, for cases where combustion reactions are occurring, the transfer relations are greatly simplified when based on conserved scalars such as the mixture fraction and/or standardised enthalpy. Some contemporary spray combustion publications [113] use transfer relations which are, strictly speaking, only valid in the absence of gas-phase combustion. The implications of this inconsistency are untested. The expressions for heat and mass transfer are derived based on the mixture fraction approach. The starting point is the derivation of heat and mass transfer between a single isolated fuel particle and quiescent, gaseous surroundings. For the first time, the theory is extended to evaporating liquid droplets. The mass transfer by pyrolysis and char conversion processes can be included but it is not studied in this study.

In this section, the equations for conductive heat flux to and evaporative mass flux

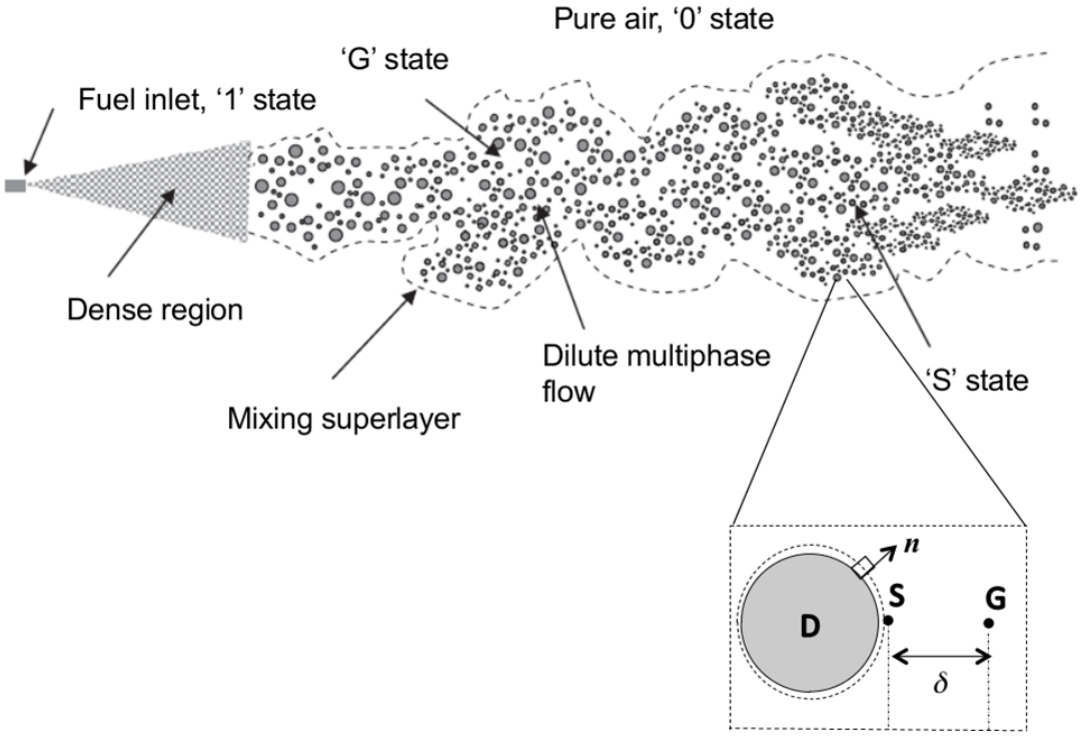

Figure 2.2: Schematic of a turbulent dilute multiphase jet (top) and with zoom view of a single fuel particle showing D, S and G states (bottom).

from a fuel particle is derived. The formulations for both heat and mass transfer perspectives of an evaporating fuel particle are considered for deriving and closing the set of equations. Simultaneous heat and mass balances are applied to calculate the temperature of the fuel particles needed to close the equations. The boundary conditions are applied for latent heat accompanying the phase change and the internal heating of fuel particles. The following system of equations is used for these expressions: i) a PDE for energy transfer expression for mass flux; ii) a PDE for mass transfer equation leading to a second expression for the mass flux iii) an ODE for the variation of fuel particle temperature with time; iv) an algebraic model for the surface conditions. Figure 2.2 shows a schematic of dilute multiphase flow and two stream mixing. The close-up view shows a single fuel particle with D, S and G states and characteristic diffusion length δ. An isolated fuel particle is considered for deriving equations for simultaneous heat and mass

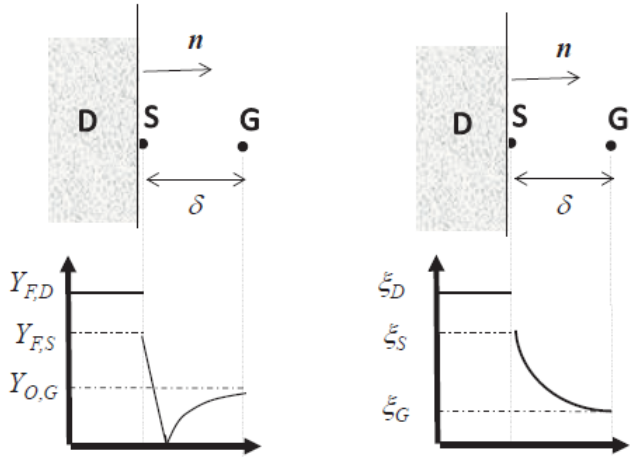

Figure 2.3: Schematic of (left) the mass fraction profile of reactive species Y_F and Y_O and (right) the mixture fraction, ξ.

transfer between a single, isolated liquid fuel particle and an infinite, quiescent gaseous environment as shown schematically in Figure 2.3. The analysis is for one-dimensional heat and mass transfer, which is a convenient simplification applicable to both spherical and long filament fuel particles. The normal outward vector is n. In the following subsections, a mass flux equation is derived from the heat and mass transfer perspective. The simple heat transfer due to conduction can be considered in the diffusive layer. The evaporation process leads to vapour mass away from the interface due to Stefan flow, thus necessitating the inclusion of the convective term in the heat transfer equation.

2.2.2.1 Mixture fraction approach

It is assumed that gaseous heat and mass transfer are quasi-steady, meaning that the timescale of transport in the gaseous layer is small relative to timescales in the dispersed phase. The left side of Figure 2.3 shows the profile of an evaporative reactive fuel species, Y_F, which has a uniform value in the fuel particle, a surface discontinuity due to a jump condition, and diffusion to the reaction zone where it is consumed. On the outer side of the reaction zone an oxidizer species, Y_O, is shown. Turns [8] circumvents this by

introducing an additional boundary condition at the reaction zone which is assumed to be infinitely thin. In practice, reactions proceed at finite rates resulting in broadened reaction zones which may even become broken due to intense turbulent mixing or quenching. A more general solution is obtained by considering conserved scalars such as the mixture fraction shown on the right side of Figure 2.3. Conserved scalars are not affected by chemical reactions alleviating the above-mentioned problem. This is because Y_F varies non-monotonically in the diffusion layer around the droplet, whereas conserved scalars are monotonic and have a known analytical distribution (for ideal cases). Mixture fraction is defined as the normalisation of any conserved scalar β as

$$\xi = \frac{\beta - \beta_o}{\beta_1 - \beta_0} \tag{2.7}$$

where subscripts 0 and 1 represent the values in pure oxidizer and pure fuel respectively. ξ has the same definition in both the dispersed and gas phases. For mass transfer from fuel particles without gas phase combustion, the mass fraction of the transferred species is a conserved scalar and it is natural to set $\beta = Y_F$. Under combustion conditions molecular species are not conserved but atomic elements are, so $\beta = Y_e$, can be written, where e can represent any element (assuming differential diffusivity is not important). The standardised enthalpies in the dispersed and gas phases are defined as

$$\hat{h}_D = C_{p,D}(T_D - T^r) \tag{2.8}$$

$$\hat{h}_G = \sum_{\alpha=1}^{N_s} \left[h_f^r + \int_{T_r}^{T^G} C_p dT \right]_\alpha \tag{2.9}$$

where C_p is the specific heat, T_r is a reference temperature and h_f is enthalpy of formation.

2.2.2.2 Heat transfer perspective

The governing equations for liquid phase modelling start from the heat and mass transfer perspective and these two perspectives are combined to derive an expression for mass flux from the dispersed phase to the gas phase. First, the heat transfer equations are written from which the unclosed terms are identified and closed by boundary conditions and another expression is equated for mass flux in the mass transfer perspective.

The second order enthalpy equation in the diffusive layer can be written as

$$\rho\alpha\frac{\partial^2\hat{h}}{\partial n^2} - \rho v\frac{\partial\hat{h}}{\partial n} = 0 \tag{2.10}$$

Since the above heat transfer equation is based on standardised enthalpy which includes both enthalpies of formation and sensible enthalpy, it attributes both heat and mass diffusion. Mass diffusion is not included for this derivation assuming a unity Lewis number; i.e. the above equation is valid for $Le = 1$. Integrating the above equation between S state where $n = 0$ and a remote point from the S state but still within the diffusive layer can be written as

$$\rho\alpha\frac{\partial\hat{h}}{\partial n} - \rho\alpha\frac{\partial\hat{h}}{\partial n}|_S - \dot{m}''(\hat{h} - \hat{h_S}) = 0 \tag{2.11}$$

where ρv is substituted as mass flux, $\dot{m}''$. The boundary conditions as shown in Figure 2.4 incorporate heat fluxes for radiation, $\dot{Q}''_R$, net heat flux to the particle, $\dot{Q}''_D$ and latent heat of phase change, $(\hat{h_S} - \hat{h_D})$, which is balanced by conductive heat transfer from the gas phase. Following convention, radiation outwards from the fuel particle has a negative value. Therefore the boundary condition in Figure 2.4 can be written as

$$\dot{Q}''_D = \rho\alpha\frac{\partial\hat{h}}{\partial n}|_S - \dot{m}''(\hat{h_S} - \hat{h_D}) + \dot{Q}''_R \tag{2.12}$$

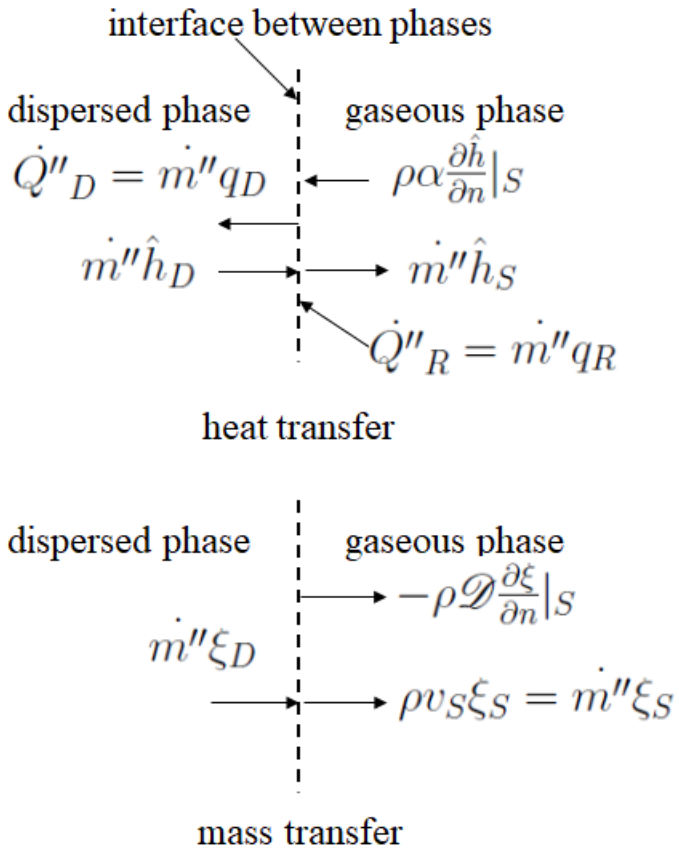

Figure 2.4: Heat and mass transfer interface boundary conditions

In the above equation $(\hat{h_S} - \hat{h_D})$ is the enthalpy difference due to the latent heat of evaporation for liquid fuel related to surface conditions. Applying this surface condition and expressing the intensive form of quantities multiplied by mass flux, the heat transfer equation takes the form as

$$\rho\alpha\frac{\partial\hat{h}}{\partial n} - \dot{m}''(\hat{h_S} - \hat{h_D}) + q_D - q_R + (\hat{h} - \hat{h_S}) = 0 \tag{2.13}$$

Integrating Eqn. 2.13 between S and G state from $n = 0$ to characteristic thickness of layer, δ_H and rearranging an algebraic expression for mass flux as following

$$\dot{m}'' = \frac{\rho\alpha}{\delta_H} ln(1 + B_H) \tag{2.14}$$

where B_H is the Spalding number for heat transfer as

$$B_H = \frac{\hat{h_G} - \hat{h_S}}{\hat{h_S} - \hat{h_D} + q_D - q_R} \tag{2.15}$$

The expression for mass flux Eqn. 2.14 is valid for any particle shapes and different coordinate systems. A thorough derivation for the spherical coordinate system is available in the literature [8]. For the spherical fuel particles, it is better to replace δ_H by an expression which effectively combines heat and mass transfer between gaseous and dispersed phases for different particle sizes. For generality, the Nusselt number is introduced here as $Nu = L/\delta_H$, which is a dimensionless number [133]. The characteristic length, L can be replaced by particle diameter, D^{fp}, which will give correct mass flux at the surface of the spherical fuel particle [8]. It indicates a decrease in the diffusion characteristic length due to convection increases Nu leading to enhancement of transfer rate. For quiescent conditions around a sphere, the lower limit of $Nu = 2$ and it can increase further for convective conditions. The final form of expression for mass flux in the heat transfer perspective is

$$\dot{m}'' = Nu\frac{\rho\alpha}{L}ln(1 + B_H) \tag{2.16}$$

The unknown quantities in the above equations (Eqns. 2.16 and 2.15) are q_D, q_R and the enthalpies of three phases such as $\hat{h}_G$, $\hat{h}_S$ and $\hat{h}_D$. Enthalpy is a function of temperature and composition, $\hat{h} = f(\xi, T)$. Assuming gas temperature (T_G) is available from the gas phase simulation, the unknown temperatures are T_S and T_D. Following simple convention, the surface temperature (T_S) can be assumed equal to the dispersed phase particle temperature (T_D). With this simplification, the particle temperature is

calculated by lumped heat capacity assumption by solving an unsteady ODE equation

$$m_D C_{p,D} \frac{dT_D}{dt} = \dot{m}'' A q_D \tag{2.17}$$

where m_D is the mass of the fuel particle, $C_{p,D}$ is the specific heat of fuel particle and A is the surface area.

2.2.2.3 Mass transfer perspective

The governing equations for mass flux are derived here from the perspective of mass transfer in the diffusive layer. The second order mass transfer equation is derived considering a single evaporative species with mixture fraction as

$$\rho \mathscr{D} \frac{\partial^2 \xi}{\partial n^2} - \rho v \frac{\partial \xi}{\partial n} = 0 \tag{2.18}$$

The Eqn. 2.18 is integrated twice between S and an arbitrary point in the diffusive layer. Again substituting $\dot{m}'' = \rho v$ the first integration form is

$$\rho \mathscr{D} \frac{\partial \xi}{\partial n} - \rho \mathscr{D} \frac{\partial \xi}{\partial n}|_S - \dot{m}''(\xi - \xi_S) \tag{2.19}$$

The boundary conditions are shown in the Figure 2.4 (in the bottom interface condition) and can be written as

$$\dot{m}'' \xi_D = \dot{m}'' \xi_S - \rho \mathscr{D} \frac{\partial \xi}{\partial n}|_S \tag{2.20}$$

Applying boundary conditions for mass flux to be positive from the dispersed to gas phase as convention and normalising mixture fraction of dispersed phase as unity and simplying

the Eqn 2.19 the following expression can be written

$$\rho\mathscr{D}\frac{\partial\xi}{\partial n} - \dot{m}''(\xi - 1) = 0 \tag{2.21}$$

Integrating Eqn. 2.21 between S and G states and simplifying, an algebraic expression for mass flux is

$$\dot{m}'' = \frac{\rho\mathscr{D}}{\delta_M} ln(1 + B_M) \tag{2.22}$$

where δ_M is the diffusive layer thickness for mass transfer. Since species have equal diffusivity and unity Lewis number ($Le = \alpha/\mathscr{D} = 1$), the film thickness is equal for heat and mass transfer cases ($\delta_H = \delta_M$). The transfer number defined as B_M [29] is

$$B_M = \frac{\xi_G - \xi_S}{\xi_S - 1} \tag{2.23}$$

For the mass transfer perspective, the dimensionless Sherwood [134] number is introduced here for simplification of the diffusive layer film thickness, which is similar to the heat transfer perspective assumptions and expression in Eqn. 2.16, so the final form of mass flux equation for the mass transfer perspective is

$$\dot{m}'' = Sh\frac{\rho\mathscr{D}}{L} ln(1 + B_M) \tag{2.24}$$

The Sherwood number is introduced here, which is a function of Reynolds and Schmidt numbers. In this study, spherical fuel particles are considered for simulation and the Ranz-Marshall correlation is used for Nu and Sh [134]. Now, there are two expressions for mass flux but from different perspectives and with different transfer numbers. For

closing the systems of equations and equating the two mass flux equation as

$$Nu\frac{\rho\alpha}{L}ln(1+B_H) = Sh\frac{\rho\mathscr{D}}{L}ln(1+B_M) \tag{2.25}$$

simplifies to

$$1+B_H = (1+B_M)^Z \tag{2.26}$$

where $Z = Le^{-1}Sh/Nu$. For the unity Lewis number, the two transfer numbers are equal so that $B_H = B_M$.

From Eqn. 2.15 and substituting the expression for B_H, the closure for q_D is found as following

$$q_D = \frac{\hat{h}_G - \hat{h}_S}{(1+B_M)^Z - 1} - (\hat{h}_S - \hat{h}_D) + q_R \tag{2.27}$$

The above Eqn. 2.27 is a final expression for the internal heating of the particle. A new unknown is introduced here, which is a surface mixture fraction term, ξ_S, which is closed by the evaporation model in the next subsection.

A unclosed term for radiation heat transfer, q_R, is modelled by a simple thin gas radiation as following

$$q_R = \sigma(T_D^4 - T_W^4) \tag{2.28}$$

where σ is Stefan-Boltzman constant and its value is -5.6703e-08 W/m^2K^4, T_W is wall temperature.

2.2.2.4 Evaporation model

A model for the species mass fraction in the surface of the fuel particle is required for applying interface conditions. For this study, Clausius-Clapeyron phase equilibrium relation is used. For a single fuel component evaporating air, the equilibrium equation is defined as

$$Y_{\alpha,S} = \left[1 + \frac{MW_{air}}{MW_{\alpha}} \left(\frac{P}{P_{\alpha}} - 1\right)\right]^{-1} \tag{2.29}$$

where MW_{air} and MW_{α} are the molecular weight of air and species α, P is the thermodynamic pressure and P_{α} is the vapour pressure of evaporative species. The thermodynamic pressure P may be assumed as atmospheric at low a Mach number.

2.2.2.5 Note about the numerical implementation

Finally, the values of $\hat{h}$ and ξ are required at the 'S' and 'G' states. These are abstracted with information from the turbulent gas phase combustion model (e.g. MMC-LES [135] or CMC-LES [136]), which provides reactive species at the 'G' state. ξ_G is also available from the gas phase MMC combustion model. For this study, ξ_S is found directly from evaporation of the liquid fuel model. For the species mixture fraction, it is assumed that a species, i, is a unique function of the mixture fraction; $Y_i = f(\xi)$, where the gas-phase combustion model gives f. The inverse function then gives $\xi_S = f^{-1}(Y_i)$ with $Y_{i,S}$ being determined by the process dependent interface conditions such as the evaporation process. The values of $\hat{h}_G$ and $\hat{h}_S$ are then obtained as a function of the mixture fraction and temperature. Once the enthalpies of S, D and G state are available, then the transient simulation starts according to modelling equations developed in this

chapter. As the surrounding carrier phase is heating the particles, the properties of the gas phase will change due to the influence of the dispersed phase. The details of coupling of the Lagrangian liquid particle model with LES and MMC will be covered in Chapter 3.

2.3 Testing of developed model in Matlab-Cantera simulation

For testing the validity of this newly developed liquid phase heat and mass transfer model and its implementation, simulation has been performed for reacting and non-reacting evaporation cases. The results are compared against a number of experimental data for the evaporation of methanol and n-heptane droplets [137, 138]. Numerical simulation has been implemented in Matlab code incorporating the Cantera thermodynamic toolbox [139] for a demonstration of the capability of the model with simple one particle burning and non-burning test cases. The transport parameters for the different cases are the same unless specified in case specific details. For developing a simple model, a unity Lewis number is assumed from which other transport parameters such as viscosity and Schmidt number are calculated as $Sc = \nu/\mathscr{D} = 0.7$. Both $\rho\alpha$ and $\rho\mathscr{D}$ are at film state. The 2/3 rule obtains for both the film mixture fraction and film standardised enthalpy, and the film composition is then calculated from the known flame structure in the diffusive layer. The burning composition is obtained from a precomputed, lightly strained laminar flamelet solution. The thermodynamic properties are obtained from NASA polynomials coefficients [140]. For the liquid droplet cases droplets exposed in a large microgravity environment, $\epsilon = 1$ and $T_W = 300K$ are assumed. The Crank-Nicholson method is

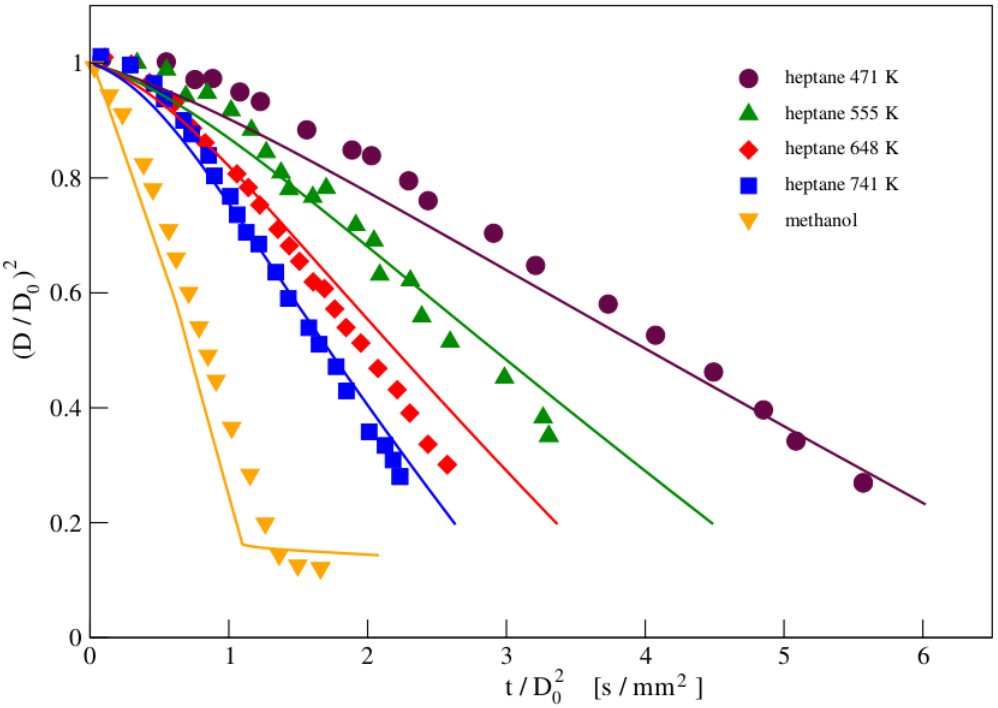

Figure 2.5: Normalised diameter squared versus scaled time for burning methanol and non-burning n-heptane droplets. n-heptane results are for various ambient temperatures. Experimental data [137, 138] - symbols, model results - lines.

applied for integration of non-linear particle temperature in Eqn. 2.17.

The experimental investigation of Dietrich *et al.* [138] is available for droplet burning cases of pure methanol and various mixtures of methanol, water, n-heptane, hexadecane and dodecanol under microgravity conditons on the Spacelab. For this test, only methanol and n-heptane cases are tested here. The experimental droplets range from 2 mm to 5 mm sizes, evaporated and burned in air at 1 atm and 300K with varying Reynolds numbers. The results are presented here for a case in which slip velocity increased slowly from 0 mm/s to 50 mm/s. The experimental investigation was also done by Nomura *et al.* [137] for non-burning cases of microgravity evaporation of n-heptane droplets in nitrogen at pressure ranging from 0.1 MPa to 5 MPa and temperature from 400 K to 800 K. In this test simulation, 0.1 MPa cases are studied only. The mean initial droplet size was 0.7 mm.

Figure 2.5 shows six evaporation cases in the same figure. The results are shown based

on the normalised diameter squared versus time divided by the initial diameter squared. All the cases trend very well with respect to the experimental data, correctly predicting the variations in evaporation rates due to different fuel and ambient temperature. For the methanol case, the model captures some order of magnitude reduction in burning rate due to flame extinction triggered at $t/D_0^2 = 1.4\ s/mm^2$. The methanol case is also showing increased burning rate due to increased Reynolds number at about $1/D_0^2$=1 s/mm^2.

The heat and mass transfer source terms are initiated in gas phase due to multiphase combustion, which was first addressed by Spalding by deriving an expression for mass flux in terms of conserved scalar approach. The contemporary studies applied a specific form of Spalding's transfer relations in terms of non-conserved mass fraction approach. In this study, the conserved scalar approach is re-introduced by mixture fraction approach, which fits well with the overall mixture fraction approach of MMC-LES framework. The liquid phase model is derived in this chapter with the aim of applying it in Lagrangian particle based model. The dispersion of fuel particles is modelled by the approach developed by Dukowicz [130]. The test simulations are performed by Matthew Cleary for reacting and non-reacting evaporation cases into an unsteady Matlab-Cantera solver. The model is tested for different evaporative fuels, oxidizer composition and Reynolds number with the presence or absence of envelope flames. A good agreement is found between the model prediction and experimental data. This novel model would seem to be a natural framework for multiphase combustion model that can be used in conjunction with the conserved scalar models for the gas phase, such as CMC or MMC. For this study, this model has been cast with MMC gas phase model for multiphase combustion model.

Chapter 3

The Multiphase sparse Lagrangian MMC-LES combustion model

Multiphase governing transport equations are derived in this section based on the concept of separated dilute two-phase flow. The measured liquid volume fractions for both reacting and non-reacting acetone cases of this study at *z/D=0.3* were equal to either 1% or less and the droplet-droplet interaction was negligible due to larger separation between droplets [1], which are conditions for dilute flow condition. The starting point is the instantaneous transport equations which are valid in the interior of each phase. A phase-weighted spatial filtering operation is then applied to the instantaneous LES equations from which the filtered moment equations and filtered mass density function transport equations are derived.

3.1 Instantaneous transport equations

For simulation of sprays, the internal flow within the dispersed phase is not considered here, rather the dispersed liquid fuel particles are treated as liquid points with negligible internal gradients of velocity and species concentration in the final simplification of the model. The local and instantaneous continuity, species mass fraction and standardised enthalpy transport equations within the interior of a single phase of a two-phase flow are:

$$\frac{\partial \rho_k}{\partial t} + \frac{\partial \rho_k u_{k,i}}{\partial x_i} = 0 \tag{3.1}$$

$$\frac{\partial \rho_k u_{k,i}}{\partial t} + \frac{\partial \rho_k u_{k,i} u_{k,j}}{\partial x_j} = -\frac{\partial P_k}{\partial x_i} + \frac{\partial \tau_{k,ij}}{\partial x_j} + \rho_k a_{k,i} \tag{3.2}$$

$$\frac{\partial \rho_k Y_{\alpha,k}}{\partial t} + \frac{\partial \rho_k u_{k,i} Y_{\alpha,k}}{\partial x_i} = -\frac{\partial J_{\alpha,k,i}}{\partial x_i} + \partial \rho_k W_{\alpha,k} \tag{3.3}$$

$$\frac{\partial \rho_k \hat{h}_k}{\partial t} + \frac{\partial \rho_k u_{k,i} \hat{h}_k}{\partial x_i} = -\frac{\partial J_{h,k,i}}{\partial x_i} + \rho_k W_{h,k} \tag{3.4}$$

In the above Eqns. 3.1 to 3.4, subscript $k \in [1,2] = [D,G]$ is the phase index, i the coordinate index and α the species index, a_i the acceleration due to drag force imparted by the other phase. $J_{\alpha,i}$ and $J_{h,i}$ are the mass and heat diffusion respectively so that $J_{\alpha,i} = \rho_k \mathscr{D}_{\alpha,k} \frac{\partial Y_{k,\alpha}}{\partial x_i}$ and $J_{h,i} = \rho_k \mathscr{D}_{h,k} \frac{\partial \hat{h}_k}{\partial x_i}$ assuming mass and heat diffusions follow Fickian law. W_α and W_h are the chemical reaction rate and radiation heat transfer respectively for the chemical species. The Eqns. 3.1 to 3.4 are valid within the interior of each phase, but they are not valid in the phase interface where momentum, mass and heat transfer between the phases may take place. In this study, the governing equations are extended to the phase interface by introducing the separated two phase model originally introduced by Kataoka

[141] and used by Mortensen and Bilger [142] for CMC spray.

Introducing a field variable $\gamma(x,t)$ so that $\gamma = \gamma^I$ at the interface, $\gamma < \gamma^I$ at the dispersed phase and $\gamma > \gamma^I$ at the gas phase. The interface can be tracked through the level set function as

$$\frac{\partial \gamma}{\partial t} + \mathbf{u}^I.\nabla\gamma = 0 \tag{3.5}$$

where $\mathbf{u}^I$ is the interface velocity. The Eqn. 3.5 is expressed in terms of the phase velocity by adding and subtracting $u_k.\nabla\gamma$ as following

$$\frac{\partial \gamma}{\partial t} + u_k.\nabla\gamma = S_k[-(u^I - u_k).n_1|\nabla\gamma|] \tag{3.6}$$

where n_1 is the unit normal vector pointing from phase 1 to phase 2. The above equation can be used to track which phase is present at location x and time t. The tracking of phases is not done directly here, rather this is done by manipulating the level set function to obtain the governing equation that holds both phases and interface. The governing equations are derived by weighting through a phase indicator θ_K which is unity in the phase k and zero in the other phase. The phase indicator function is expressed as

$$\theta_k = 0^{k-1} + (-1)^k H(\gamma - \gamma^I) \tag{3.7}$$

where H is the Heaviside function. The transport equation for θ_k is [141]

$$\frac{\partial \theta_k}{\partial t} + \mathbf{u}_k.\nabla\theta_k = \Pi_k \left[(-1)^k S_k \delta(\gamma - \gamma^I)\right] \tag{3.8}$$

where Π_k is the volumetric rate of mass transfer per unit normalising volume (unit [1/s]) locally at the phase interface. For the two phases: the dispersion mass transfer rate, $\Pi_D = \dot{m}_D/(\rho_D V)$ and the gaseous mass transfer rate, $\Pi_G = \dot{m}_G/(\rho_G V)$, where V is the

normalising volume, usually it is LES cell volume, V^{eu}. Since $\dot{m}_G = -\dot{m}_D$, which leads to $\rho_G \Pi_G = -\rho_D \Pi_D$.

Multiplying Eqns. (3.1) - (3.4) by θ_k and applying the chain rule, the phase-weighted continuity, momentum, species and standardised enthalpy transport equations can be written as

$$\frac{\partial \theta_k \rho_k}{\partial t} + \frac{\partial \theta_k \rho_k u_{k,i}}{\partial x_i} = \rho_k \Pi_k \tag{3.9}$$

$$\frac{\partial \theta_k \rho_k u_{k,i}}{\partial t} + \frac{\partial \theta_k \rho_k u_{k,i} u_{k,j}}{\partial x_j} = -\theta_k \frac{\partial P_k}{\partial x_i} + \frac{\partial \theta_k \tau_{k,ij}}{\partial x_j} + \theta_k \rho_k a_{k,i} - \tau_{k,ij} \frac{\partial \theta_k}{\partial x_j} + \rho_k u_{k,i} \Pi_k \tag{3.10}$$

$$\frac{\partial \theta_k \rho_k Y_{\alpha,k}}{\partial t} + \frac{\partial \theta_k \rho_k u_{k,i} Y_{\alpha,k}}{\partial x_i} = -\frac{\partial \theta_k J_{\alpha,k,i}}{\partial x_i} + \theta_k \rho_k W_{\alpha,k} + J_{\alpha,k,i} \frac{\partial \theta_k}{\partial x_i} + \rho_k Y_{\alpha,k} \Pi_k \tag{3.11}$$

$$\frac{\partial \theta_k \rho_k \hat{h}_k}{\partial t} + \frac{\partial \theta_k \rho_k u_{k,i} \hat{h}_k}{\partial x_i} = -\frac{\partial \theta_k J_{h,k,i}}{\partial x_i} + \theta_k \rho_k W_{h,k} + J_{h,k,i} \frac{\partial \theta_k}{\partial x_i} + \rho_k \hat{h}_k \Pi_k \tag{3.12}$$

The Eqns. 3.9 to 3.12 are valid in both phases and the phase interface. Since Eqns. 3.10 to 3.12 contain θ_k, it requires closure. Mass, momentum, species and enthalpy cannot be generated in the interface since there is no mass and volume in the interface. Thus the following interface jump conditions can be applied [141]:

$$\sum_{k=1}^{2} \rho_k \Pi_k = 0 \tag{3.13}$$

$$\sum_{k=1}^{2} \left(-\tau_{k,ij} \frac{\partial \theta_k}{\partial x_j} + \rho_k u_{k,i} \Pi_k) \right) = 0 \tag{3.14}$$

$$\sum_{k=1}^{2}\left(J_{\alpha,k,i}\frac{\partial\theta_k}{\partial x_i}+\rho_k Y\alpha,k\Pi_k\right) \tag{3.15}$$

$$\sum_{k=1}^{2}\left(J_{h,k,i}\frac{\partial\theta_k}{\partial x_i}+\rho_k\hat{h}_k\Pi_k\right)=\rho_D\Pi_D\left(q_D-q_R\right) \tag{3.16}$$

Neglecting internal velocity, species and enthalpy gradients within the interior of the dispersed phase particles, the gas phase stress and diffusive flux closures can be found as

$$-\tau_{G,ij}\frac{\partial\theta_G}{\partial x_j}=\rho_G\Pi(u_{D,j}-uG,j) \tag{3.17}$$

$$J_{\alpha,G,i}\frac{\partial\theta_G}{\partial x_i}=\rho_G\Pi\left(Y_{\alpha,D}-Y_{\alpha,G}\right) \tag{3.18}$$

$$J_{h,G,i}\frac{\partial\theta_G}{\partial x_i}=\rho_G\Pi(\hat{h}_D-q_D+q_R-\hat{h}_G) \tag{3.19}$$

where, $\rho_G\Pi_G=\rho_G\Pi=-\rho_D\Pi_D$ can be set in the above equation.

3.2 The LES governing equations

In this study, the LES method is applied which involves a filtering operation. For the turbulent motions, scales larger than the filter are simulated the in Eulerian grid, and scales smaller than the filtering length are modelled. In single phase combustion, the modelled terms include the subfilter viscous stress in the momentum equation, the subfilter mass flux and the filtered chemical reaction rate in the species transport equation. In multiphase combustion additional gas production terms, denoted dispersed-to-gas conversion terms, which are related to the evaporation process of the liquid phase, and heterogeneous

chemical conversion, need to be modelled. Since the rate controlling process for subfilter momentum and mass fluxes is the breakdown of turbulent (i.e. resolved) eddies, these terms can be modelled satisfactorily from the resolved velocity and scaler flux fields. However, the rate controlling process for chemical reactions and gas production terms is unresolved molecular diffusion and cannot be easily modelled using resolved quantities.

From the above understanding, two different sets of filtered equations are derived which then form the basis of subgrid models for the turbulent velocity and turbulent reaction species fields respectively. First, in the conventional LES model, the LES filtered moments (mean and variance) are solved in the Eulerian grid. The second, the stochastic particle model, is developed in the filtered density functions (FDF) approach, where the chemical reactions source term is closed. Since the dispersed phase will be modelled as points without internal gradients, therefore the continuum separated flow equations are relevant only within the gas phase. The subscript G, which represents the gas phase is omitted in this section for clarity to avoid confusion and the subscript D is retained as the dispersed phase. The filtered mean is defined by

$$\bar{\varphi}(x,t) = \int_{-\alpha}^{\alpha} \varphi(x',t) G(x'-x) dx' \tag{3.20}$$

where φ is any general field quantity and G is a kernel function with width Δ^{eu}. In multiphase flows with large density variations, the phase-weighted Favre filtered mean is defined as

$$\tilde{\varphi} = \frac{\overline{\theta\rho\varphi}}{\bar{\theta}\bar{\rho}} \tag{3.21}$$

From the above definition the phase weighted average density

$$\overline{\theta(x,t)}\,\overline{\rho(x,t)} = \int_{-\alpha}^{+\alpha} \theta(x',t)\rho(x',t)G(x'-x)dx' \tag{3.22}$$

Applying phase-weighted Favre filter to Eqns. 3.1 to 3.12 with substitution of the jump conditions in Eqns. 3.17 to 3.19 and some further manipulations give the filtered transport equations as following:

$$\frac{\partial\bar{\theta}\bar{\rho}}{\partial t} + \frac{\partial\bar{\theta}\bar{\rho}\tilde{u}_i}{\partial x_i} = \tilde{\dot{S}}_\rho \tag{3.23}$$

$$\frac{\partial\bar{\theta}\bar{\rho}\tilde{u}_i}{\partial t} + \frac{\partial\bar{\theta}\bar{\rho}\tilde{u}_j\tilde{u}_j}{\partial x_j} = -\bar{\theta}\frac{\partial\bar{P}}{\partial x_i} + \frac{\partial\bar{\theta}\tilde{\tau_{ij}}}{\partial x_j} - \frac{\partial\bar{\theta}\tau_{ij}^{sgs}}{\partial x_j} + \tilde{\dot{S}}_{u,i} \tag{3.24}$$

$$\frac{\partial\bar{\theta}\bar{\rho}\widetilde{Y}_\alpha}{\partial t} + \frac{\partial\bar{\theta}\bar{\rho}\tilde{u}_i\widetilde{Y}_\alpha}{\partial x_i} = -\frac{\partial\bar{\theta}\tilde{J}_{\alpha,i}}{\partial x_i} - \frac{\partial\bar{\theta}J_{\alpha,i}^{sgs}}{\partial x_i} + \tilde{\dot{S}}_\alpha \tag{3.25}$$

$$\frac{\partial\bar{\theta}\bar{\rho}\widetilde{\hat{h}}}{\partial t} + \frac{\partial\bar{\theta}\bar{\rho}\widetilde{u}_i\widetilde{\hat{h}}}{\partial x_i} = -\frac{\partial\bar{\theta}\widetilde{J_{h,i}}}{\partial x_i} - \frac{\partial\bar{\theta}J_{h,i}^{sgs}}{\partial x_i} + \widetilde{\dot{S}_h} \tag{3.26}$$

where the filtered source terms are

$$\widetilde{\dot{S}}_\rho = \bar{\rho}\widetilde{\Pi} \tag{3.27}$$

$$\widetilde{\dot{S}}_{u,i} = \bar{\theta}\bar{\rho}\tilde{a}_i + \widetilde{\bar{\rho}u_{D,i}\Pi} \tag{3.28}$$

$$\widetilde{\dot{S}}_\alpha = \bar{\theta}\bar{\rho}\tilde{W}_\alpha + \bar{\rho}Y_{\alpha,D}\widetilde{\Pi} \tag{3.29}$$

$$\widetilde{\dot{S}_h} = \bar{\theta}\bar{\rho}\widetilde{W_h} + \bar{\rho}\langle(\hat{h}_D - q_D + q_R)\Pi\rangle \tag{3.30}$$

The above filtered equations contain a number of unclosed terms: $\bar{\theta}$ is the volume fraction

of the gas phase, which is approximated as unity for dilute flows; τ_{ij}^{sgs} is the subgrid viscous stress tensor, $\tilde{J}_{\alpha,i}^{sgs}$ is the subgrid mass flux, and $\tilde{\dot{S}}$ is the non-linear source terms. As chemical reaction and gas production occur at the unresolved scales, simple closure is not readily available. The subgrid models are derived for closing the above source terms. The LFP model is already derived in chapter 2 and the FDF formulation is derived in the next section leading to another subgrid model for the chemical reaction source term.

3.3 Subgrid models

Finally, this study implements a sparse Lagrangian MMC-LES combustion model in LES and the governing equations are derived in the previous section, where the unclosed source terms are taken care of by the subgrid models.

The subgrid models are summarised in this section as followings:

- Lagrangian Fuel Particle Model (derived in Chapter 2)
- The LES Mass and Momentum Model
- The Sparse Lagrangian MMC Model

In this section, superscripts eu, fp and sp are introduced to denote values in Eulerian cell centres, fuel particle/parcel locations and MMC/FDF stochastic notional particle locations to identify which value of a particular quantity is being referred to. The subscripts remain as the previous chapter as following: for states G, D and S; for species, α; and for coordinate, i. For dilute two-phase assumption; $\bar{\theta}_G = 1$ is used throughout. It is possible to track individual particles for a very small number of fuel particles and for cases with very high dilution [136]. However, to save computational expense for this

study, tracking of particles is done by parcels which represent ensembles of real fuel particles with identical properties such as location, velocity, mass and temperature. The Lagrangian fuel particle model has been already derived in chapter 2. The other two models are derived in the following subsections.

3.3.1 The LES mass and momentum model

The filtered moment Eqn. 3.24 is solved for three components of the velocity vector. The unclosed term, $\widetilde{\tau}_{ij}^{sgs}$, is closed by a Smargorinsky-type closure [143] with a dynamic parameter [144]. The source terms for filtered mass and momentum resulting from mass and momentum exchange between phases are evaluated with information from the Largrangain fuel particles model by summing over all particles, $N_{fp,LES}$, within the filter volume, V^{eu}, [145] according to Eqn. 3.24. following:

$$\widetilde{\dot{S}}_{\rho}^{eu} = \rho^{-eu}\widetilde{\Pi}^{eu} \backsimeq \frac{1}{V^{eu}} \sum_{fp=1}^{N_{fp,LES}} \dot{m}_D^{fp} \tag{3.31}$$

$$\widetilde{\dot{S}}_{u,i}^{eu} = \theta^{-eu}\rho^{-eu}\widetilde{a_i}^{eu}\widetilde{u_{D,i}}\Pi^{eu} \backsimeq \frac{1}{V^{eu}} \sum_{fp=1}^{N_{fp,LES}} \left(-\dot{m}_D^{fp} a_{D,i}^{fp} + \dot{m}_D^{fp} u_{D,i}^{fp}\right) \tag{3.32}$$

The filtered mean of reactive species is solved via FDF equations instead of solving Eqn. 3.25. For the gas phase mixture fraction $\widetilde{\xi}_G^{eu}$, the filtered mean is solved and used as a reference variable for the FDF equations. Eqn. 3.25 is simplified to the following form using $\theta = 1$ and with the chemical source term set zero

$$\frac{\partial \rho_G^{-eu}\widetilde{\xi_G^{eu}}}{dt} + \frac{\partial \rho_G^{-eu}\widetilde{u}_{G,i}^{eu}\widetilde{\xi}_G^{eu}}{\partial x_i} = -\frac{\partial \widetilde{J}_{\xi,G,i}^{eu}}{\partial x_i} - \frac{J_{\xi,G,i}^{sgs,eu}}{\partial x_i} + \widetilde{\dot{S}}_{\xi}^{eu} \tag{3.33}$$

where

$$\widetilde{\dot{S}}_{\xi}^{eu} = \frac{1}{V^{eu}} \sum_{fp=1}^{N_{fp,LES}} \dot{m}_D^{fp} \tag{3.34}$$

The Eqn. 3.34 has the same form as $\widetilde{\dot{S}}_{\rho}^{eu}$ in Eqn. 3.31. The two expression follows the substitution as $Y_{\alpha,D} = 1$ for $\xi_D = 1$ into Eqn. 3.29. In Eqn. 3.33, for $\widetilde{J}_{\xi,G,i}^{sgs,eu}$ an eddy diffusivity model similar to the Smagorinsky model is used.

3.3.2 The sparse Lagrangian MMC model

In the FDF method, subfilter turbulent fluctuations of the reactive species and enthalpy field $\phi = \left(Y_1, ..., Y_\alpha, ..., Yn_s, \hat{h}\right)$ are represented probabilistically by the phase-weighted filtered mass density function, F, defined as

$$F(\Psi; x, t) = \int_{-\alpha}^{+\alpha} \theta(x', t)\rho(x', t)\zeta[\Psi, \phi(x, t)]G(x' - x)dx' \tag{3.35}$$

where Ψ is the sample space for ϕ and the fine-grained density, ζ, is given by the n_s+1 dimensional delta function

$$\zeta[\Psi, \phi(x, t)] = \delta[\Psi - \phi(x, t)] = \prod_{n=1}^{n_s+1} \delta[\Psi_n - \phi_n(x, t)] \tag{3.36}$$

From Eqn. 3.22 and Eqn. 3.35, integration of F in Ψ yields the phase-weighted filtered density as

$$\int_{-\alpha}^{+\alpha} F(\Psi; x, t)d\Psi = \bar{\theta}(x, t)\bar{\rho}(x, t) \tag{3.37}$$

Furthermore, defining the conditional Favre filtered mean of some variable Q as

$$\overline{Q(x, t)|\Psi} = \frac{\int_{-\alpha}^{+\alpha} \theta(x', t)Q(x', t)\zeta[\Psi, \phi(x't)]G(x' - x)dx'}{F(\Psi; x, t)} \tag{3.38}$$

its unconditional filtered mean can be found as

$$\tilde{Q}(x,t) = \frac{1}{\bar{\theta}\bar{\rho}} \int_{-\alpha}^{+\alpha} \overline{Q(x,t)|\Psi} F(\Psi;x,t) d\Psi \tag{3.39}$$

Deriving the transport equation for F starting from the generalised time derivative of the fine grained density as

$$\frac{\partial \zeta}{\partial t} = -\frac{\partial}{\partial \Psi_n}\left(\zeta \frac{\partial \phi_n}{\partial t}\right) \tag{3.40}$$

weighting this equation by $\theta\rho$ and manipulating with the chain rule gives

$$\frac{\partial \theta\rho\zeta}{\partial t} - \zeta\frac{\partial \theta\rho}{\partial t} = -\frac{\partial}{\partial \Psi_n}\left[\zeta\left(\frac{\partial \theta\rho\phi_n}{\partial t} - \phi_n \frac{\partial \theta\rho}{\partial t}\right)\right] \tag{3.41}$$

Substituting Eqn. 3.9 and Eqn. 3.11 while incorporating the jump conditions of Eqn. 3.13 and Eqn. 3.15 gives

$$\begin{aligned}\frac{\partial \theta\rho\zeta}{\partial t} - \zeta\left(-\frac{\partial \theta\rho u_i}{\partial x_i} + \rho\Pi\right) = -\frac{\partial}{\partial \Psi_n}\Bigg[\zeta\Bigg(-\frac{\partial \theta\rho u_i\phi_n}{\partial x_i} + \frac{\partial \theta J_{n,i}}{\partial x_i} + \\ \theta\rho W_n + \rho\phi^*_{n,D}\Pi - \phi_n\left(-\frac{\partial \theta\rho u_i}{\partial x_i} + \rho\Pi\right)\Bigg)\Bigg]\end{aligned} \tag{3.42}$$

With further manipulation this becomes

$$\begin{aligned}\frac{\partial \theta\rho\zeta}{\partial t} + \frac{\partial \theta\rho u_i\zeta}{\partial x_i} = -\frac{\partial}{\partial \Psi_n}\Bigg[\Bigg(\frac{\partial \theta J_{n,i}}{\partial x_i}\zeta + \theta\rho W_n\zeta + \\ \rho\Pi\left(\phi^*_{n,D} - \phi_n\right)\zeta\Bigg)\Bigg] + \rho\Pi\zeta\end{aligned} \tag{3.43}$$

In the above equation; $\phi^*_{n,D} = \phi_{n,D}$ for $n \in [1,n]$ and $\phi^*_{n,D} = \phi_{n,D} - q_D + q_R$ for $n = n_s + 1$

Finally weighting by the filtering kernel, G, and integrating this last equation according to the definition in Eqn. 3.35 and Eqn. 3.38 gives the exact (unclosed) FDF transport

equation:

$$\frac{\partial F}{\partial t} + \overline{\frac{\partial u_i|\Psi}{\partial x_i}F} = \frac{\partial}{\partial \Psi_n}\left[\left(\overline{\frac{1}{\theta\rho}\frac{\partial \theta J_{n,i}}{\partial x_i}|\Psi} - W_n(\Psi) - (\phi^*_{n,D} - \psi_n)\overline{\frac{\Pi}{\theta}|\Psi}\right)F\right] + \overline{\frac{\Pi}{\theta}|\Psi}F \tag{3.44}$$

Since the statistics of the instantaneous, local composition field are fully described by F the source term is in closed form $\overline{W_n|\Psi} = W_n(\Psi)$. The conditional convective and diffusive fluxes and conditional gas production terms, however, are unclosed and require modelling. This is to be discussed in turn.

Decomposing the conditional velocity into its filtered and subfilter components

$$\overline{u_i|\Psi}F = \tilde{u_i}F + \left(\overline{u_i|\Psi} - \tilde{u_i}\right)F \tag{3.45}$$

a closure is obtained through use of the gradient diffusion model as

$$\left(\overline{u_i|\Psi} - \tilde{u_i}\right)F = -\bar{\theta}\bar{\rho}\mathscr{D}_t\frac{\partial F/\bar{\theta}\bar{\rho}}{\partial x_i} \tag{3.46}$$

where $\mathscr{D}_t$ is a turbulent diffusivity. Similarly, decomposing the conditional diffusive flux term into resolved and subfilter parts with substitution of a gradient subfilter diffusive flux yields

$$\frac{\partial}{\partial \Psi_n}\left[\overline{\frac{1}{\theta\rho}\frac{\partial \theta J_{n,i}}{\partial x_i}|\Psi}F\right] = \frac{\partial}{\partial x_i}\left(\bar{\theta}\bar{\rho}\mathscr{D}\frac{\partial F/\bar{\theta}\bar{\rho}}{\partial x_i}\right) - \frac{\partial^2}{\partial \Psi_n \partial \Psi_m}\left[\overline{\mathscr{D}\frac{\partial \phi_n}{\partial x_i}\frac{\partial \phi_m}{\partial x_i}|\Psi}F\right] \tag{3.47}$$

where to ensure consistency with the filtered reactive species Eqn. 3.25 it has been assumed that

$$\frac{\partial}{\partial x_i}\left(\bar{\theta}\bar{\rho}\mathscr{D}\frac{\partial F/\theta(\Psi)\rho(\Psi)}{\partial x_i}\right) = \frac{\partial}{\partial x_i}\left(\bar{\theta}\bar{\rho}\mathscr{D}\frac{\partial F/\bar{\theta}\bar{\rho}}{\partial x_i}\right) \tag{3.48}$$

The first term on the right hand side of Eqn. 3.47 accounts for the resolved-scale diffusive

flux and the second term is the still unclosed subfilter conditional scalar dissipation. Its closure is discussed in the context of the sparse Lagrangian MMC formulation of the FDF. The last term on the right hand side of Eqn. 3.44 accounts for the effects of gas production on the shape of the gas-phase reactive species distribution. Since we require that the first moment of Eqn. 3.44 be consistent with Eqn. 3.25, the following relation is set

$$\overline{\frac{\Pi}{\theta}|\Psi F} = \frac{1}{\bar{\theta}}\overline{\Pi|\Psi} F \tag{3.49}$$

For evaporation, simple models for $\overline{\Pi|\Psi}$ exist [146, 147, 148, 136], whereas possible closures for solid fuels such as coal can be found in [149, 150]. A simple model for $\overline{\Pi|\Psi}$ found in both PDF [148] and CMC [146, 136] publications is

$$\overline{\Pi|\Psi} = \frac{\widetilde{\Pi}\delta(\psi - \phi_{gas})}{F} \tag{3.50}$$

where ϕ_{gas} is the mixture at which the gas production impulse occurs. An even simpler model in the recent FDF model of Hey *et al.* [147] is to set as

$$\overline{\Pi|\Psi} = \widetilde{\Pi} \tag{3.51}$$

Both of the models are dimensionally consistent and computationally convenient as they have conditional evaporation as a simple function of the unconditional evaporation rate. However, neither of the models is physically correct. The proposed sparse Lagrangian MMC approach allows for more advanced closures of $\overline{\Pi|\Psi}$ that is discussed in the next subsection. For now it is $\overline{\Pi|\Psi} = \Pi(\Psi)$ to indicate that a closed form exists.

Incorporating the above closures but retaining the unclosed forms of the subfilter

conditional dissipation for FDF equation becomes

$$\frac{\partial F}{\partial t}+\left(\widetilde{u}_i F-\bar{\theta}\bar{\rho}\left(\mathscr{D}+\mathscr{D}_t\right)\frac{\partial F/\bar{\theta}\bar{\rho}}{\partial x_i}\right)=-\frac{\partial}{\partial\Psi_n}\left[\left(W_n(\Psi)+\left(\phi^*_{n,D}-\Psi_n\right)\frac{\Pi(\Psi)}{\bar{\theta}}\right)F\right]-\frac{\partial^2}{\partial\Psi_n\partial\Psi_m}\left(\overline{\mathscr{D}\frac{\partial\phi_n}{\partial x_i}\frac{\partial\phi_m}{\partial x_i}|\Psi}F\right)+\frac{\Pi(\Psi)}{\bar{\theta}}F \tag{3.52}$$

The FDF transport Eqn. 3.52 is (n_s+3) dimensional including mixture fraction, standardised and conditonal enthalpies [2], where $n_s \gg 1$ for any realistic treatment of the chemical kinetics. The cost of the finite difference scheme would increase exponentially with the number of dimensions for computing F. In this study, equivalent stochastic differential equations are solved using the stochastic Lagrangian particle scheme for which cost increases approximately linearly with the number of dimensions. The Eqn. 3.52 is replaced by the following stochastic differential equations

$$dx_i^{sp}=\left[\widetilde{u}_{G,i}^{sp}+\frac{1}{\bar{\rho}_G^{sp}}\left(\frac{\partial}{\partial x_i}\left(\bar{\rho}\left(\mathscr{D}+\mathscr{D}_t\right)_G^{sp}\right)\right)\right]dt+\left[\sqrt{2(\mathscr{D}+\mathscr{D}_t)_G^{sp}}\right]d\omega_i \tag{3.53}$$

$$dY_{\alpha,G}^{sp}=\left[W_\alpha^{sp}+M_{\alpha,G}^{sp}+\left(Y_{\alpha,D}^{sp}-Y_{\alpha,G}^{sp}\right)\Pi^{sp}\right]dt \tag{3.54}$$

$$d\hat{h}_G^{sp}=\left[W_h^{sp}+M_{h,G}^{sp}+\left(\hat{h}_D^{sp}-q_D^{sp}+q_R^{sp}-\hat{h}_G^{sp}\right)\Pi^{sp}\right]dt \tag{3.55}$$

$$dm^{sp}=\frac{m^{sp}\Pi^{sp}dt}{1-\Pi^{sp}dt} \tag{3.56}$$

where, Eqn. 3.53 is a stochastic model for the spatial transport term on the LHS of Eqn. 3.52.

The model for transport in composition space due to reaction, gas production and mixing is represented by Eqn. 3.54 and Eqn. 3.55. Finally, dm^{sp} accounts for the change mass of the stochastic particles due to gas production. In the gas production term, the

conditional volumetric transfer rate, $\Pi^{sp} \simeq \Pi(\eta)$ represents coupling between the LFP and MMC numerical schemes. Moreover, the values of $Y_{\alpha,D}$ and $\hat{h}_D - q_D + q_R$, all of which are terms associated with fuel particles, are at the location of stochastic particles. The details of coupling are described in the next coupling section 3.4. The mixing operator M_α represents the conditional subfilter scalar dissipation. Mixing models involve various forms of direct exchanges between stochastic particles or interactions with filtered means. The most essential characteristics of mixing models are: (1) mean scalar quantities should not change as a result of mixing, (2) scalar variance should decay at the correct rate, and (3) scalar quantities should remain bounded, (4) linearity and independence of scalars and (4) localness of mixing. The mixing models used in the PDF methods are Curls [151] and modified Curls [66], interaction by exchange with the mean (IEM) [58], and the Euclidean minimum spanning tree (EMST) [67] model. However published FDF mostly use IEM [58]. Although IEM is very simple to use, but it does not ensure localness of mixing. In the intensive Lagrangian FDF simulations of gaseous fuel combustion these deficiencies are somewhat overcome due to the relatively smaller influence of the subfilter scale mixing on the macroscale features of the flow and the implicit localness resulting from the use of a well resolved grid.

In this study, mixing particles interact directly with each other, similar to Curl's model [151], but the pairs of particles are selected specifically so as to enforce localness in a reference space based on the filtered mixture fraction simulated by the LES according to Eqn. 3.33. The two parameters f_m and r_m are introduced representing characteristic distances between particles in mixture fraction and physical spaces respectively. The two separating distances can be approximated by considering isoscalar contours in a fractal

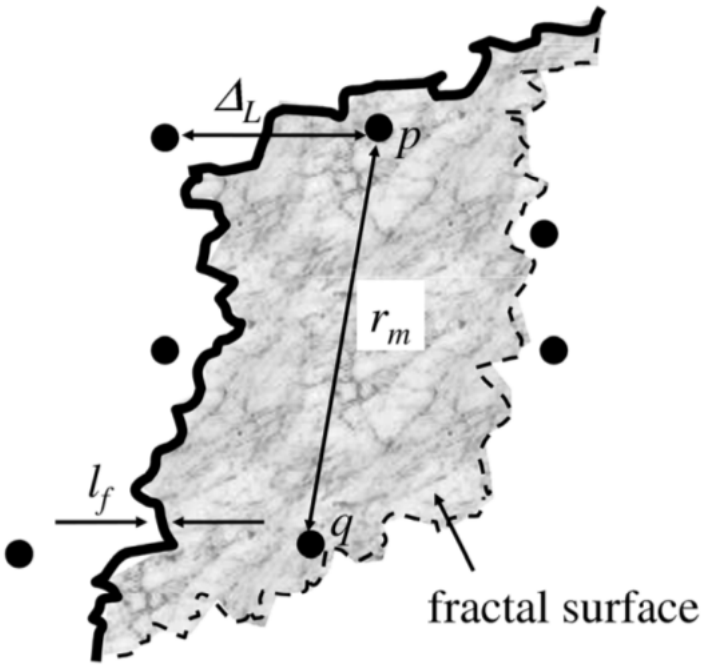

Figure 3.1: Schematic of mixing particle pair, q and q, located on a isoscalar surface with thickness l_f, the physical length scale r_m and the length scale to the nearest particle is Δ_L [2].

surface as shown in Figure 3.1. The fractal surface is considered here in a localization structure in a turbulent field, which is self-similar and self-affine that is a replica of whole structure made up of many pieces of such fractals as discussed elsewhere [152]. The thickness and fractal area of isoscalar sliver can be written as followings:

$$l_f \approx \frac{f_m}{\frac{d\tilde{f}}{dn}} \tag{3.57}$$

$$A_f = (\Delta_E / r_m)^{2-D_f} r_m^2 \tag{3.58}$$

where $\frac{d\tilde{f}}{dn}$ is the gradient normal to the isoscalar sliver, Δ_E is the filter width scale and D_f is the experimental observed fractal dimension. Therefore the volume of mixing particles can be written as $V_m \approx l_f A_f$. The volume of individual particle in the domain can be estimated by nominal distance between particles, Δ_L, as $V_L \approx \Delta_L^3$. By equating the two

volumes the relationship for r_m can be written as

$$r_m = C_m \left(\frac{d\tilde{f}}{dn} \frac{\Delta_L^3}{\Delta_E^{2-D_f}} \frac{1}{f_m} \right)^{1/D_f} \tag{3.59}$$

where C_m = 0.5, is a constant value determined by matching r_m to the actual mixing distance [2]. The scalar surface is modelled by a fractal dimension of D_f = 2.36. For each time step all particles are tested for mixing by minimizing the effective square distance. The k-d tree algorithm [153] is performed for the selection of particles to minimise the distance

$$\hat{d}_{p,q}^2 = \sum_{i=1}^{3} \left(\frac{d_{x_i}^{p,q}}{r_i} \right)^2 + \left(\frac{d^{p,q}}{f_m} \right)^2 \tag{3.60}$$

where r_i is the characteristic mixing distance in each spatial direction and set $r_i = r_m/\sqrt{3}$ for i = 1, 2, and 3; based on isotropic assumption of mixing distance between particles. Once particle pairs are selected based on the above description, pairs mix linearly and discretely over a finite time step Δt as following,

$$Y_{\alpha,G}^{sp,1}(t+\Delta t) = Y_{\alpha,G}^{sp,1}(t) + k\left(\bar{Y}_{\alpha,G}^{1,2}(t) - Y_{\alpha,G}^{sp,1}(t)\right)$$

$$Y_{\alpha,G}^{sp,2}(t+\Delta t) = Y_{\alpha,G}^{sp,2}(t) + k\left(\bar{Y}_{\alpha,G}^{1,2}(t) - Y_{\alpha,G}^{sp,2}(t)\right) \tag{3.61}$$

where $\bar{Y}_{\alpha,G}^{1,2}$ is the two-particle mean, which may be weighted if variable mass particles are used, and $k = 1 - exp(-\Delta t/\tau_G^{sp})$ is the extent of mixing controlled by a mixing time scale, τ_G^{sp}. Model is required for the mixing time scale, τ_G^{sp} which is done by scale similarity in the inertial range [2]:

$$\tau_G^{sp} = \frac{\widetilde{\xi'^2}_G^{sp}}{\widetilde{\xi'^2}_G^{eu}} \tau_G^{eu} \tag{3.62}$$

where

$$\widetilde{\xi'^2}_G^{sp} = C_f \beta |\widetilde{\xi}_G^{sp,1} - \widetilde{\xi}^{sp,2}|^2 \tag{3.63}$$

The coefficients are $C_f = 0.1$ and $\beta = 3$

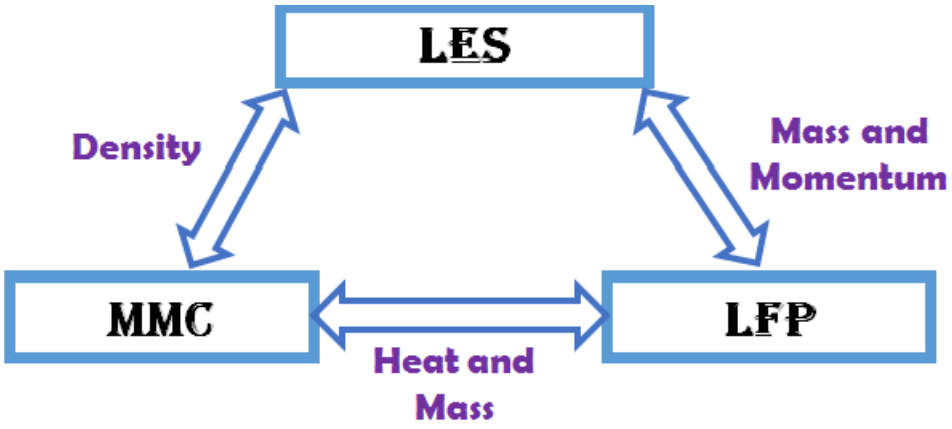

Figure 3.2: Schematic of coupling.

3.4 LES-MMC-LFP coupling

The models introduced in section 3.3 need to be coupled for updating source terms. The schematic of LES-MMC-LFP coupling is shown in Figure 3.2, where the three major code segments are related by two-way coupling. Two-way coupling is needed for using instantaneous values of species, mixture fraction and other parameters needed for the solution the LES-MMC-LFP packages.

The models are summarised in this section as following:

- Density coupling
- Mass and momentum coupling
- Heat and mass transfer coupling

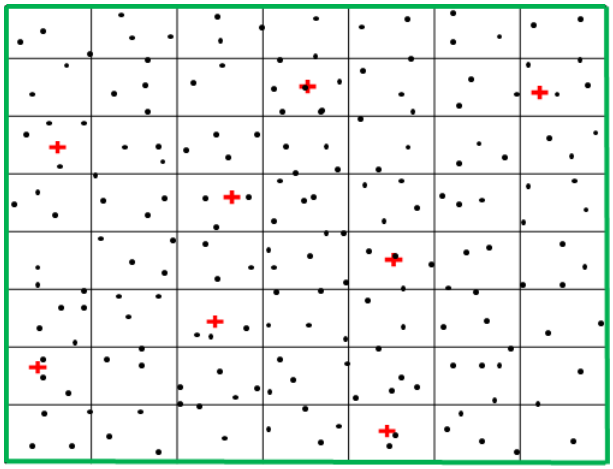

Figure 3.3: A supercell showing LES grids (black), stochastic particle (red plus sign) and fuel particle (black dots).

The details of each coupling are described in the following subsections.

3.4.1 Density coupling

Density coupling is done between simulated LES and MMC fields. It is a two-way coupling initiated from the LES field by passing filtered density to the MMC such that $\rho^{-sp} = \rho^{-eu}(x^{sp})$. The density of the centres of the LES grid cells is interpolated to calculate the density at the location of particles. In return, the density of each particle is known by the composition and the equation of state is sent back to LES via an estimate of its filtered value. Density feedback from MMC to LES is complicated due to stochastic error and the sparse nature of the notional particle scheme. For this study, rather than using direct backward coupling by density, the equivalent enthalpy method is used which was originally developed by Muradoglu *et al.* [154]. This adapted density feedback matches

the conditional means of the LES and MMC models. Although the unconditional filtered densities are not fully consistent between the two models, conditional averaging is in line with well accepted MMC and CMC concepts [2].

3.4.2 Mass and momentum coupling

Mass and momentum coupling is necessary due to gas production in the evaporation process in fuel particles. The coupling is done by updating LES model source terms from the Lagrangian fuel particle model applying the particle source in the cell (PSIC) approach [145] that has already been mathematically described in Eqns. 3.31, 3.32 and 3.34. As there can be more than one fuel particle in a single LES cell, the LES source terms are accumulated based on cell-wise for all particles and updated in Eulerian time step. The communication between LES and LFP is not necessarily only for mass and momentum coupling, rather LFP has a forward coupling with LES that has been described in the numerical implementation in Chapter 4.

3.4.3 Heat and mass transfer coupling

Heat and mass transfer coupling are done between MMC and LFP. In forward coupling, the surface mixture fraction, ξ_S^{fp} is calculated using MMC reacting scalar fields, from which the Lagrangian fuel particle heat and mass transfer rates, $\dot{m}_D^{fp}$ and $\dot{Q}_D^{fp}$, are obtained according to relations developed in Chapter 2. In backward coupling, LFP predictions of $\dot{m}_D^{fp}$ and $\dot{Q}_D^{fp}$ are used to evaluate conditional transfer rates Π^{sp} and used in Eqns. 3.54 to 3.56. The rates of heat and mass transfer to or from the fuel particle are dependent on the gas-phase composition and enthalpy fields as the Lagrangian fuel particle sees the

turbulent gas-phase particles that have been modelled by the MMC. The transfer rates specifically depend on the gradient of gas-phase composition in the diffusive boundary layer surrounding a fuel particle. However, this boundary layer is not resolved here. Moreover, the particles of the two models (MMC and LFP) are not co-located. The method adapted here is to select a stochastic MMC particle for each Lagrangian fuel particle so that $|\xi^{sp} - \xi^{fp}|$ is minimised, where ξ^{sp} and ξ^{fp} are reference mixture fractions at the stochastic particle and the droplet location, respectively. In this way, each stochastic particle may receive gas from any number of fuel particles and the fuel particle can the use the gas phase properties that is needed for LFP calculations. Conditional averaging is done to calculate these properties. Figure 3.3 shows the Eulerian grid (black mesh), Lagrangian fuel particles (black dots) and stochastic particles (red plus symbols). The outer big green box represents one supercell (for stochastic particles) which forms a boundary of particle ensembles used for conditional averaging. To address these complexities, a coupling based on conditional averaging is implemented.

3.4.3.1 Forward coupling (MMC to LFP)

The Spalding transfer numbers that have been derived in Chapter 2 show that the Spalding heat transfer number, B_H, depends on the difference between the standardised enthalpy between the 'G' and 'S' states of the fuel particles, while the Spalding mass transfer number, B_M, is related to the mixture fraction difference between the same two states. The purpose of forward coupling is to calculate those four quantities, $\hat{h}_G^{fp}$, $\hat{h}_S^{fp}$, ξ_G^f and ξ_S^{fp}, using information at the fuel and stochastic particle locations.

The gas composition at the location of a fuel particle is well approximated by

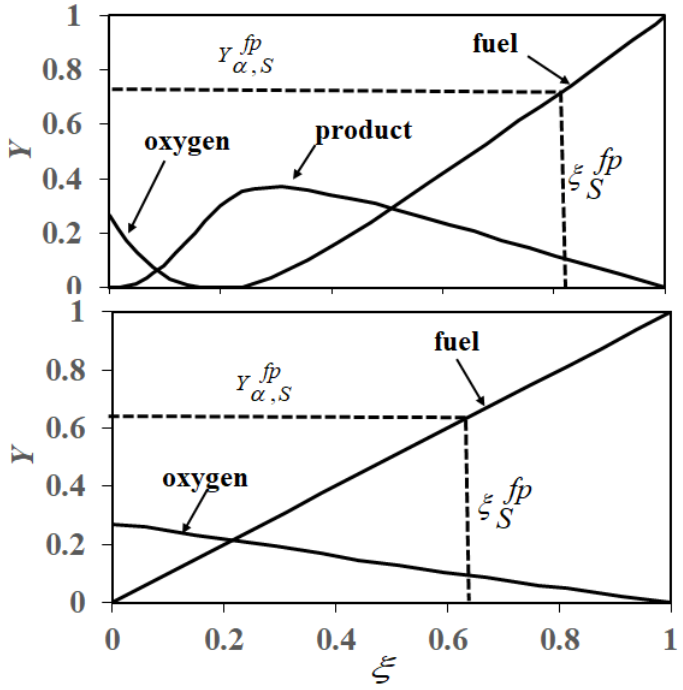

Figure 3.4: Species mass fraction (Y) and mixture fraction (ξ) is shown for both burning (top) and non-burning (bottom) cases.

conditional means that are obtained from a stochastic particle ensemble in the vicinity of that fuel particle as the spatial gradient of conditionally averaged compositions are usually smaller than the gradients of unconditional averages. For the surface state mixture fraction as explained above, the Clausius Clapeyron evaporation model is applied. There are two possibilities; (1) droplets are burning with an envelope flame and (2) there is no envelope flame at all or evaporating only. The burning droplet is modelled by a lightly strained laminar flamelet as shown (top) in Figure 3.4. The surface mixture fraction, ξ_S^{fp}, is obtained from the abscissa of the intersection between a horizontal line with an ordinate of $Y_{\alpha,S}^{fp}$ and fuel mass fraction line as shown in Figure 3.4. As stated above, an envelope flame can form around a droplet or droplet clusters and the flames can be extinguished by slip. In the present study,the sensitivity of spray flames is studied for the two limiting cases of (i) no envelope flames at all, and (ii) envelope flames form around an individual

droplets when $\xi_S > \xi_{St} > \xi_G$, where ξ_{St} is the stoichiometric mixture fraction.

Once the values of $\xi_G^{fp}, \xi_S^{fp}, Y_{\alpha,G}^{fp}$ and $Y_{\alpha,S}^{fp}$ are found then the enthalpies, $\hat{h}_G^{fp}$, $\hat{h}_S^{fp}$ can be calculated from the thermodynamic data.

3.4.3.2 Backward coupling (LFP to MMC)

The heat and mass transfer rate of each fuel particle is now available. To find an expression for the conditional transfer rate Π^{sp}, it is assumed that gas released from the fuel particle occupies the LES filtered cell volume at the location of that fuel particle, V^{eu}, then $\Pi^{fp} = \dot{m}_G^{fp}/\rho_G V^{eu}$. This conditional transfer rate is supposed to maintain mass consistency between LFP and MMC. Once the stochastic particle is selected for pairing with a fuel particle with the same method adapted for forward coupling, the source terms are updated for each time step from LFP to MMC.

Chapter 4

Numerical implementation

The numerical simulation of a liquid spray is a difficult task due to the existence of multiple phases and their simulation in the context of droplet dynamics, turbulent flow, heat and mass transfer between liquid and carrier phase and chemical reaction in the carrier phase. The governing equations for liquid spray, multiphase flow and combustion are derived in Chapter 2 and Chapter 3. The simulation is performed and the results are compared with the relevant target flames to justify the validity of the modelling approaches proposed in this thesis. This chapter discusses the selection of target flames, model set up, boundary conditions and numerical schemes that have been applied for the simulation of the selected target cases.

4.1 Target flames

There are strong research interests among CFD communities to expand the current modelling capabilities of dilute spray jets and flames. In particular, there is interest in droplet dynamics and the interaction of droplets with flow, heat and mass transfer between

droplets and carrier phase, autoignition characteristics, and combustion of different droplet modes. The international workshop series on Turbulent Combustion of Sprays (TCS) was established in 2009 in a bid for collaboration worldwide between numerical and experimental groups. A series of experiments performed by Masri and Gounder [155, 1] were chosen as reference test cases for validation of numerical approaches. The target cases selected for the contribution in the last TCS-2015 workshops were KS6 as non-reacting kerosene, SP6 as evaporating but non-reacting acetone and EtF6 and EtF7 as reacting ethanol. The contributors for the reacting acetone (AcF1- AcF8 series of Sydney University) cases were not available up to TCS5 workshop. For this study, the target cases are selected keeping in mind TCS6-2017 workshop as following: KS6 and KS7 cases as non-reacting kerosene and SP6 and SP4 as evaporating but non-reacting acetone and AcF1 and AcF2 as reacting acetone. The details of the case specific data are given in the corresponding chapter.

4.2 Burner specification

The schematic of the piloted burner and co-flow assembly is shown in Figure 4.1. There are three parts in the burner; a burner base, a contraction, and a pilot flame holder. The contraction is made of aluminium and has a contraction ratio of 10:1. The central jet is 10.5 mm, the diameter of the pilot annulus is 25.0 mm and the co-flow diameter is 104 mm. The lip thickness of the annulus is 0.2 mm. The pilot flame holder is fixed 7.0 mm upstream of the nozzle exit which holds 72 holes concentrically aligned at 7 mm, 9 mm and 11 mm radius from the centre and each row contains 24 holes with diameters 0.9 mm, 1 mm and 1.1 mm respectively. The cross section of the tunnel exit is 290

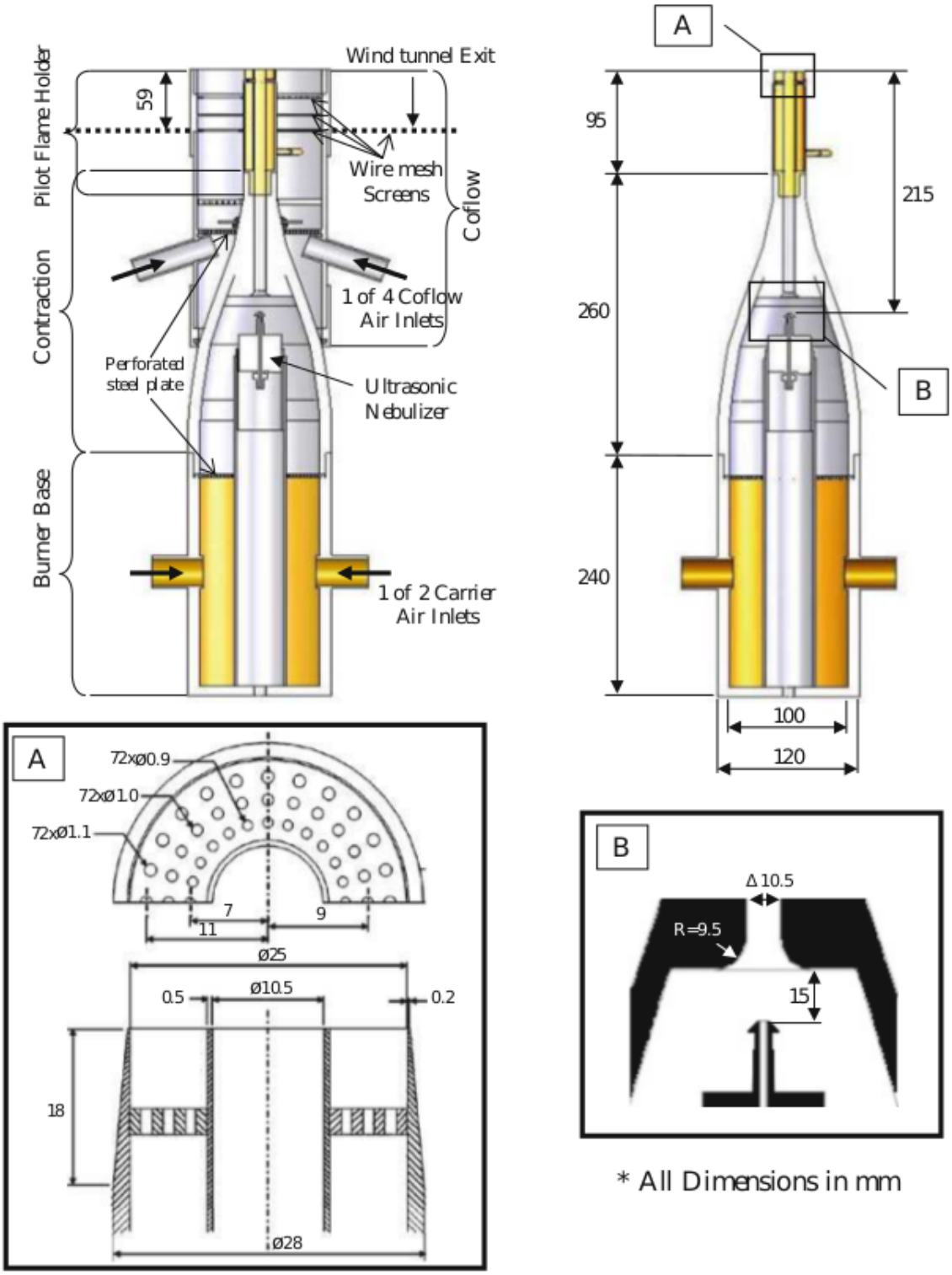

Figure 4.1: Schematics view of Burner and co-flow assembly [1], reprinted with publisher's permission.

mm x 290 mm. The spray is generated by an ultrasonic nebulizer. The droplet size distribution produced by the nebulizer as reported by Sono-Tek (model number 8700-48) is approximately lognormal with the mean diameter $40\mu m$ when using liquid water. A typical experimental measurement of droplet distribution is shown in Figure 4.2, where the mean particle diameter is found approximately $38.8\mu m$ for SP4 evaporating acetone case [1]. The nebulizer head is located 215 mm upstream of the jet exit plane so that a certain portion of liquid fuel is evaporated for acetone cases before the exit plane.

The following measurements were performed by Gounder and Masri [155]:

(i) Mean and RMS droplet velocity by Laser Doppler Velocimetry (LDV).

(ii) Droplet fluxes and size distribution by Phase Doppler Anemometry (PDA).

(iii) Planar imaging for selected scalars by Laser Induced Fluorescence (LIF), namely OH, acetone or formaldehyde.

(iv) Mean temperature by R-Type thermocouple.

The measurement uncertainties that are associated with these techniques are of the order of 10 % for temperature, 6% for mean velocity and 15% for RMS velocity [1]. The measured liquid and vapour mass flow rate data are used for the boundary conditions of different target cases of liquid phase simulations. For the acetone cases with pre-evaporation, the measurement data of vapour fuel flow rate and carrier air flow rate are used to calculate the jet gas phase mixture fraction at the exit plane as

$$\xi_{jet} = \frac{\dot{m}_{vap}}{\dot{m}_{vap} + \dot{m}_{air}} \tag{4.1}$$

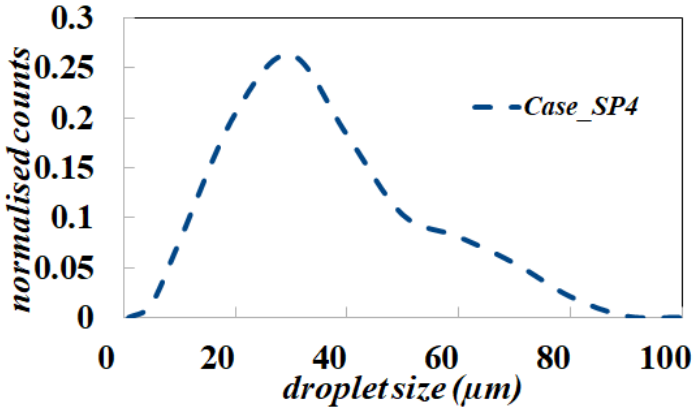

Figure 4.2: Droplet size distribution of SP4 case [1].

where $\dot{m}_{vap}$ is the fuel vapour flow rate and $\dot{m}_{air}$ is the measured carrier air flow rate at the exit plane.

4.3 General set up of cases

Numerical schemes, boundary conditions and model set up depend on which case is being simulated. Unless anything is specifically mentioned, the following subsections are the general discussion of numerical implementation and model set up. The case specific boundary conditions are discussed in the respective chapter (Chapter 5, Chapter 6, Chapter 7), where the simulation results are presented.

4.3.1 Hybrid numerical method

In this study, a hybrid Eulerian/Lagrangian method is used for sparse Lagrangian MMC-LES combustion modelling of liquid spray. The Eulerian mesh is used for the simulation of LES velocity, pressure and reference mixture fraction. The Lagrangian stochastic particle model is implemented in FDF formulation for the simulation of gas phase mixing, chemical reaction and species composition fields. The second Lagrangian

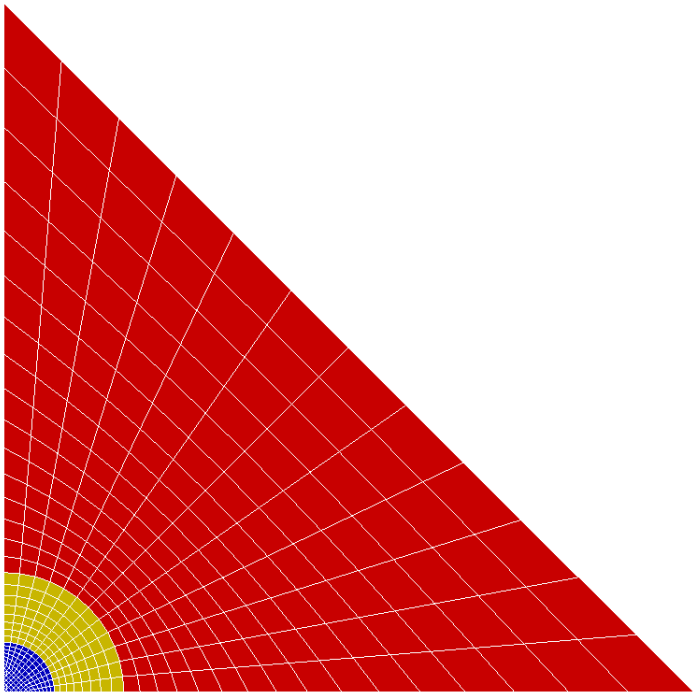

Figure 4.3: The schematic view of one quarter mesh in inlet patches; the colour schemes: blue, yellow and red correspond to main jet, pilot and co-flow patches, respectively.

particle model is used for the modelling of the liquid phase. The liquid phase droplets are tracked as parcels with each parcel representing many identical droplets [130]. The coupling of the two Lagrangian particles and LES has been described in subsection 3.4

4.3.2 Geometry and mesh

The numerical grid is generated in the OpenFOAM computational scheme called blockmesh. For the LES grid, the numerical domain is taken as a rectangular box with a dimension of $14D$x$14D$x$35D$, where, D is the diameter of the main jet. The schematic of one-quarter of inlet patches is presented in Figure 4.3, which shows main jet, pilot, and co-flow patches with three different colours as follows: blue, yellow and red corresponding to the main jet, pilot and co-flow respectively. The kerosene and evaporating acetone cases are simulated by basic model grid resolution of total 453440

LES cells hexagonal mesh consisting of 1417 cells in xy rectangular box and 320 axial cells in the z direction. The supermesh grid resolution consists of 64 axial cells in the z direction and 192 cells in the xy rectangular box with total 12288 cells.

Properties	Course	Medium	Fine
Axial resolution	0.79	0.66	0.44
Radial resolution	0.42	0.22	0.16
Axial Total Cells	320	320	384
Cells in Jet	481	1273	2625
Axial expansion	2	2	4
Total Cells	453440	1331520	2620800

Table 4.1: Mesh sensitivity study implemented in evaporating SP4 case.

The LES reference mixture fraction symbol ξ is replaced by f for presentation of simulation results. The LES mesh sensitivity is studied by simulating three cases: coarse, medium and fine mesh with different grid resolutions. The details of grid resolution of the three cases are shown in Table 4.1. Here, the grid sensitivity is studied in the evaporating SP4 acetone case as the reacting cases are the most complex simulations involving LES and two Lagrangian particle models (MMC and LFP), where the results may be affected by the modelling parameters. The simulation results of the gas phase velocity and the reference mixture fraction, f are compared to study the grid sensitivity. The axial centreline velocity of the three cases and experimental velocity of $0 - 10\mu m$ droplets are shown in the Figure 4.5 (left side), where all velocity profiles are showing consistent results. The centreline reference mixture fractions of the three cases are also shown in the above same figure (right), where all three cases are nicely following a similar trend

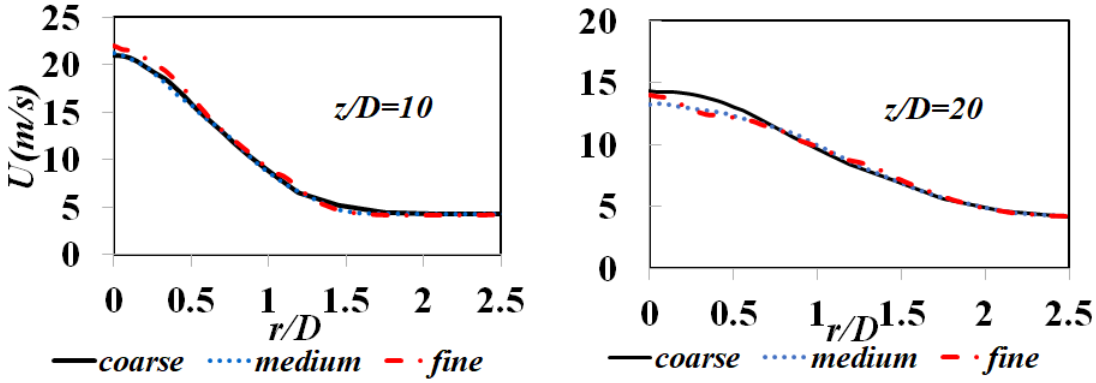

Figure 4.4: Radial profiles of axial velocity of three cases in $z/D = 10$ (left) and $z/D = 20$ (right) locations; in the figure U stands for mean velocity.

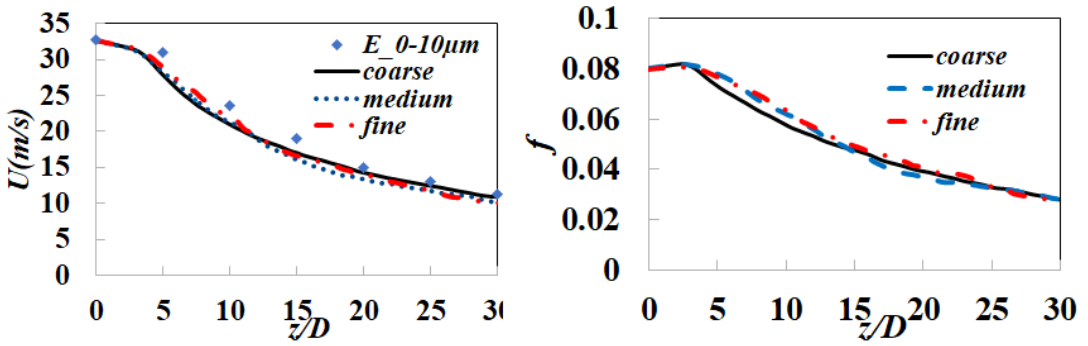

Figure 4.5: Axial profiles of centreline velocity of three cases and experimental results of $0 - 10\mu m$ droplet velocity (left) and the reference mixture fractions of three cases (right).

except a little under prediction of the coarse case result in the $z/D = 5, 10$ locations. The radial profiles of velocity in the $z/D = 10, 20$ locations are shown in Figure 4.4, where the velocity of the coarse case is over-predicting a little bit in the $z/D = 20$ location. The radial profile of the reference mixture fraction is shown in the same radial locations in Figure 4.6, where the results are showing a similar trend to the radial velocity cases. Overall the results of the three cases show good agreement with each other. The medium grid resolution is chosen finally for the investigation of reacting cases considering the cost and accuracy of simulation.

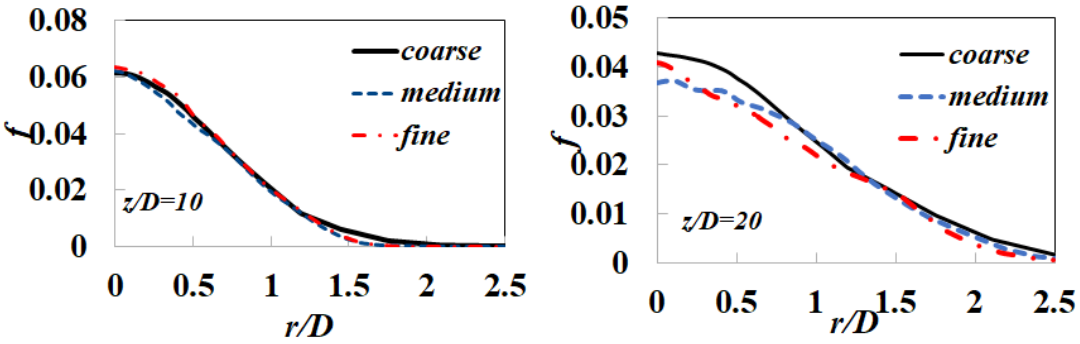

Figure 4.6: Radial profile of reference mixture fractions in z/D=10,20 locations.

4.3.3 Boundary conditions

The initial boundary conditions are applied for the main jet, pilot, co-flow, side and outlet patches. A digital filter based generation of inflow data for the velocity boundary condition is introduced following the method developed by Klein *et al.* [156] by using mean and variance of experimental data. The initial velocity boundary condition is as followings: a time varying mapped fixed value for the main jet, a fixed value for the pilot and co-flow and pressure inlet outlet velocity condition for the side and outlet patch. The pressure boundary condition at flow inlets and outlets are zero gradient, while at the side boundaries a fixed value pressure is specified. The total pressure boundary condition is applied to the side and outlet patch, whereas zero gradient pressure is applied for main jet, pilot, and co-flow. Mixture fraction, species and temperature boundary conditions are applied according to experimental data for the relevant cases.

4.3.4 Chemical mechanism

For the reacting acetones cases, there are two acetone mechanisms; the mechanisms of Pichon *et al.* [157] and Chong and Hochgreb [158] have been used in past studies [136]. Chong and Hochgreb [158] extended the GRI 3.0 methane mechanism by adding

an additional sub-mechanism for acetone, which involves 38 species and 224 chemical reactions. Pichon *et al.* [157] developed another acetone mechanism consisting of 81 species and 419 chemical reactions from the dimethyl ether mechanism. Ukai *et al.* applied the Pichon mechanism for the study tabulated flame chemistry approach, where Chong's mechanism caused some instabilities [136]. However, Ukai *et al.* [136] preferred the Chong mechanism as there was no significant difference between the two mechanisms in both conventional CMC and two conditional moment approaches [136]. For this study, the Chong mechanism is applied as the number of species and chemical reactions is less compared to the Pichon mechanism. For the chemistry solver stiffly-accurate embedded Rosenbrock ODE of the order of (2)3 [159] is used for the stiff acetone chemical reactions.

4.4 Discretisation and solvers

The numerical simulation is performed in mmcFoam [160], a branch of the OpenFoam CFD code developed by Sydney University. This is a C++ object oriented programming code structured in nested templates (i.e. generic code instantiated at runtime). Each level of the nested templates represents the specific physics. A multiphase application solver is created for the purpose of simulating dilute spray in turbulent flow consisting of LES, MMC and LFP code. There are also some other utility packages for the Eulerian statistics, the statistical random distribution and the post processing. The simulation starts with the solution of the LES governing equations and within the LES simulation loop, C++ objects are created for the two Lagrangian particle models. These two C++ objects are used in runtime in every LES time step for their respective simulations to perform. The coupling of sub-models is done as described in section 3.4 during this simulation loop.

The numerical schemes used for the major code segments are described below in the following subsections.

4.4.1 LES schemes

The LES simulation is performed up to resolved filtered length scales, and the subgrid scales are modelled for viscous stress tensor by the eddy-viscosity model assuming kinetic energy analogous to molecular diffusion. The unclosed term in the turbulent eddy-viscosity model is modelled by the Smagoronsky-Lilly model [143]. The chemical reactions and gas production occur in the unresolved scales, which are modelled by the MMC and LFP models respectively. For the LES, finite volume simulation is performed in low Mach compressible pimple solver for the solution of flow (pressure, velocity, density), species and reference mixture fraction transport equations. The numerical simulation mostly uses second order schemes. The second order finite volume schemes are as following: a backward scheme for the time derivative, a Gauss linear for gradient and Gauss limited linear (bounded) for the divergence scheme. The interpolation and surface normal gradients are calculated based on the first order linear and second order corrected schemes respectively. The source terms are updated in runtime from the respective Lagrangian particle solution.

4.4.2 MMC schemes

The stochastic differential equations derived in subsection 3.3.2 follow the concept of FDF formulation. These equations (Eqn. 3.53 - Eqn. 3.56) are solved by the stochastic Lagrangian particle approach with the aid of Fokker-Plank formulations for drift and

diffusion terms, [161, 162] mixing model and chemical reactants. MMC applied Curl's [151] mixing model, but the selection of particle is done by specifically enforcing localness. The mixing parameters f_m and r_m are selected based on the details given by Cleary and Klimenko [2]. Two-way density coupling is done between MMC and LES using the equivalent enthalpy method [154, 61]. LES simulation provides velocity, turbulent diffusivity, and reference mixture fraction to the MMC field which in turn gives density feedback to the LES. The density is calculated algebraically from the solution of a filtered enthalpy like property, which is obtained from a Eulerian transport equation.

MMC has four templates, namely, ItoPopeParticle, MixingPopeParticle, ReactingPopeparticle, and ThermoPopeparticle. The submodels used in MMC simulation are: inflow boundary, composition, radiation, mixing, and reaction model for the particle injection, species composition, radiation effect, gas phase mixing and finite rate chemistry respectively. MMC retains all the generality of OpenFOAM allowing for structured and unstructured grids, numerous discretization and integration schemes, and the full range of thermodynamic and kinetic flexibility.

4.4.3 LFP schemes

A new LFP code is developed for the liquid phase simulation and for coupling with LES and MMC. The governing equations for the LFP simulation are provided in Chapter 2. The LFP code is developed retaining the same generality of MMC. There are two templates in LFP: KinematicParcel and ThermoParcel including submodels for evaporation, fuel parcel injection and post processing. The fuel droplets are defined [130] and tracked as a parcel. The solution of each parcel is performed in Lagrangian time

step and the source terms are updated in each Eulerian time step for the LES and in each Lagrangian time step for MMC.

The LFP code has easy access to all liquid phase initial and constant properties from the case dictionary, which is well designed OpenFOAM coding style. LFP also uses instantaneous values from the LES and MMC particle models. The cell centre values are interpolated in the face for scalar and vector value from the respective volscalar or volvector parameters. The interpolation schemes are used for the LES density, velocity, viscosity, reference mixture fraction, temperature, specific heat, the gradient of reference mixture fraction and pressure. LFP also uses gas phase mixture fraction, species, and temperature for solving the LFP governing equations using stochastic particle values representing the gas phase in the reference mixture fraction space.

The first order Euler integration scheme is used for the parcel velocity, temperature, and volatile mass calculation by solving ODE equations as derived in Chapter 2. The second order Crank-Nicolson method is applied for the final parcel temperature and volatile mass calculation as the Crank-Nicolson is unconditionally stable [163] for the cases of heat and mass diffusion equations. The Clausius Clapeyron relation is solved for the surface state mixture fraction using equivalent flamelet curves of species. The film state mixture fraction is also needed for solving the LFP modelling equations, which is assumed equivalent to one-third of gas plus two thirds of the surface state mixture fraction. The film state viscosity and density is obtained from the first order Sutherland's relation using surface species and parcel temperature.

Chapter 5

Simulations of kerosene dispersion

5.1 Introduction

The simulation of liquid spray involves the presence of both carrier and dispersed phases and their couplings. In this thesis, there are three complicated spray simulations, namely (1) dispersion, (2) evaporation and (3) combustion and each is investigated in succession. This chapter is devoted to dispersion. The governing equations for liquid spray dispersion were derived in subsection 2.2.1 of Chapter 2. The theory has been implemented for non-reacting KS6 and KS7 kerosene cases [1] of Sydney University.

5.2 Case specific set up and boundary conditions

For simulating the kerosene dispersion cases, the liquid fuel droplets are modelled by the Lagrangian particle approach, the reasons for this selection having already explained in subsection 2.1.6. The Lagrangian fuel droplets are simulated as parcels (a collection of identical droplets) with the same properties such as diameter, mass, and velocity. The

Non-reacting kerosene cases	**KS6**	**KS7**
Bulk jet Velocity, U_{jet} (m/s)	36	60
Carrier	Air	Air
Carrier mass flow rate (g/min)	225	376
Liquid fuel injection rate (g/min)	45	75
Measured liquid flow rate at exit (g/min)	37.7	66.1
Co-flow bulk velocity (m/s) of air	4.5	4.5
Bulk velocity in pilot stream (m/s) of air	4.5	4.5
Reynolds number range	19000 -30000	19000 - 30000
Stokes number range at exit plane	0.11 - 2.06	0.11 – 2.06

Table 5.1: Boundary conditions for kerosene spray cases

parcels are tracked in the Lagrangian time step, which is usually a smaller time step depending on the instantaneous velocity of the parcels to cross the cell faces with respect to each Eulerian time step. There can be multiple Lagrangian time steps for each Eulerian time step, so as to ensure that parcels are not left out in the face of the corresponding cell. The LES momentum source term is updated in each Eulerian time step by accumulating a cell based total mass of all parcels multiplied by their respective velocity adapting the 'particle source in cell' (PSIC) method.

The initial boundary conditions of KS6 and KS7 cases are shown in Table 5.1. The co-flow velocity is 4.5 m/s for both cases, while the bulk velocities of KS6 and KS7 are 36 m/s and 60 m/s, respectively. The liquid fuel droplets are injected in the domain randomly according to measured experimental distribution of droplets (as explained in subsection 4.2) and the mass flow rates (see in Table 5.1). The parcels evolve in the domain with an

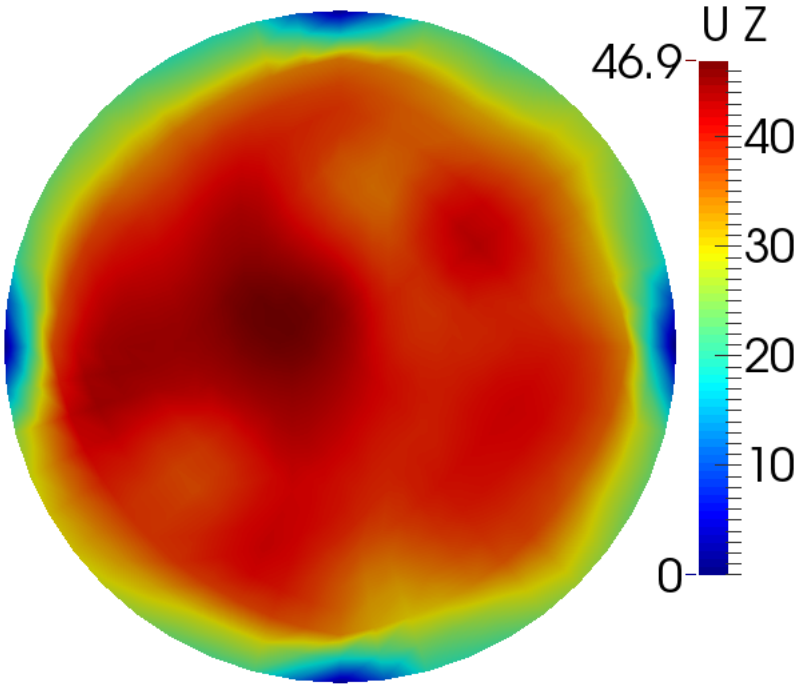

Figure 5.1: Instantaneous initial axial velocity profile of kerosene case KS6 with turbulence.

initial velocity, diameter and parcel id, maintaining the experimental mass flow rate. The initial velocity profile is shown in Figure 5.1, which shows a roughly parabolic profile with turbulence based on the method developed by Klein *et al.* [156] and experimental data [1].

5.3 Results and analysis

The characteristics of liquid spray and droplet dynamics are reviewed in section 2.1 of Chapter 2. It is found that both dispersed and gas phases can influence on each other in the turbulent two-phase flow. The simulation is aimed to explore the key features of liquid spray dispersion, the influence of dispersed and carrier phase each other and the validation of kerosene dispersion with experimental data [1]. The simulation results of

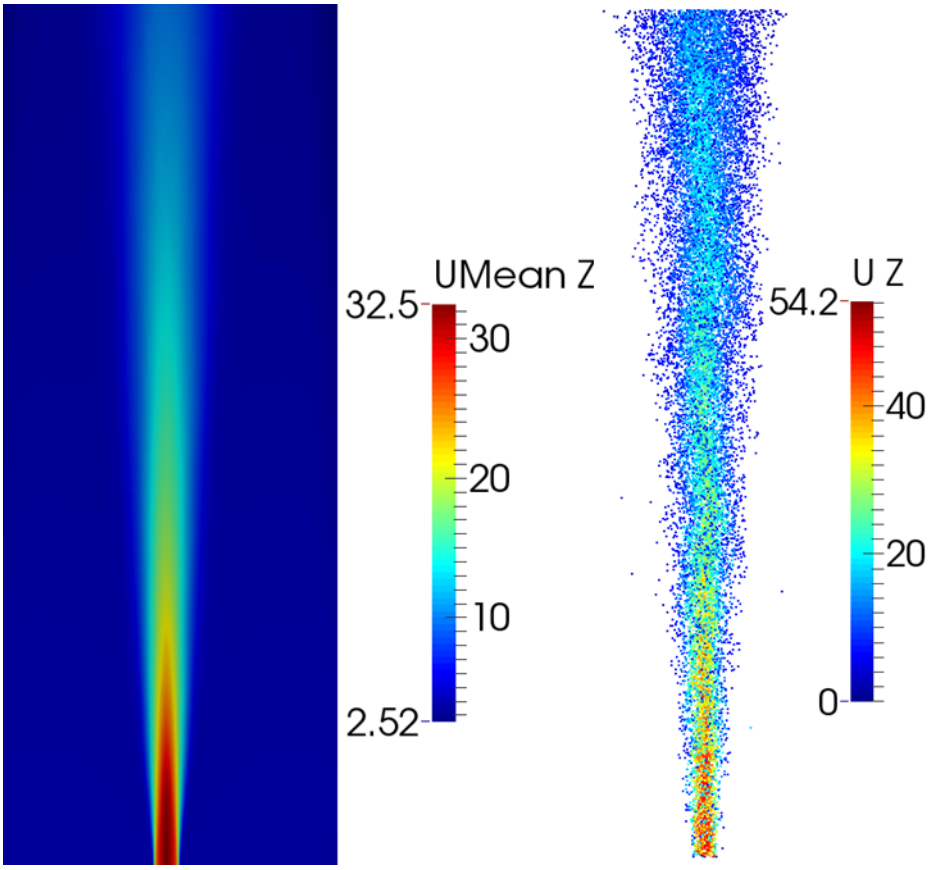

Figure 5.2: Axial profile of carrier velocity (UmeanZ) and instantaneous droplet velocity (UZ) in KS6 case.

kerosene cases, KS6 and KS7, are presented in this section highlighting the key features of droplet dynamics. It is expected that different droplet sizes would influence the behaviour of liquid spray. According to governing equations for liquid phase dispersion derived in Chapter 3, the smaller droplets decelerate quickly with the gas phase due to lower particle response time (see in Eqn. 2.5), whereas the larger droplets conserve their velocity due to higher response time and experience higher slip velocity. It is also expected that the larger droplets would show higher velocity due to the fact that the Stokes number for larger droplets is greater than unity confirming the higher slip velocity.

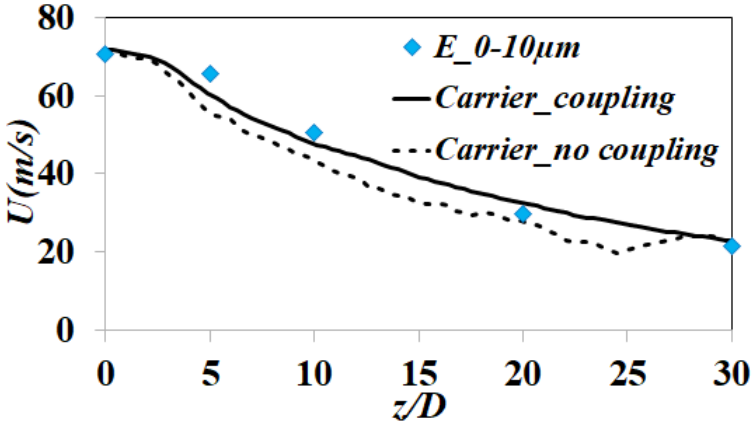

Figure 5.3: Effect of carrier phase momentum source term on axial centreline velocity and early jet break up in KS7 case. The letter 'E' stands for experimental measurement [1].

5.3.1 Interactions of two phases

The contour plot of the mean profile of carrier velocity for the KS6 case is shown in the left side of Figure 5.2, which shows potential core jet break up and successive decay of velocity from upstream to downstream. The fuel droplet dispersion is shown in the right side of Figure 5.2, which shows droplet velocity in both axial and radial directions after the jet break-up. The dispersed phase can influence the carrier phase velocity due to the momentum effect of droplets. The simulation is performed with and without momentum coupling for testing the sensitivity of the carrier phase velocity with respect to droplet momentum as shown in Figure 5.3.

The axial centreline velocity of the carrier phase is showing under prediction without momentum coupling (see in Figure 5.3) and also the early jet break up in $z/D = 10$ axial position causes the under prediction up to $z/D = 25$ and after that it is merging toward the experimental value in the downstream with little effect of the momentum source term probably due to lower velocity of droplets.

5.3.2 Mean velocity profile

The simulation result of kerosene dispersion is validated against the experimental data for both mean and RMS velocity profiles with varying droplet size as the droplet size plays an important role in the dispersion. The mean profiles of axial centreline velocity of the experimental and simulated results of both carrier and droplets are shown in Figure 5.4, which are in good agreement with each other for the droplet size range of $0 - 10\mu m$. The simulation accurately captures the jet breakup point at about $z/D = 5$ and the subsequent decay in full domain. There is some overprediction of the mean velocity at about mid-way along the domain for the KS6 case, whereas the KS7 case is showing good agreement. Moreover, 6 % uncertainties in experimental measurement [1] were recorded for the mean velocity.

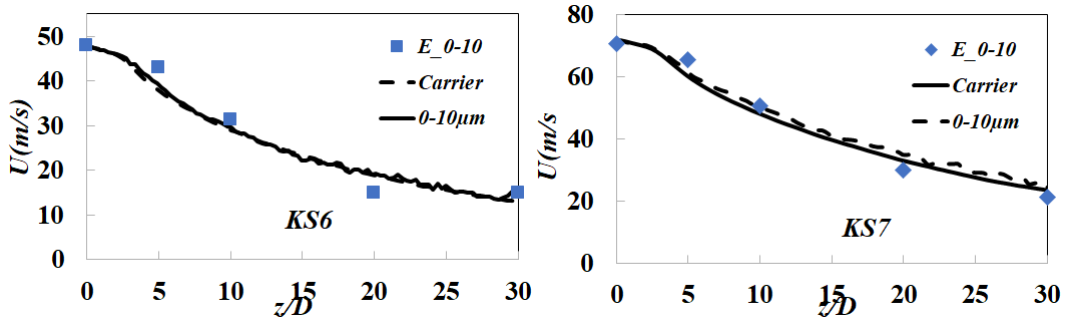

Figure 5.4: Axial centreline velocity profiles of KS6 and KS7 cases.

The radial profiles of axial mean velocities are also compared in Figs. 5.5 and 5.6 with the experimental data at $z/D = 10, 20$ and 30 locations for the parcels size range of $10 - 20\mu m$, $20 - 30\mu m$, $30 - 40\mu m$ and $40 - 50\mu m$. All the radial profiles are showing good agreement with their corresponding experimental data except some discrepancies are found in the $z/D = 20$ location for the KS6 case, which is also similar to the discrepancy in the axial centreline mean velocity. It is also found that the larger droplets

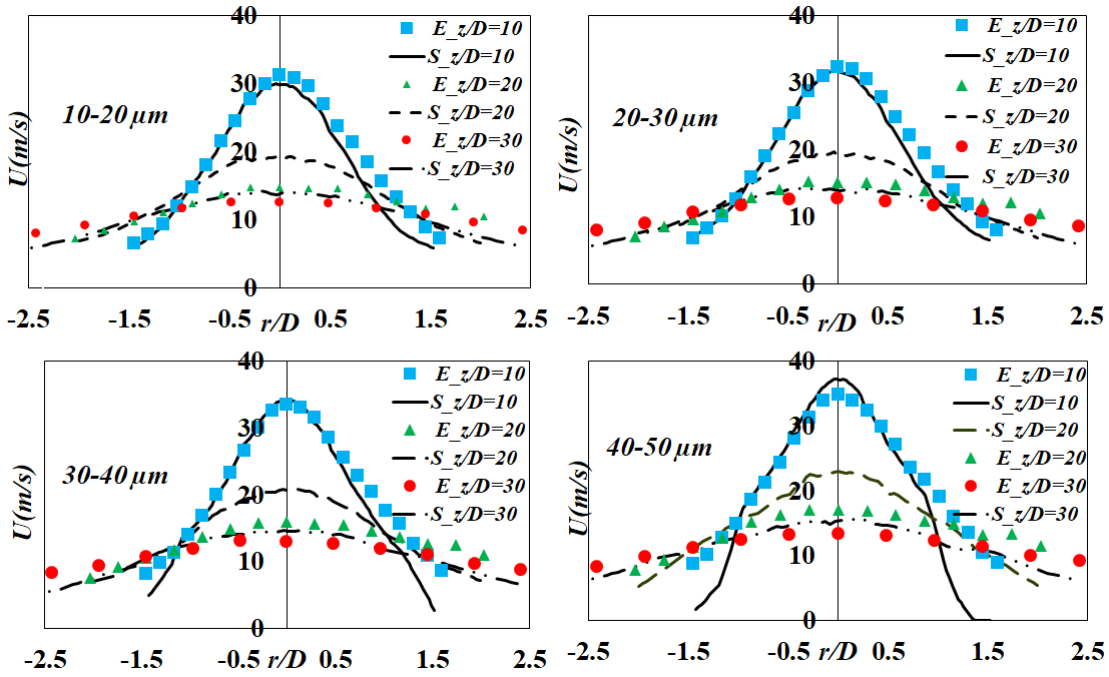

Figure 5.5: Radial profiles of axial velocity for different droplet size of KS6 case, the letter 'S' stands for Simulation result.

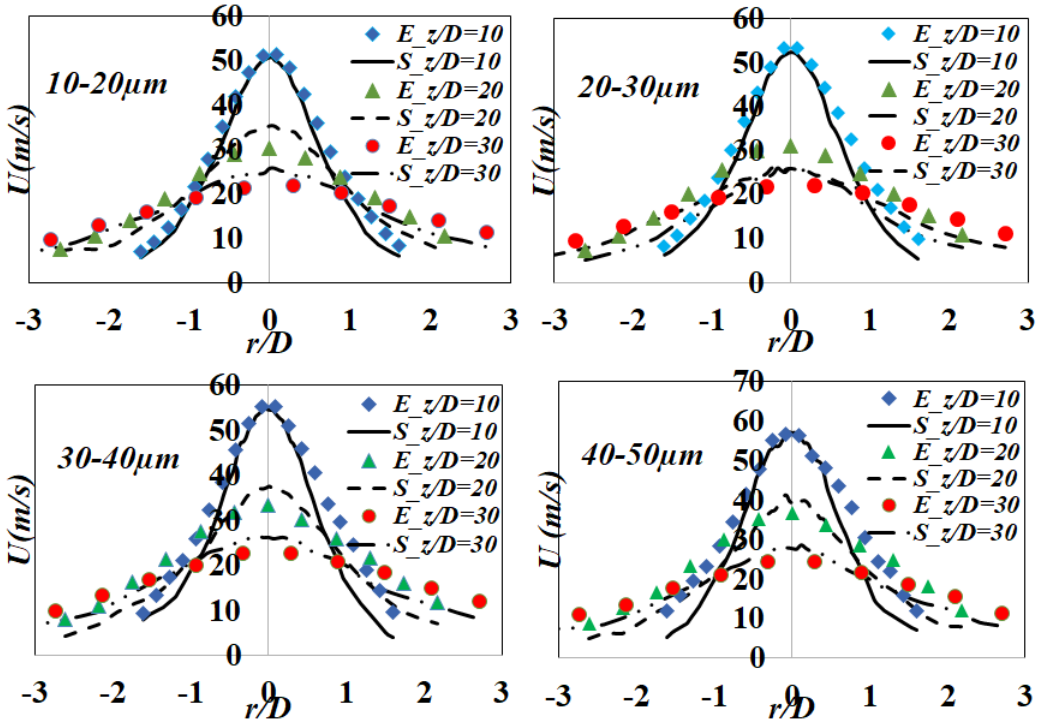

Figure 5.6: Radial profiles of axial velocity for different droplet size of *KS7* case.

$(40 - 50\mu m)$ have experienced higher peak velocity at $z/D = 0$ as 37.24 m/s and 57.23 m/s for KS6 and KS7 respectively against the smaller droplets $(10 - 20\mu m)$ velocity as 31.58 m/s and 50.79 m/s. It is expected as the Stokes number of larger droplets is greater than unity and the slip velocities are high. Overall, the droplet velocity of these two cases (KS6 and KS7) are showing good agreement with the experimental data.

5.3.3 RMS velocity profile

The simulation results of RMS velocity profiles of two kerosene cases are compared with the experimental data for the droplet size of $10 - 20\mu m$. The centreline RMS of axial velocities of both cases are showing good agreement in the $z/D = 0, 5, 20$ and 30 locations but some significant discrepancy is found in the $z/D = 10$ location, which is immediately after the jet break-up point. The radial profiles of RMS velocity are

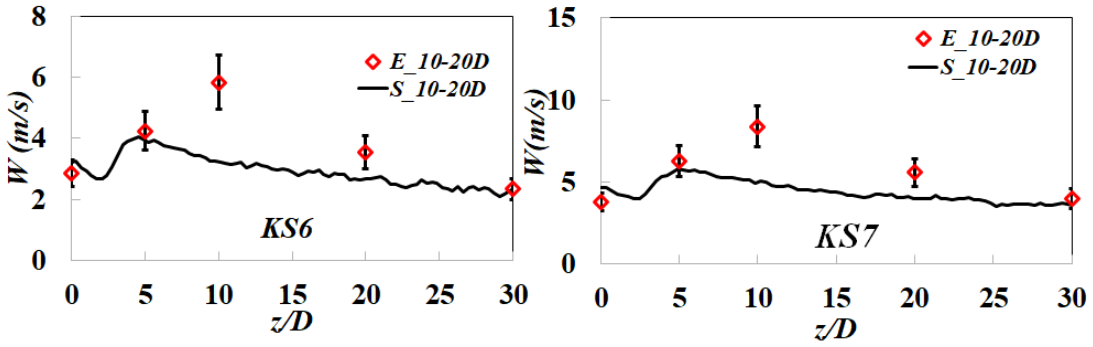

Figure 5.7: Axial profile of RMS velocity *10-20* μm droplets, in the figure 'W' stands for RMS velocity. The experimental uncertainly is shown by error bars.

also shown in Figure 5.8 for the KS6 and KS7 cases for the same droplet size range as the axial RMS profile. It seems that RMS velocities for both cases are under predicting in $z/D = 10$ location, whereas better agreement is found at $z/D = 20$ and 30 locations with experimental data. The discrepancy of RMS velocity was recorded 10-15 % by Gounder *et al.* [1]. The error bars are showing close agreement in all axial and radial positions

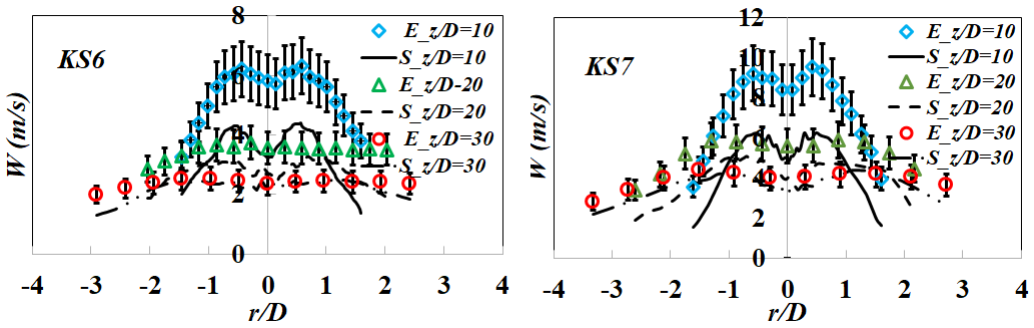

Figure 5.8: Radial profile of RMS velocity of *10-20* μm droplets, the experimental uncertainly is shown by error bars

except at $z/D = 10$. Overall, the trend of RMS velocity profiles is reasonable except for the discrepancy after the jet break-up point.

5.4 Discussion and conclusions

The kerosene cases are simulated with introduction of Lagrangian particle based particle dispersion part of LFP model. The particles are tracked as parcels in Eulerian grid cells to reduce computational cost. The source term is added in momentum transport equation for updating liquid phase interaction to the gas phase following particle source in cell approach from LFP. For testing the accuracy of LFP-LES coupling for dispersion source term, the simulation is performed with and without source term in KS7 case. The axial centreline velocity has improved and the simulation captures the actual jet break-up while the early jet break-up occurs without momentum coupling.

The simulation results of mean and RMS velocity profiles are presented for different droplet classes. The axial and radial profiles of mean velocity are showing good agreement with the experimental measurement [1]. There is some discrepancy in the RMS velocity profiles, but the results are qualitatively similar to the experimental data. It is found that the smaller droplets are following the carrier phase velocity on account

of their low Stokes number. It is found that the smaller droplets are following the carrier phase velocity on account of their low Stokes number. Although the larger droplets are decelerating more on account of their higher stokes number the dispersion of such droplets is dominated by inertia effect and cross stream movement leading to higher dispersion. The droplet size and their corresponding velocity profiles are consistent with the literature review that has been discussed in Chapter 2. The simulation results nicely capture the jet break-up, the effect of turbulence on dispersion, the influence of carrier phase velocity due to the momentum source term and the effect of droplet size on velocity. This simulation, which is the starting point before implementing the evaporating and reacting cases, shows encouraging results.

Chapter 6

Simulations of evaporating acetone

6.1 Introduction

The behaviour of evaporating liquid spray has been discussed in Chapters 1 and 2. From the modelling point of view, the importance and the principle of updating the heat and mass transfer source terms in LES and MMC equations in spray combustion modelling are explained in those chapters. These source terms are associated with the evaporation rate. Evaporation plays an important role in the combustion of liquid spray leading to heat and mass transfer processes taking place due to the production of volatile mass from evaporative fuel. In this chapter, the results of non-reacting acetone but evaporating cases of [1] are presented as a part of validating the heat and mass transfer model that has been derived in Chapter 2. There has been past numerical studies of evaporating cases [85, 136] simulated in LES with the Lagrangian fuel particle model. The quality of the results in the present study is validated with experimental data and the past studies.

Non-reacting acetone cases	**SP4**	**SP6**
Bulk jet velocity, U_{jet} (m/s)	24	36
Carrier mass flow rate (g/min)	150	225
Liquid fuel injection rate (g/min)	75	45
Measured liquid flow rate at exit (g/min)	10.3	26.7
Measured temperature at jet exit plane (^{0}C)	-6.5	-7
Co-flow bulk velocity (m/s) of air	4.5	4.5
Bulk velocity in pilot stream (m/s) of air	4.5	4.5
Vapour fuel flow rate at jet exit (g/min)	13.1	18.3
Mixture fraction at exit plane	0.08	0.0752
Reynolds number	18000	28100
Stokes number range at exit plane	0.11 - 2.06	0.11 - 2.06

Table 6.1: The boundary conditions for SP4 and SP6 cases

6.2 Case specific set up and boundary conditions

The non-reacting acetone case is set up with the base model grid resolution, pressure and velocity boundary conditions. The boundary conditions that have been applied are relevant to SP4 and SP6 cases as shown in Table 6.1. For the inflow velocity boundary conditions, mean, variance, and bulk velocity data are used to generate time varying inflow velocity with a realistic turbulent spectrum. For the evaporation cases, the initial mixture fraction is calculated based on the exit plane vapour fuel flow rates and carrier mass flow rate according to Eqn. 4.1. The temperature boundary condition is applied for the main jet according to relevant cases as shown in Table 6.1,

whereas, for the other patches, temperature is set at 293k. For acetone, oxygen and nitrogen species, non-reacting equivalent species tables are created for the thermophysical coupling. The primary species is set as oxygen in the thermophysical coupling and JANAF thermodynamic data are used for the enthalpy calculation. The surface mixture fraction of droplets is calculated based on the Clausius Clapeyron evaporation submodel and the carrier phase mixture fraction is obtained from the MMC simulation.

6.3 Results and analysis

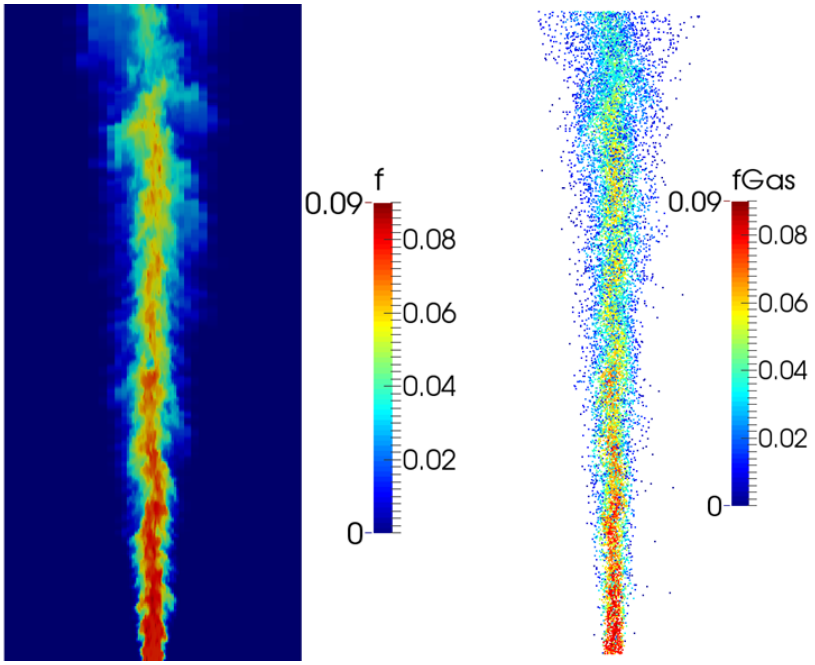

Figure 6.1: Instantaneous mixture fraction profile; LES mixture fraction (left) and particle gas mixture fraction (right)

The simulation is performed for non-reacting but evaporating cases [1] to validate the mixture fraction based liquid spray model that has been derived in Chapter 2. The simulation is now attempted to investigate a number of features, such as, validating the evaporation model and validating the evaporation rate with experimental data, testing of

the mixture fraction approach and transfer equations and updating LES source terms due to heat and mass transfer between the carrier and liquid phases.

6.3.1 Evaporation rate

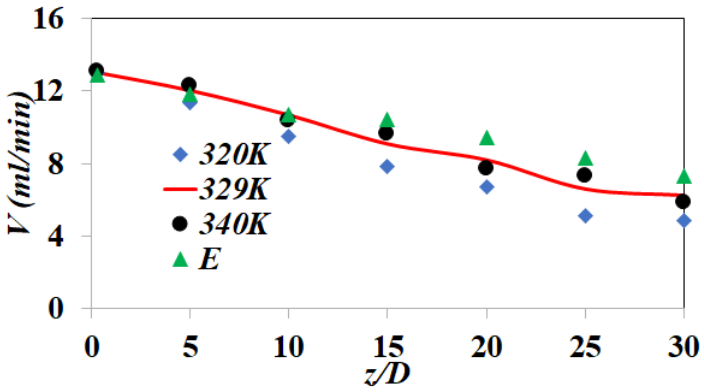

Figure 6.2: Liquid volume flow rate, *V (ml/min)*, in SP4 case for different boiling temperatures *320K, 329K, 340K* and the experimental data (*E*).

The variation of the liquid volume flow rate downstream of the injection is an indicator of evaporation rate. The liquid volume flow rate is calculated in different axial locations as shown in Figure 6.2. It is found that the liquid volume flow rate decreases from exit plane to downstream. Evaporation continues as expected in the downstream, where the temperature of the surrounding carrier phase is higher compared to the jet exit plane. In the exit plane, the initial temperature is low due to major pre-evaporation taking place just before the exit plane as evaporation is started after injection of droplets from the nebulizer and before reaching the exit plane. The simulation results of the liquid volume flow rate are in good agreement with the experiment up to $z/D = 10$ location, whereas it is a little bit underpredicted in the rest of the axial positions. The measurement results vary up to $10 - 15\%$ [1] due to experimental uncertainty. The simulation is performed for different acetone boiling temperatures. The actual boiling temperature of acetone is $329K$. The

simulation is done for temperature as high as $340K$ and temperature as low as $320K$. It is clear that with lower boiling temperature, there is reduction of the liquid volume flow rate (see in Figure 6.2) i.e. evaporation rate has increased. With higher boiling temperature, the liquid volume flow rate is very close to the result of the actual boiling temperature ($329K$). Overall, the simulation results of the three sets of boiling temperature range show the exact physical trend and the rate of evaporation when the exact boiling point is chosen which is in satisfactory agreement with the data.

6.3.2 Mean velocity profile

The mean axial velocities along the centreline are shown in Figure 6.3 for SP4 and SP6 cases. The velocities of the smallest droplets ($0 - 10\mu m$), carrier and experimental results are compared. As expected, due to their small Stokes number the small droplets and carrier have very similar velocities. Both match the experimental data well. The simulation results nicely capture jet break up around z/D=5 location and subsequent decay further downstream. The radial profile of mean axial velocities is shown in Figures 6.4

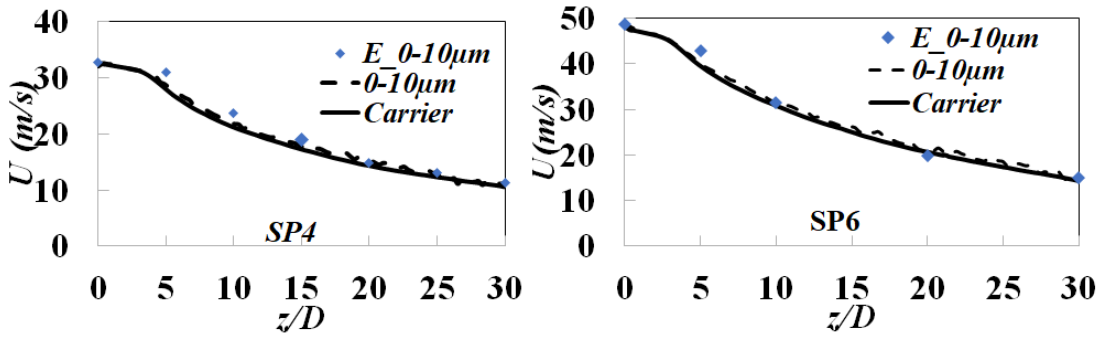

Figure 6.3: Axial centreline mean velocity profile of SP4 (left side) and SP6 case (right side).

and 6.5 for particle size ranges of $10 - 20\mu m$, $20 - 30\mu m$, $30 - 40\mu m$ and $40 - 50\mu m$ respectively. The predictions are in very good agreement with the experimental results.

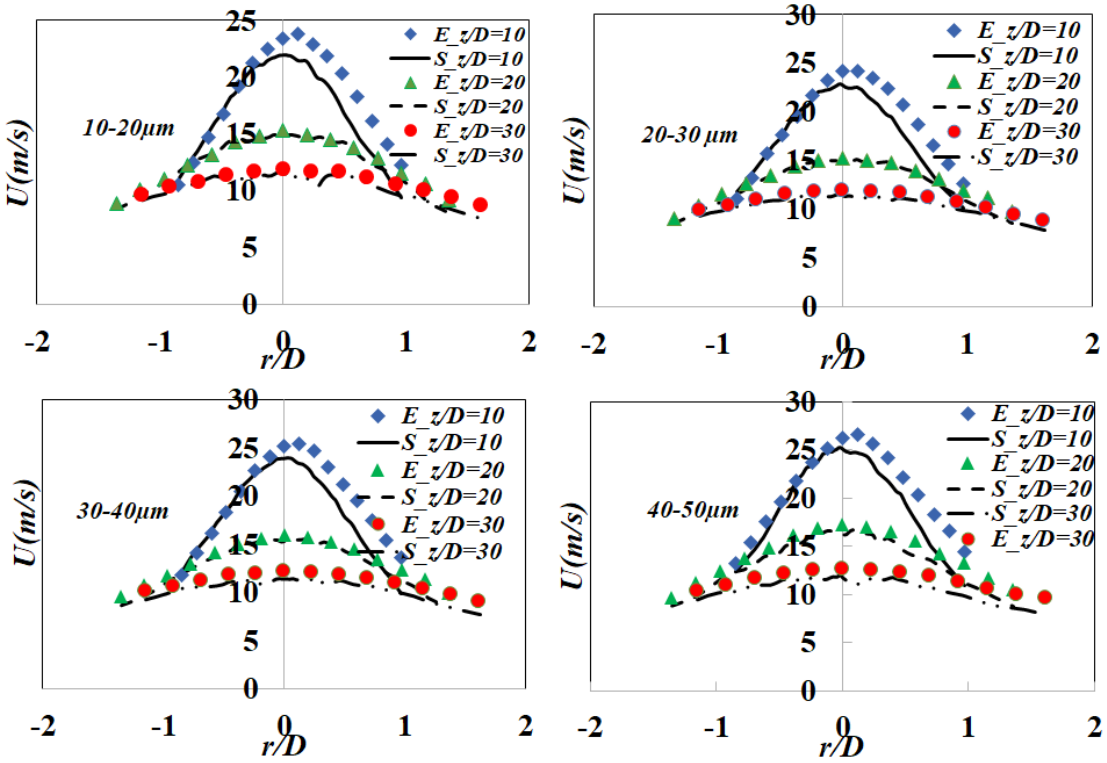

Figure 6.4: Radial profiles of mean axial velocity for different droplet classes of SP4 case.

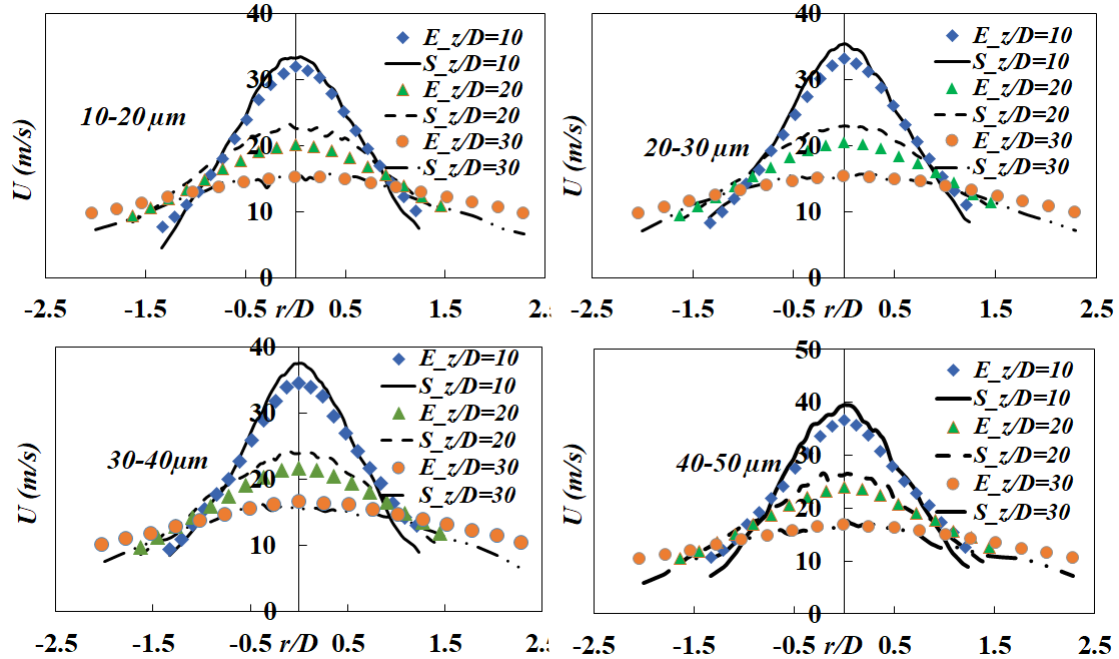

Figure 6.5: Radial profiles of mean axial velocity for different droplet classes of SP6 case.

Even comparing to kerosene cases, the evaporation cases are showing encouraging results.

6.3.3 RMS velocity profile

The centreline and radial profiles of the RMS of the axial velocity for cases SP4 and SP6 are shown in Figures 6.6 and 6.7 for the droplet size of $10 - 20\mu m$. The RMS profile along the centreline is showing good agreement, except there is a significant discrepancy at $z/D = 10$, which is the similar to the results of kerosene cases. The measurement uncertainties were 15 % for the RMS velocity as recorded by Gounder and Masri. The error bars are introduced in figures 6.6 and 6.7, which show discrepancies at $z/D = 10$, while the close agreement is found at all other axial and radial locations. The simulation results of Ukai et. al. also found similar discrepancy.

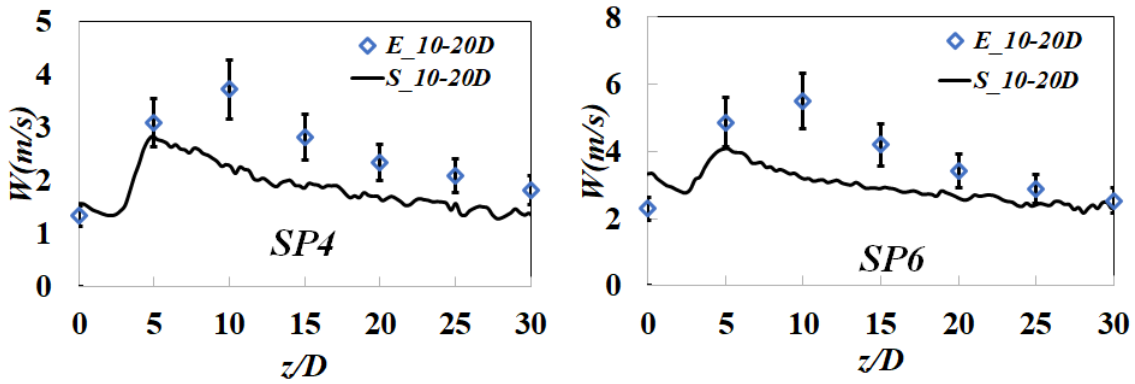

Figure 6.6: Axial profile of RMS velocity of SP4 and SP6 cases with experimental error bars.

6.3.4 Droplet temperature

The instantaneous droplet temperature is shown on the left side of Figure 6.8a. The temperature in the downstream is found to be lower compared to the upstream as the evaporation rate is higher in the downstream due to higher surrounding gas temperature

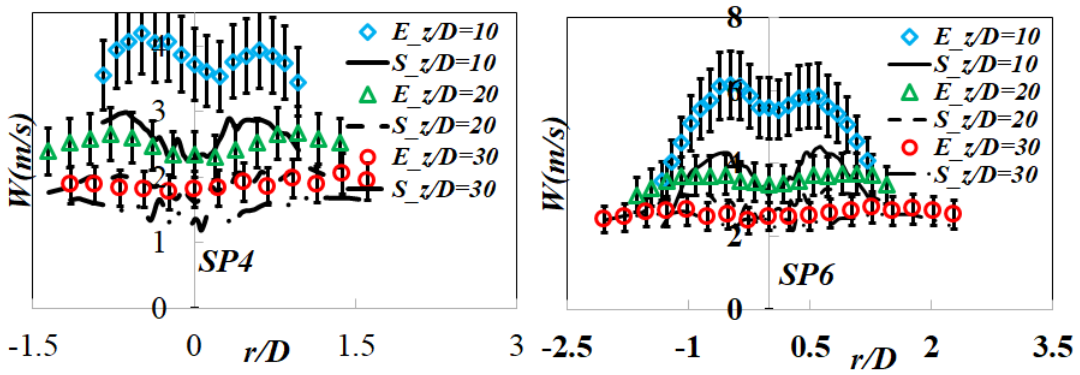

Figure 6.7: Radial profile of RMS velocity of SP4 and SP6 cases with experimental error bars.

(see the right side of Figure 6.8a). The lower internal heating in the downstream is also indicating the cooling of fuel droplets (see the left side Figure 6.8b). This can be explained with the expression of internal heating, Eqn. 2.27 rewritten as following

$$q_D = \frac{\hat{h}_G - \hat{h}_S}{(1 + B_M)^Z - 1} - (\hat{h}_S - \hat{h}_D) + q_R$$

where the first term represents convective heat and the rest is latent heat. The latent heat increases with the increase of evaporation resulting lowering the value of internal heat and consequently the temperature drop of fuel droplets in the downstream. The mass flux is also shown on the right side of Figure 6.8b, which shows higher mass flux in the downstream and it also indicates why the temperature is lower in the downstream. It is expected as the evaporating mass takes away heat from the surface of the droplets resulting in low temperature in the downstream.

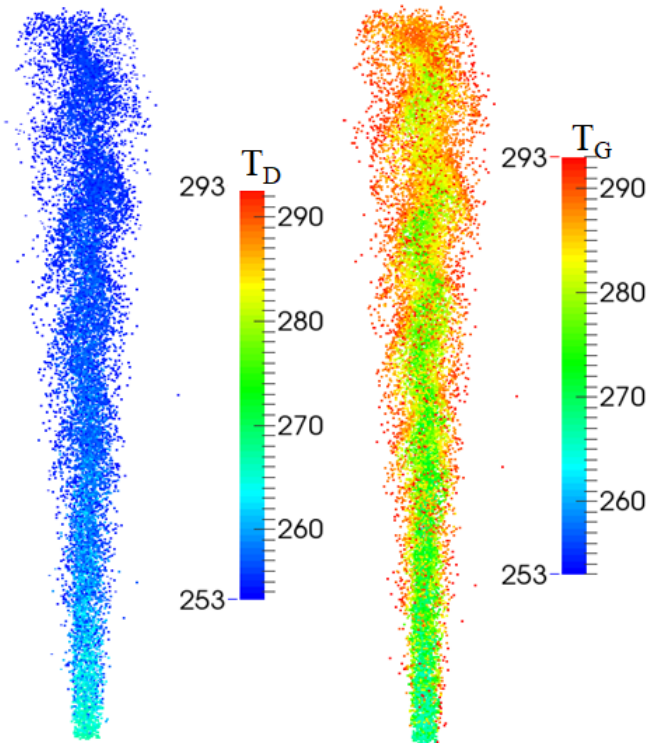

(a)

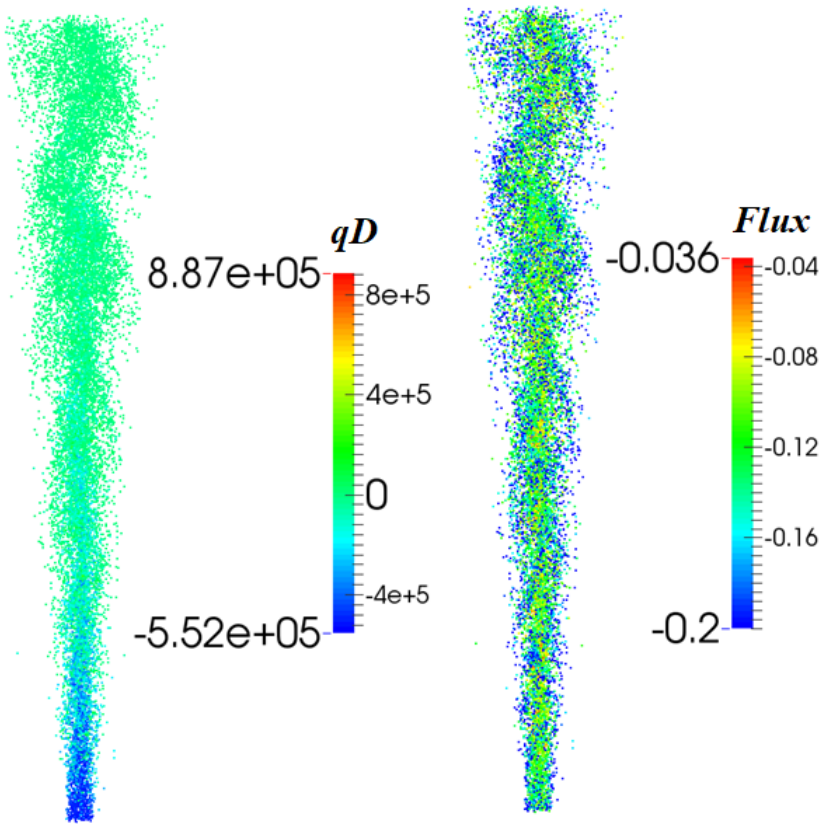

(b)

Figure 6.8: (a) Droplet temperature, T_D, (left side), gas temperature, T_G, (right side) and (b) Internal heat, q_D, (left side) and droplet mass flux, $Flux$, (right side) of SP4 case.

6.4 Discussion and conclusions

The simulation is performed for the evaporating acetone cases [1] incorporating new heat and mass transfer model for the liquid phase. The Clausius Clapeyron relation is applied to the liquid phase evaporation model. The mass flux is calculated according to governing equations derived in Chapter 2 by adapting mixture fraction based Spalding's [84] model for heat and mass transfer. The evaporation source term is added to the continuity, momentum and mixture fraction transport equations and updated from the LFP. The validity of evaporation model is tested through comparing of liquid flow rate which shows qualitatively good agreement with the experimental data of SP4 case.

The simulated results of axial and radial mean velocity of droplets show good agreement with the experiment data. Compared to the study of Ukai *et al.* [86, 136] this study captures similar qualitative results. The axial centreline RMS velocity of droplets are also qualitatively good but showing under-prediction after the jet break-up at *z/D=5*. Ukai *et al.* found 10- 20 % under prediction at *z/D=10*, whereas this study under-predicted around 40% at *z/D=10* while the prediction is well in all other stations. The radial RMS velocity of droplets is also underpredicted at *z/D=10* whereas the prediction has improved at *z/D=20, 30* test positions. The temperature of droplets is found lower in the downstream due to the influence of higher evaporation rate.

Overall the prediction of evaporating cases is in good agreement with the experimental data [1] and the previous study of Ukai *et al.* [86]. The simulation has successfully implemented a new Lagrangian particle based model for the heat and mass transfer between the liquid and gas phases in OpenFOAM CFD code. The developed new model has been applied in reacting cases and the results have been presented in Chapter 7.

Chapter 7

Simulations of reacting acetone

7.1 Introduction

This chapter is devoted to the study of reacting acetone cases [1]. The governing equations for the combustion of multiphase flow were derived in Chapter 3. The LES based multiphase combustion model is developed with the inclusion of two Lagrangian particle based subgrid models; the sparse Lagrangian MMC model for the gas phase and the Lagrangian particle model for the discrete liquid phase. The subgrid models are implemented in two separate Lagrangian particle based codes and coupled with the LES based finite volume CFD code. The coupling between the gas phase MMC and the liquid phase LFP model is done in both the physical and the reference mixture fraction spaces according to the formulations derived in Chapters 2 and 3. The finite rate chemistry is applied with a chemical mechanism and the optically thin assumption for radiation is used. The species transport equations are solved using the stochastic Lagrangian particle approach applying the MMC-Curl mixing model with the introduction of a locality

Reacting acetone cases	**AcF1**	**AcF2**
Bulk jet velocity, U_{jet} (m/s)	24	36
Carrier mass flow rate (g/min)	150	225
Liquid fuel injection rate (g/min)	75	75
Measured liquid flow rate at exit (g/min)	18	23.9
Measured temperature at jet exit plane (K)	293K	293K
Co-flow bulk velocity (m/s) of air	4.5	4.5
Bulk velocity in pilot stream (m/s) of air	11.9	11.9
Vapour fuel flow rate at jet exit (g/min)	57.0	51.1
Mixture fraction at exit plane	0.275	0.185
Reynolds number	24400	32100
Stokes number range at exit plane	0.11 – 2.06	0.11 – 2.06

Figure 7.1: The boundary conditions for the reacting acetone cases.

parameter for the micromixing operation [2]. The simulation results are validated with the experimental data [1] and a previous study [86].

7.2 Case specific set up and boundary conditions

The reactive acetone cases investigated in this study are the partially premixed type and the mixture fraction boundary condition is applied based on the pre-evaporated mass vapour and carrier air flow rate as shown in Table 7.1. The mixture fraction at the exit plane was 0.275 and 0.185 for the cases of AcF1 and AcF2, respectively [1]. The bulk

velocity for the pilot stream was 11.9 m/s for all cases. The pilot mixture fraction is calculated as 0.0858 for all cases based on the stoichiometric equivalent mixture fraction of the pilot species: acetylene, hydrogen and air. The initial temperature of the droplets was not measured in the experiment, and the temperature was suggested 293K by Gounder *et al.* [1]. The chemical mechanism of Chong and Hochgreb [158] is used for this study consisting of 38 species and 224 chemical reactions.

7.3 Results and analysis

The details of the geometry, mesh and numerical schemes were given in Chapter 4, where the grid sensitivity study was elaborated for the reacting cases. The resolution of the stochastic particle number in LES mesh is also important for the minimal variation of results due to particle mixing and the accuracy of the gas phase simulation. Moreover, particle number control is also important for the heat and mass transfer coupling between LFP and MMC, which ensures consistent pairing of each fuel particle defined in the LES field corresponding to one stochastic particle. However, the computational cost increases with the increase of particle numbers. The investigation is sought after for the independence of prediction to the number of stochastic particles.

The values of f_m and r_m are model parameters which can be selected to produce a defined level of localness in both the mixture fraction and physical spaces. However, for the converged solution these parameters need to be studied. The sensitivity of f_m and r_m is studied in some MMC publications [135, 2, 164] where there are a range of f_m values showing no sensitivity in the simulation. The f_m value is chosen as 0.03 according to those studies while the sensitivity of r_m is studied through different particle density. The

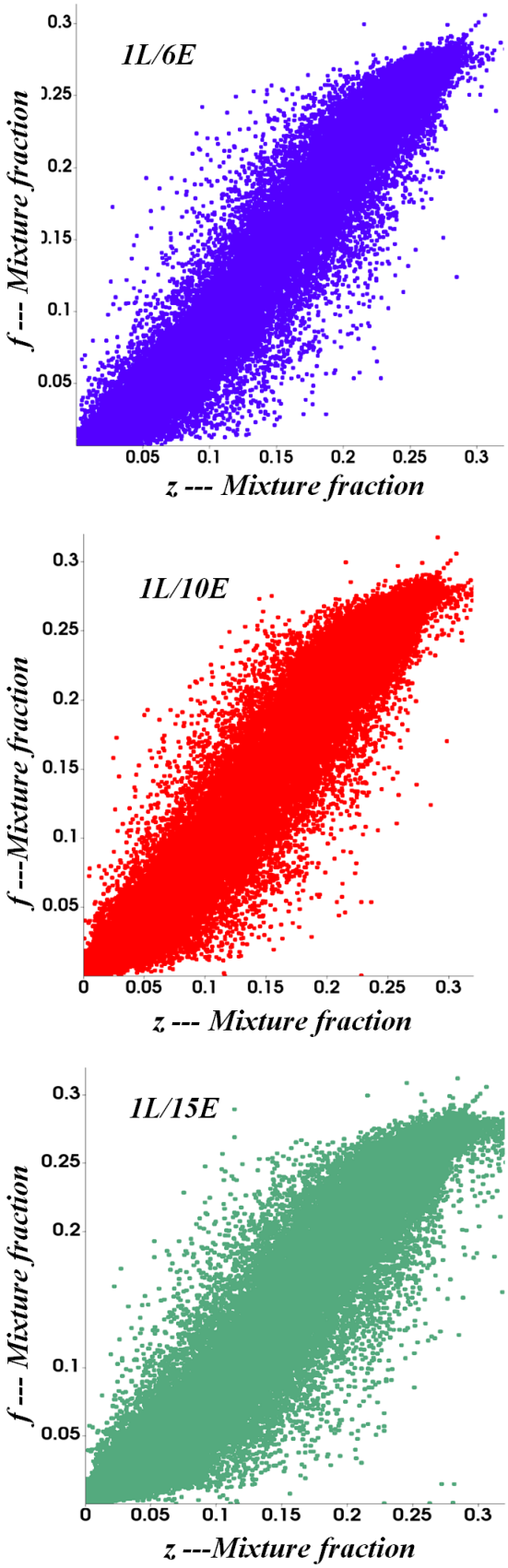

Figure 7.2: The scatter plot showing *f vs z* mixture fraction with varying stochastic particle numbers.

Cases	Number density	Total no. particles	f_m	r_m (mm)
1	1L/6E	180480	0.03	2.56
2	1L/10E	135360	0.03	2.89
3	1L/15E	90240	0.03	3.44

Table 7.1: Test cases for sensitivity of particles.

summary of test cases is shown in Table 7.1. The number of each Lagrangian stochastic particle is set proportional to the number of LES cells. For this study, 1 Lagrangian particle proportional to 15, 10 and 6 LES cells defined as *1L/15E*, *1L/10E* and *1L/6E* respectively is selected for the sensitivity study. For the multiphase simulation, the correlation between the reference mixture fraction and the particle mixture fraction also needs to be tested at the same time with the particle sensitivity test.

The correlation between the reference mixture fraction and the particle mixture at the stochastic particle location is a good indication of consistency between the LES - MMC fields. The scatter plots of particles for the LES reference mixture fraction, f and the stochastic particle mixture fraction, z, are shown in Figure 7.2 for the three test cases. The scatter plots are showing excellent correlation between the two mixture fractions at the stochastic particle location.

For the evaporation of spray flame, the evaporated gas mixes with the surrounding gas mixture and the mixing is characteristically local in composition space. Heye *et al.* [165] introduced random selection of subgrid gas particles for the pairing with evaporating fuel droplets. Although the conditional evaporation rate is evaluated for each droplet,

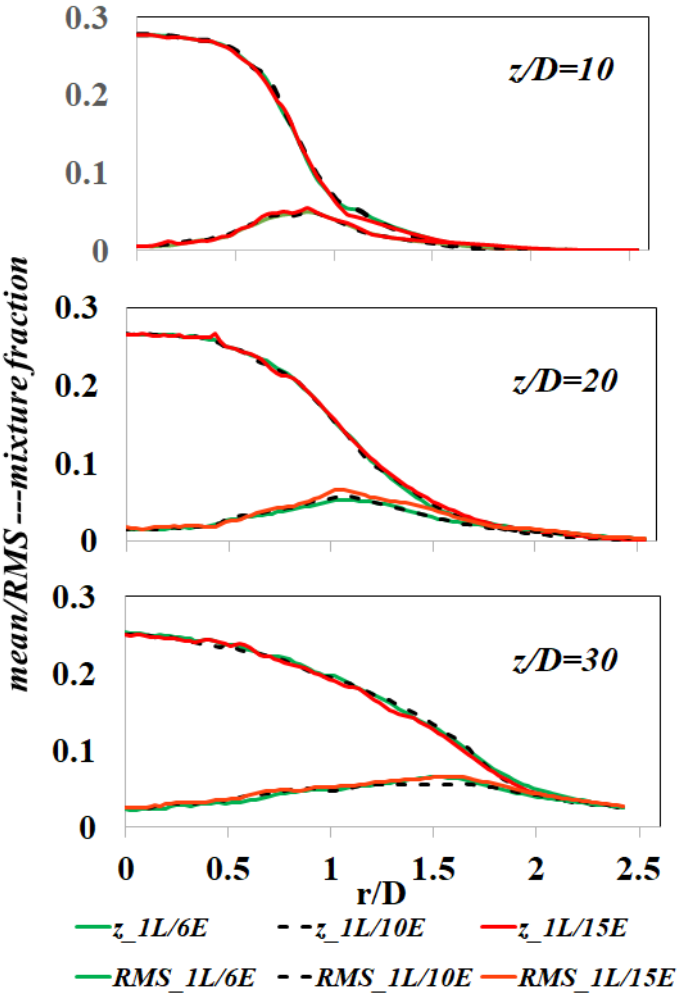

Figure 7.3: The mean and RMS of gas phase mixture fraction at differnt axial locations.

which is an improvement of their previous work [147], it is still not local in composition space. For this study, the Lagrangian fuel particle model is developed and coupled with previously developed MMC. The novelty of this study is to introduce a robust coupling scheme, which selects a stochastic particle for pairing with each fuel droplet in physical proximity of reference mixture fraction space that ensures the localness of evaporation rate in composition space. For testing the accuracy of coupling scheme, the simulation is also performed with the random selection of stochastic particle for pairing each fuel droplets. The scatter plot of temperature vs z is shown in 7.4 for both local and random selection method. The scatter plot shows the random selection method produces jump

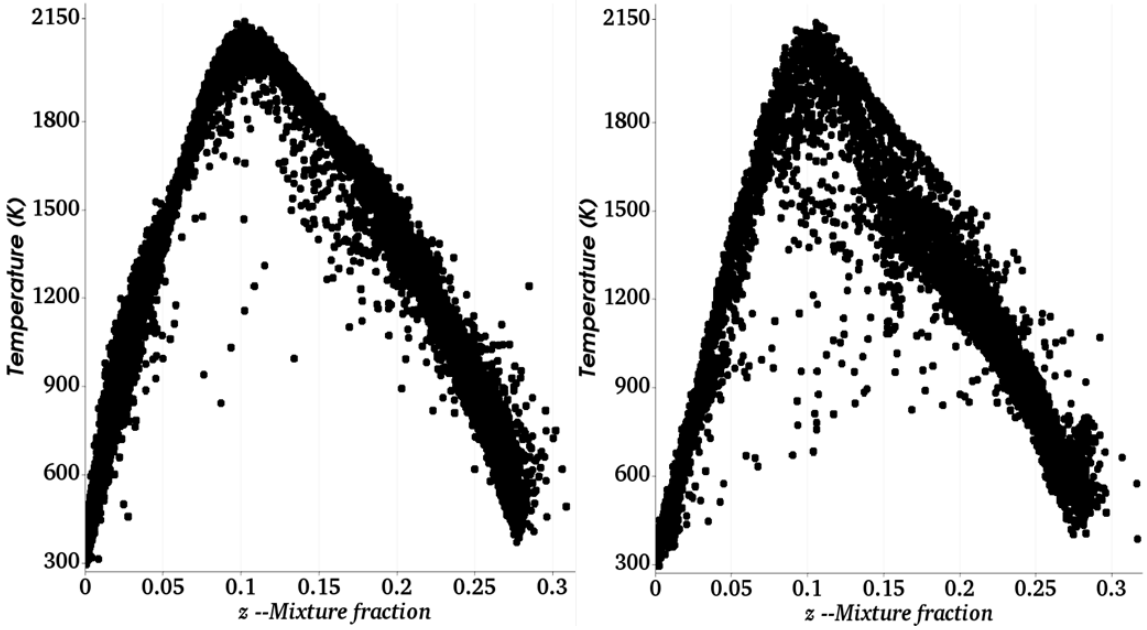

Figure 7.4: Comparison of local (left) vs random (right) particle selection method at *z/D=30* location in AcF1 case.

and departs from the locality in large extend compared to the local method that justifies the accuracy of the coupling scheme proposed in this study

The sensitivity of the stochastic particles is verified with the simulation results of mean and RMS temperature and mixture fraction at different axial locations. The simulation results of the mean temperature are also compared to the experimental data. The mean and RMS of the gas phase mixture fraction are shown in Figure 7.3 for the three sets of particle number density at *z/D=10, 20* and *30* locations where the results are nicely matching each other. The mean and RMS temperatures are also shown in Figure 7.5 which are in good agreement with each other at all axial positions. However, a very negligible mismatch is found in both mixture fraction and temperature prediction for the case *1L/15E*, which is the course case among the three. The cases *1L/6E* and *1L/10E* are showing an exact match to each other. While the experimental data for the mixture fraction are not available, the measurement mean temperature is also compared to the

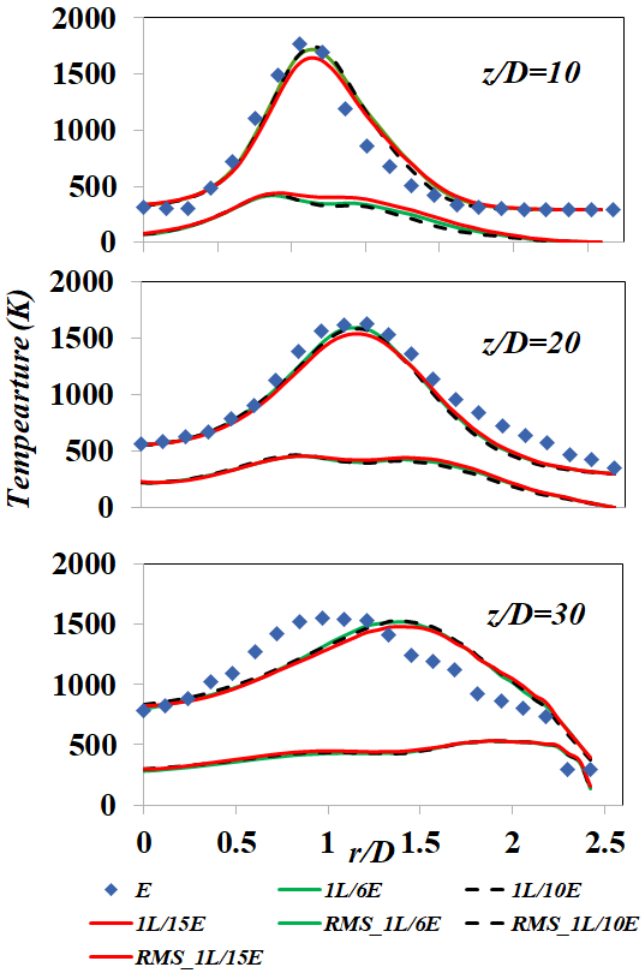

Figure 7.5: The mean and RMS of gas phase temperature at different axial test positions.

prediction, which shows good agreement at *z/D=10, 20* stations and a little jet spreading at *z/D=30*. For the final simulation, the particle density *1L/10E* is chosen for this study with f_m value 0.03.

7.3.1 The statistics of scalars

The statistics of each reactive species are available in the MMC stochastic Lagrangian particle simulation. The acetone is a highly reactive chemical species, and it decomposes very fast to some other intermediate species. The scatter plots of stochastic particle mass fractions of O2, CH3COCH3, OH, H2O, CO2 and CO are shown in Figure 7.6 at *z/D=10*

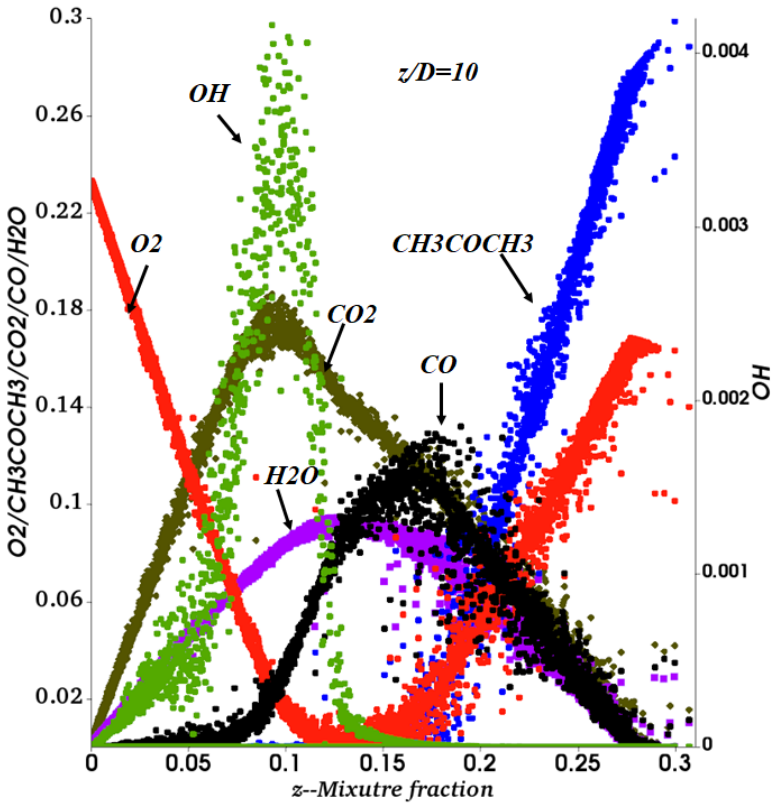

Figure 7.6: The species O2, CH3COCH3, OH, H2O, CO2 and CO mass fraction profiles in AcF1 case at *z/D=10* axial test position.

axial location. The oxidizer (O2) and acetone (CH3COCH3) fuel are clearly showing rich (right) and lean (left) sides and a stoichiometric point, 0.095. The product CO2 is following the peak value of OH at the stoichiometric point, which is the highly reactive zone producing peak value of CO2. The product CO is formed on the rich side of the fuel stream following the CO2 profile. However, the lower mass fraction of CO is near the stoichiometric point due to further reactions to produce CO2, and the peak value of CO2 is found at stoichiometric. The mass fraction of H2O is an indicator of heat release due to chemical reactions, and the peak value of H2O is found before the stoichiometric point (from the right side).

The instantaneous scatter image of mass fraction and temperature profiles is shown in Figures 7.7 at *z/D=10* axial location. In the Figure, the mass fractions of OH, H2,

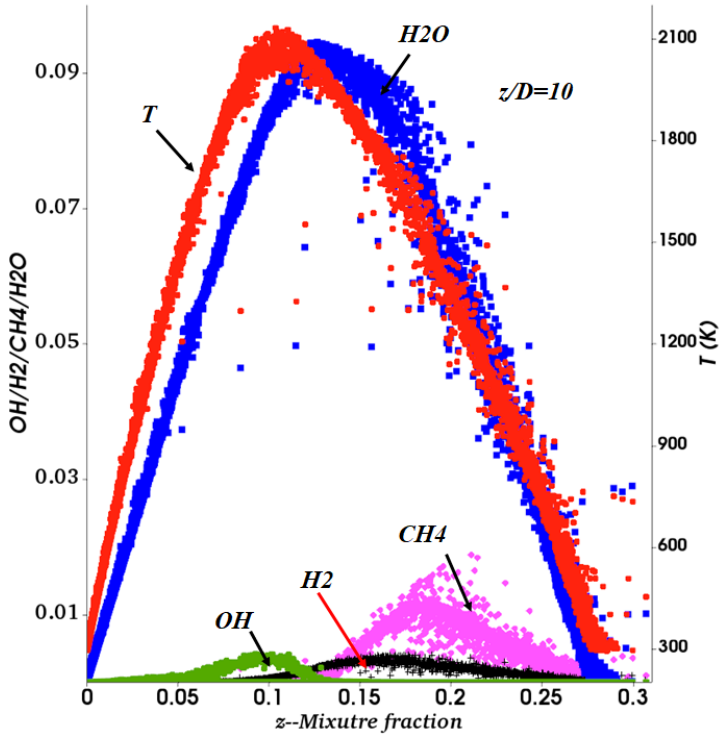

Figure 7.7: The species mass fraction profiles of OH, H2, CH4, H2O and temperature profile in AcF1 case at *z/D=10*.

CH4 and H2O are shown along with the temperature profile. The intermediate species CH4 is produced immediately in the rich fuel stream side, and further decomposition of CH4 occurs in the successive reactions. The overlapping profiles of OH and H2 show the peak reaction zone, and the heat release to H2O and consequently the peak temperature is found just after the peak value of H2O.

The contour plot of the OH profile is shown in Figure 7.8 where the concentration of *OH* is found in the outer periphery of droplet clouds which is similar to the experimental observation [1]. The droplet clouds are shown in the left side of Figure 7.8 with the gas phase mixture fraction showing the stoichiometric value 0.095 at the outer boundary of droplets.

The above scatter and contour plots are demonstrating the trend of species mass fraction profiles in an acetone combustion case. The acetone mass fraction profile is

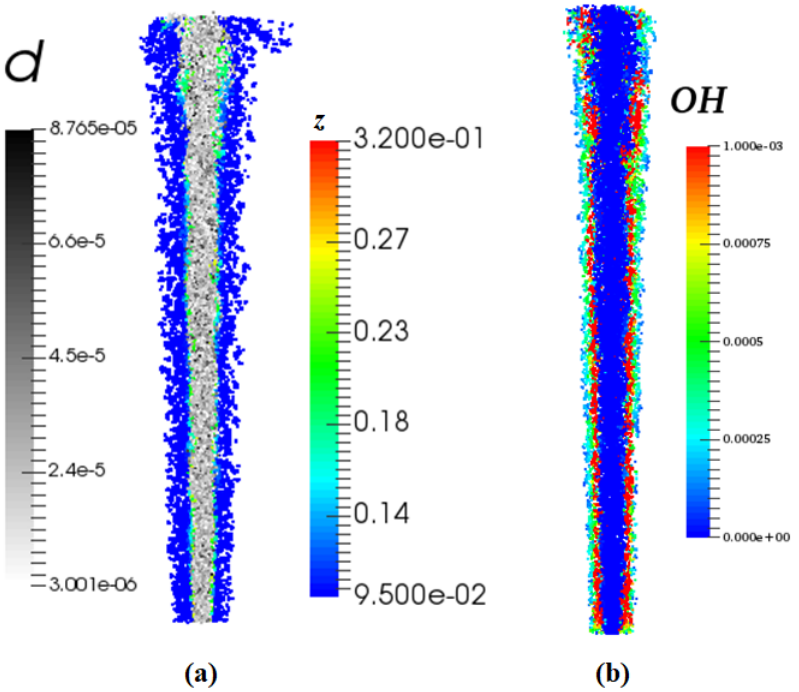

Figure 7.8: (a)The instantaneous contour plot of droplet diameters (left) with gas phase mixture fraction (right) and (b) The *OH* profile.

clearly showing the lean, stoichiometric and rich fuel zones and combustion and mixing lines.

7.3.2 The mixture fraction profiles

The consistency of the coupling schemes can be tested by comparing the LES and MMC mixture fraction fields. An instantaneous contour image of the reference mixture fraction, f, (at the location of the stochastic particle) and the gas phase mixture fraction, z, in the stochastic particle is shown in Figure 7.9 in the AcF1 case; it shows good correlation between the two profiles. The radial profiles of the two mixture fractions at z=*10,20* and *30* locations are also shown in Figures 7.10 and 7.11 for the AcF1 and AcF2 cases. Again it shows both quantitative and qualitative correlation between the two mixture fractions at all test positions.

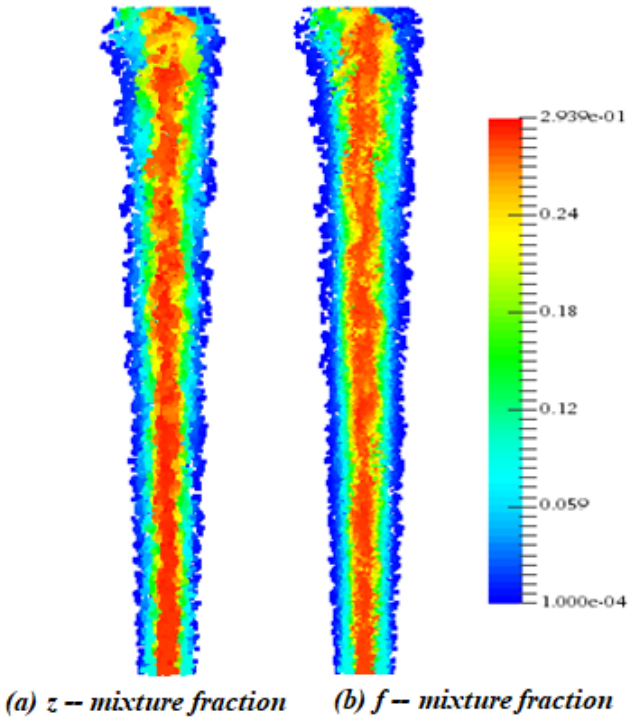

Figure 7.9: Instantaneous contours of f and z mixture fraction fields at the stochastic particle locations.

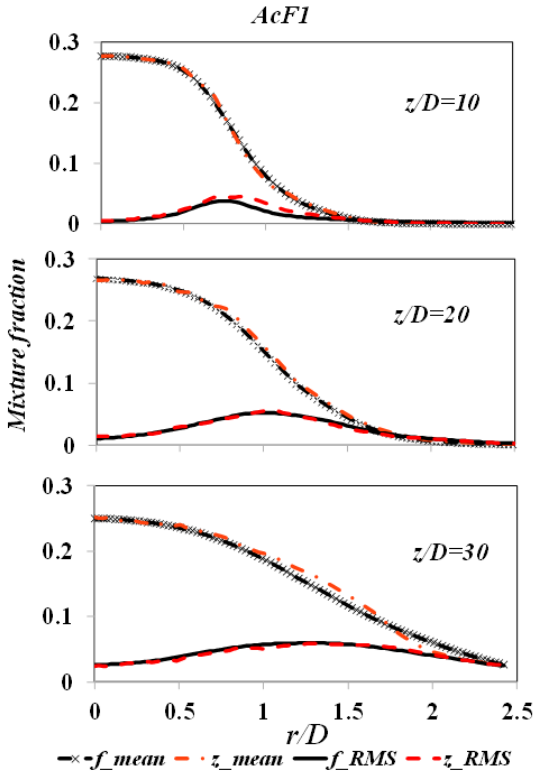

Figure 7.10: The radial profiles of f and z mixture fraction of AcF1 case.

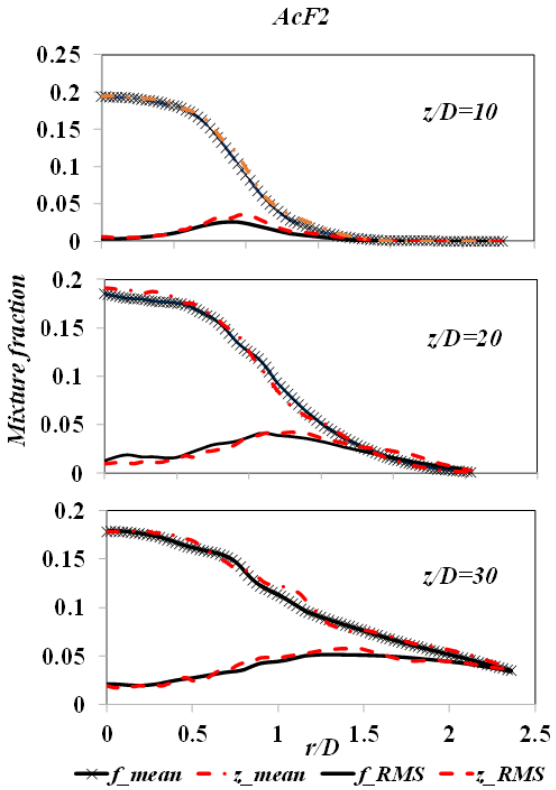

Figure 7.11: The radial profiles of f and z mixture fraction of AcF2 case.

7.3.3 The temperature profiles

The radial profiles of the gaseous temperatures of AcF1 and AcF2 are shown in Figures 7.12 and 7.13 at z/D=10,20 and 30, respectively. There is an excellent agreement of mean temperature in the AcF1 case in the first two locations while jet spreading is found at z/D = 30 relative to the experimental data. The mean temperature of the AcF2 case is also well predicted in first two stations but a little bit underpredicted at z/D=30 location on the right side. The mean peak temperature is well predicted in the shear layer at all axial locations. The discrepancy of mean temperature in the two cases is within the experimental error range of 15 %. The RMS profiles of temperature are also shown where the peak is found in the inner side of the shear layer while at z/D = 30 the RMS is more evenly distributed across the radial profile with a smaller peak in the

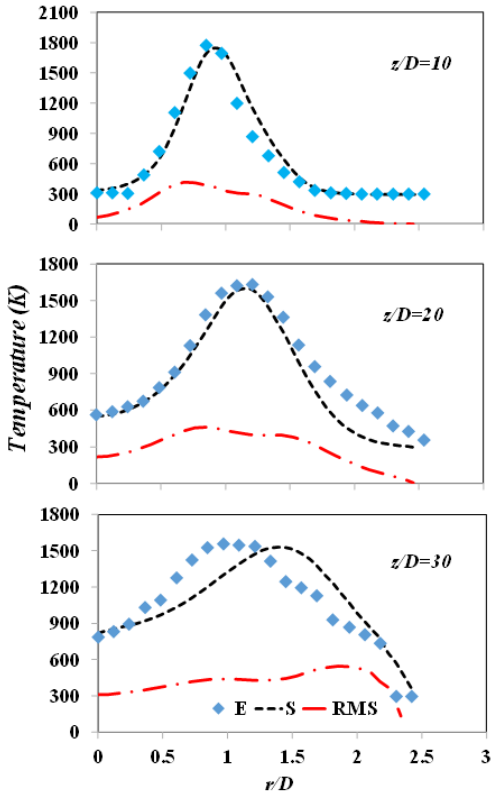

Figure 7.12: Radial profiles of mean (up) and RMS (down) temperature of AcF1 case.

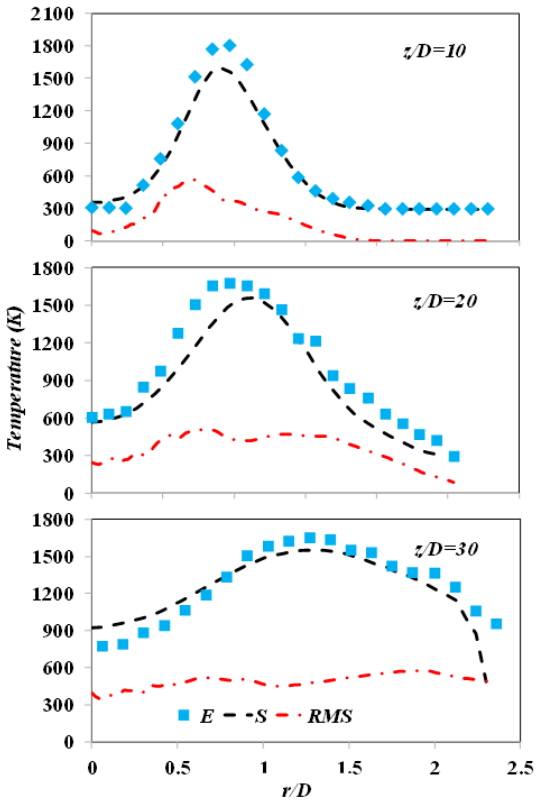

Figure 7.13: Radial profiles of mean (up) and RMS temperature (down) of AcF2 case.

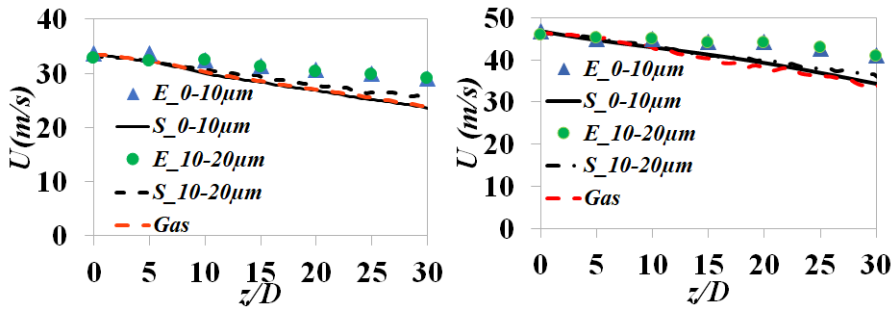

Figure 7.14: Axial centerline velocity of AcF1 (left) and AcF2 (right) case.

outer edge of the side of the shear layer in the AcF1 case at *z/D=30*. Although the RMS temperature is not available in the experimental data for comparison, the simulation results are shown for completeness. Overall the mean temperature is well predicted compared to the experimental study and the similar to the study of Ukai *et al.* [86].

7.3.4 Axial and radial velocity profiles

The axial centreline mean velocity for the droplet class of $0 - 10\mu m$ and $10 - 20\mu m$, is compared to the experimental data in Figure 7.14 for cases AcF1 (left side) and AcF2 (right side). For comparison, the predicted gaseous mean velocity is also shown and found to be very similar to the small droplet velocity on account of their low Stokes numbers. All the predictions are in good agreement with the data except for slight underprediction in downstream in both cases.

The mean and RMS velocity of the AcF1 case at different axial positions of the domain are shown in Figure 7.15 for the droplet class of $10 - 20\mu m$ and $30 - 40\mu m$. The radial profiles of the mean and RMS velocity of the AcF2 case are also shown in Figure 7.16 which shows similar accuracy and trend to the AcF1 case. The measurement uncertainties were 6% for the mean velocities and 15% for the RMS velocities. The presented results were compared to the previous study of Ukai et al., which show similar

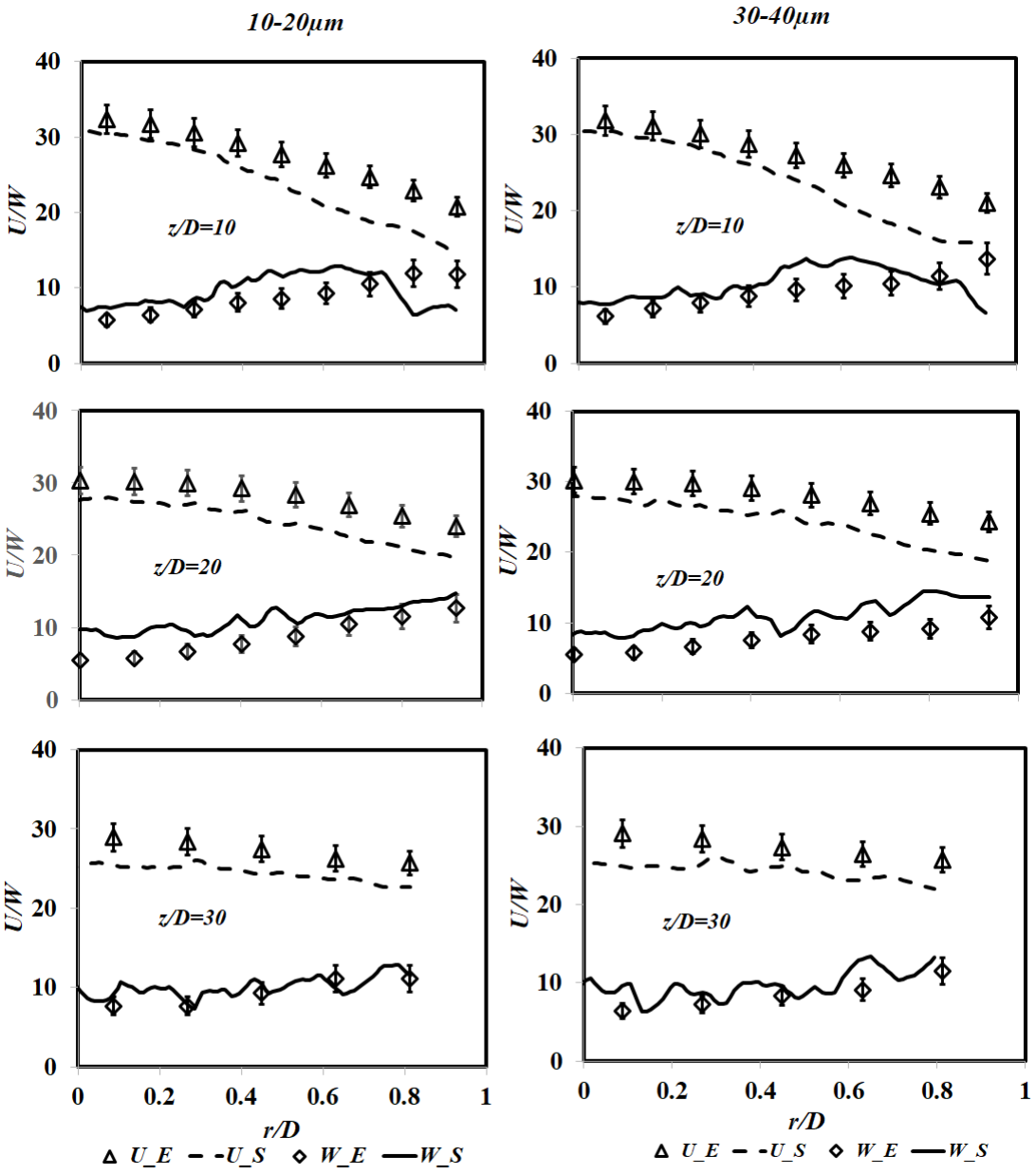

Figure 7.15: Radial profiles of mean (up) and rms (down) velocity of AcF1 case with error bars, RMS values have been multiplied by four for clarity

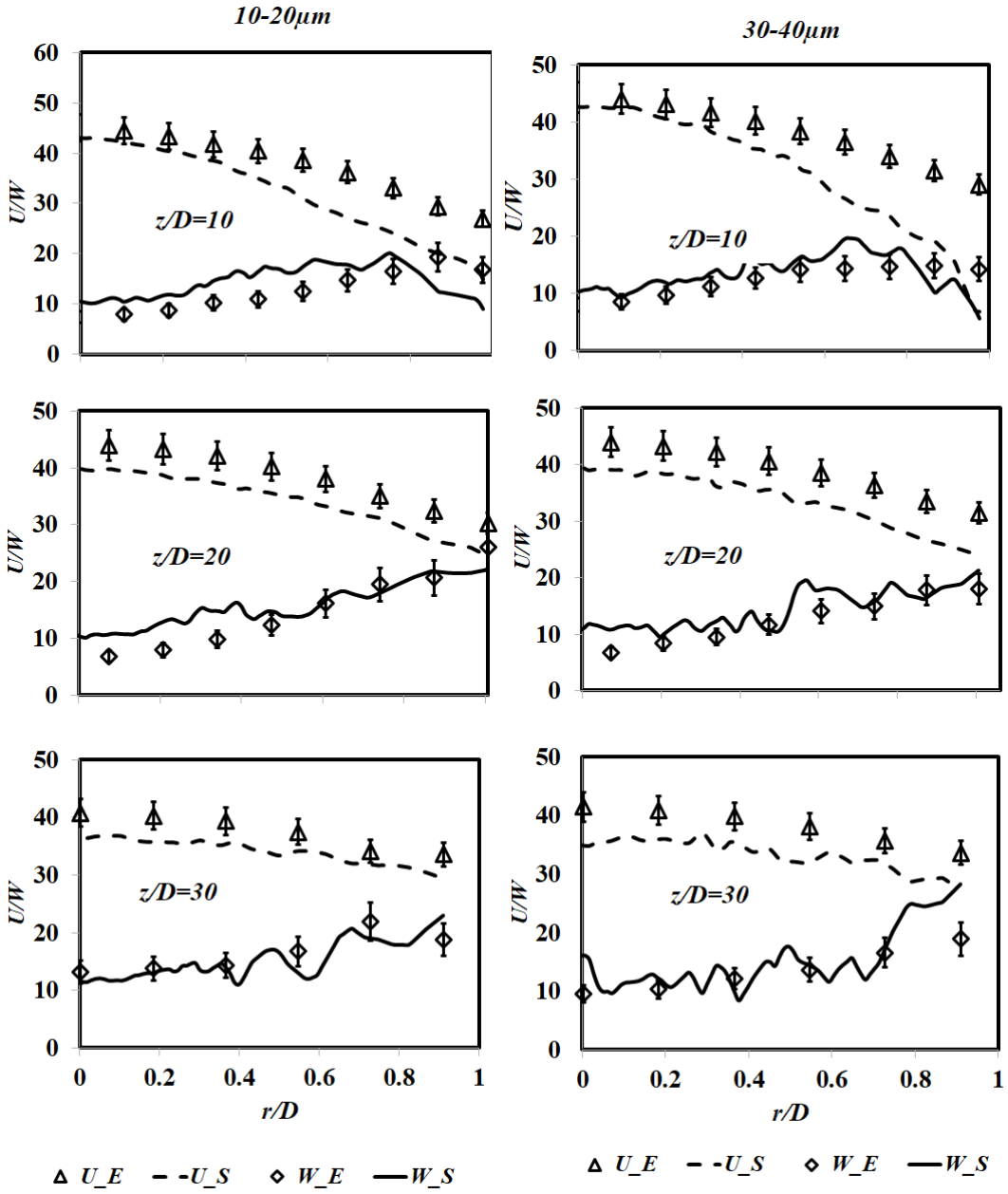

Figure 7.16: Radial profiles of mean (up) and rms (down) velocity of AcF2 case with error bars, RMS values have been multiplied by four for clarity.

trend. The error bars are introduced in figures 7.15 and 7.16, which shows a little bit under-prediction of mean velocity at z/D=10 location, while a reasonable agreement is found at $z/D = 20$ and 30 compared to experimental data. Although the mean velocities are slightly under-predicted at downstream, the RMS velocities are in good agreement with the experimental data [1]. The accuracy of these results is comparable to those in the LES-CMC modelling of Ukai *et al.* [86].

7.4 Discussion and conclusions

The simulation of reacting acetone cases is investigated in a sparse Lagrangian MMC-LES combustion modelling framework incorporating a new heat and mass transfer model for the discrete liquid phase model. The sensitivity of the stochastic particle number and the LES grid is studied for the minimal variation of presented results. The sensitivity of the stochastic particle number is validated through the comparisons of mean and RMS results of both temperature and mixture fraction. The finite rate chemistry is applied with the Chong and Hochgreb [158] Chemical mechanism for the acetone cases. The consistency of the coupling schemes is validated with the mixture fraction information. The consistency between the two mixture fractions shows good agreement with all test locations. The spray cases have different velocity, premixing and mass loading conditions which are simulated with good accuracy. While the mixture fraction data are not available in the experimental study the validation of the combustion model is done by comparing the droplet velocity and temperature.

The accuracy of the gas phase MMC simulation depends on the conditional mean of the mass fraction in reference mixture fraction space. The mass fraction profile of

some primary species is presented which shows the trend of reactants and products in acetone combustion chemistry. The species profiles are clearly showing the reaction zone, fuel-lean and fuel-rich state of the mixture which are consistent with the non-premixed combustion theory. The OH profile is clearly showing the intense reaction zone where the gas phase mixture fraction is at stoichiometric or near stoichiometric.

The mean velocity of droplets in both the axial centreline and radial locations show good agreement with the experimental data [1] except some underprediction at *z/D=30* location in the AcF1 and AcF2 cases. However, the RMS velocity in radial test positions shows good agreement in all locations for both cases. The simulation results of droplet velocity are similar to the prediction of Ukai *et al.* [86].

The radial profiles of gaseous mean temperature at different axial stations show an excellent agreement with the experimental data with little discrepancy at *z/D=30* in both AcF1 and AcF2 cases. Although the RMS of gaseous temperature is not available in the experimental study, the simulated results are shown for completeness.

The reacting cases are simulated with full implementation of the developed multiphase model derived in this study. The accuracy of the coupling schemes is tested. The presented results of LES, MMC and LFP are satisfactory in the reacting cases which is encouraging to apply this developed sparse MMC-LES multiphase model to other complex flames of spray.

Chapter 8

Conclusions and future work

8.1 Conclusions

Spray combustion modelling is a challenging task due to multiple length and time scales in the turbulent flow and combustion process associated with the interaction of the liquid phase with the gas phase. In this study, the LES method is chosen as a preferred method to resolve the computational scales up to the filtered length scale, and the unresolved scales are modelled. There is a need to apply multiphase governing equations for such a flow that has been derived following the separated flow model concept introduced by Kataoka [141] and later by Mortensen and Bilger [142], where the LES filtered equations are derived for both phases and interface. The interface boundary condition is then applied which simplifies the governing equations with unclosed source terms. The subgrid models are developed to close these source terms.

The chemical reaction source term in species transport equations is one of the complex parts of the combustion modelling as the chemical reaction occurs in molecular scales

and needs to be modelled. The CMC method is one of the modelling techniques that can be applied for closing the chemical reaction source term of reacting flows by applying correlation between the species and the reference mixture fraction space. The PDF method is also an effective modelling technique [58, 62] to provide resolution of the species and thus close the chemical reactions and other non-linear source terms. However, the accuracy of the PDF model depends on the appropriate mixing model, and the PDF methods are computationally expensive. For this study the MMC modelling technique has been chosen which unifies the concept of the PDF [71, 59] and CMC methods [47]. Moreover, the sparse nature of stochastic particles is used to solve the FDF equations derived in Chapter 3, which is computationally less costly compared to the PDF method.

A model is required for the momentum interaction and gas production source terms that appear in the multiphase combustion model, which is done by developing a LFP model. A polydispersed, spherical fuel particles based Lagrangian fuel particle model is derived following the approach of Dukowicz [130]. The expressions for heat and mass transfer are required to account for the mass flux due to the evaporation process in the liquid phase which is done by applying a mixture fraction - based Spalding's [84] heat and mass transfer relations. The first expression for the mass flux is derived from the heat transfer perspective where the unclosed term internal heat needs to be modelled. Another expression of mass flux is derived in the mass transfer perspective and by equating the two expressions thus closes the system of equations.

The coupling of LES-MMC-LFP is done elegantly to implement the concept of multiphase modelling that has been derived in Chapter 3. The coupling schemes are basically designed for updating LES source terms from the relevant particle models.

The momentum interaction source term is updated from the LFP, and the simulation is performed with and without updating the momentum source term in the KS7 kerosene case. The axial centreline velocity in the KS7 case shows that the early jet break up occurs without a momentum source term leading to an underprediction. The validation of MMC-LFP coupling is also tested with the consistency of the reference mixture fraction, f, and the particle mixture fraction, z, at the stochastic particle location, which shows excellent correlation between them in all reacting cases.

The simulation starts with the kerosene cases [1] by applying the kinematic part of the code, where the dispersion of fuel particles is tracked as a parcel. The simulation is performed with the introduction of droplet clouds in the domain of the order of $0-100\mu m$ size range with random entrainment of droplets with a mass and diameter maintaining the experimental mass flow rate. The simulated axial and radial profiles of droplet velocities are in good agreement with the experimental data. The RMS velocities are underpredicted while the trend of RMS profiles is qualitatively similar to experimental data. The simulation nicely captures the jet break up and subsequent decay of velocity in the axial centreline.

The evaporating acetone cases [1] are studied with the implementation of heat and mass transfer coupling to account for gas production due to the droplet evaporation. The accuracy of the Clausius Clapeyron evaporation model is assessed by liquid flow rate, which shows qualitatively good agreement with the experimental data. The mean axial and radial of profiles of different classes of droplets are investigated, which show excellent agreement with the experimental data. However, the RMS velocities are underpredicted while the trends are qualitatively similar to the experimental data. Compared to the study

of Ukai *et al.* the prediction of mean velocities is similar whereas the RMS velocity of this study is underpredicted.

A comprehensive investigation of reacting cases [1] is done by applying the multiphase combustion model that has been derived in Chapter 3 involving chemical kinetics and LES-LFP-MMC interactions by coupling schemes. Sensitivity to the LES grid and the stochastic particle number control is studied for the minimal variation in the presented results for the resolution as described in Chapters 4 and 7. Although the mean axial centreline droplet velocities are slightly underpredicted in the downstream, the RMS velocities are in good agreement at all stations. The radial profiles of mean and RMS velocity show a similar trend as axial. The predicted gaseous mean temperatures of the AcF1 and AcF2 cases are found in good agreement with experimental data in all axial locations. The mass fractions of some primary species are presented which show the trend of species consumption in the acetone burning case. Overall the results of the reacting acetone cases are in good agreement with the experimental data and are similar to the study of Ukai *et al.* [86].

The simulation is performed in three categories of spray cases with varying velocity, mass loading and boundary conditions. For the same bulk velocity 24 m/s and a different liquid mass flow rate at exit plane 10.6 and 18.0 g/min in the SP4 and AcF1 cases respectively, the jet break-up is found early at *z/D=5* in the SP4 case, whereas the jet break is delayed in the AcF1 case up to *z/D=15* due to higher mass loading as well as momentum. However, the jet break-up in the kerosene cases (KS6 and KS7) is similar to the SP4 case at around *z/D=5* where the bulk velocities were 36 and 60 m/s with measured liquid flow rate at exit plane being 37.7 and 66.1 g/min. This may be due to momentum

affect contributing to the jet break up early or delaying. The mean velocity is predicted well in all cases except a little underprediction in reacting cases at *z/D=30*. The RMS velocity is underpredicted in kerosene, and the evaporating acetone cases whereas the prediction is good in the reacting acetone cases. The radial profiles of gaseous temperature are nicely captured in both AcF1 and AcF2 cases.

The simulation is performed in OpenFOAM C++ object oriented user-friendly CFD code. The LES based combustion model is coupled with the two subgrid models; MMC and LFP for the gas and liquid phases respectively. The subgrid model for the heat and mass transfer between the liquid and gas phase is newly developed and implemented in mmcFOAM code by coupling with the previously developed gas phase MMC model [135]. The simulation is performed in different spray cases and validated against experimental data and a previous study. The developed new solver is numerically stable, robust and user-friendly. This sparse Lagrangian MMC-LES code can be used in other complex flame cases in liquid spray modelling.

In the simulation, LES grid - cells, stochastic particles and fuel particles were 1331520, 135360 and 1000000, respectively. The simulation takes 20 days in 64 processors for 4 complete flow through in a domain of 367.5 mm length. It roughly takes 20 % for LES, 70 % for stochastic particles and 10 % for fuel droplets simulation cost in each time step. However, the averaging of droplet velocities takes longer time, which is the major part of simulation cost ultimately.

8.2 Recommendations for future work

The aim of this thesis has been to develop a platform for the multiphase combustion modelling of liquid spray. Even though the present study simulates three complex spray cases with the introduction of a novel heat and mass transfer model in sparse Lagrangian MMC-LES simulation, there are some suggestions to further extend this work. The study recommends a new solver for the combustion of multi-component fuels that will be capable of predicting the pollution formation of multi-components bio-fuels, which is a prospective field for an alternative to fossil fuels.

The newly developed liquid phase model is tested for the three spray cases, which shows satisfactory results with respect to the experimental data. However, the liquid droplet dynamics are very complex, and a variety of physical processes and their interaction needs to be tested for a wide range of utilisation in CFD modelling. The evaporation model can be extended to the various equilibrium and non-equilibrium models as a submodel in the newly developed multiphase solver. However, evaporation of liquid droplets would create local fuel-rich and fuel-lean zones leading to partially premixed and non-premixed nature of burning. The coupling of liquid phase with gas phase MMC is having some issues when the pre-evaporated mixture fraction is near to stoichiometric value, and the highly premixed cases with local extinction are very difficult to handle with a single reference mixture fraction variable. Future study can be extended to implement double conditioning approaches so that the highly premixed cases can be modelled with further improvement by this multiphase combustion code. The good thing is that the newly developed solver can handle the multiple reference variables which need some further testing and code development to implement multiple reference variables.

The developed modelling approach can be extended for multi-component fuels with multiple reference variable definition for different fuel species. The existing code has the capability to define multiple mixture fractions for different fuel species. Future work can be done in this direction to apply the combustion model in multi-component bio-fuels. Moreover, future study can be extended from this to onward implementing a wide range of utilities and different combustion flames. The new submodels can be added to the source code, which is easily supported with the existing user-friendly OpenFOAM coding style.

References

[1] James Dakshina Gounder, Agisilaos Kourmatzis, and Assaad Rachid Masri. Turbulent piloted dilute spray flames: Flow fields and droplet dynamics. *Combustion and flame*, 159(11):3372–3397, 2012.

[2] MJ Cleary and AY Klimenko. A detailed quantitative analysis of sparse-lagrangian filtered density function simulations in constant and variable density reacting jet flows. *Physics of Fluids (1994-present)*, 23(11):115102, 2011.

[3] Bp statistical review of world energy 2015.

[4] HH Chiu, HY Kim, and EJ Croke. Internal group combustion of liquid droplets. In *Symposium (international) on combustion*, volume 19, pages 971–980. Elsevier, 1982.

[5] RW Bilger, SB Pope, KNC Bray, and JF Driscoll. Paradigms in turbulent combustion research. *Proceedings of the Combustion Institute*, 30(1):21–42, 2005.

[6] Y. Ge, M.J. Cleary, and A.Y. Klimenko. Sparse-lagrangian {FDF} simulations of sandia flame e with density coupling. *Proceedings of the Combustion Institute*, 33(1):1401 – 1409, 2011.

[7] Tarek Echekki and Epaminondas Mastorakos. Turbulent combustion: concepts, governing equations and modeling strategies. In *Turbulent Combustion Modeling*, pages 19–39. Springer, 2011.

[8] R Stephen. Turns, 2012, an introduction to combustion: Concepts and applications. *INTERNATIONAL EDITION, MCGRAW-HILL*, 2012.

[9] GE Andrews, D Bradley, and SB Lwakabamba. Turbulence and turbulent flame propagation-a critical appraisal. *Combustion and Flame*, 24:285–304, 1975.

[10] A.N. Kolmogorov. The local structure of turbulence in incompressible viscous fluid for very large reynolds number. *Dokl. Akad. Nauk, SSSR*, 30(30):299–303, 1941a.

[11] A.N. Kolmogorov. Dissipation of energy in the locally isotropic turbulence. *Dokl. Akad. Nauk, SSSR*, 32(30):19–21, 1941b.

[12] Stephen B. Pope. *Turbulent Flows*. Cambridge University Press, 2000. Cambridge Books Online.

[13] M Oberlack, R Arlitt, and N Peters. On stochastic damkohler number variations in a homogeneous flow reactor. *Combustion Theory and Modelling*, 4(4):495–510, 2000.

[14] Paul A Libby and Forman A Williams. Turbulent reacting flows. *Turbulent Reacting Flows*, 1, 1980.

[15] Lartigue Selle, Ghislain Lartigue, Thierry Poinsot, R Koch, K-U Schildmacher, W Krebs, B Prade, P Kaufmann, and Denis Veynante. Compressible large eddy

simulation of turbulent combustion in complex geometry on unstructured meshes. *Combustion and Flame*, 137(4):489–505, 2004.

[16] N Peters. The turbulent burning velocity for large-scale and small-scale turbulence. *Journal of Fluid mechanics*, 384:107–132, 1999.

[17] N. Peters. *Turbulent combustion*. Cambridge university press, 2000.

[18] Tarek Echekki and Epaminondas Mastorakos. *Turbulent combustion modeling: Advances, new trends and perspectives*, volume 95. Springer Science & Business Media, 2010.

[19] SP Burke and TEW Schumann. Diffusion flames. In *Proceedings of the Symposium on Combustion*, volume 1, pages 2–11. Elsevier, 1948.

[20] Norbert Peters. Laminar diffusion flamelet models in non-premixed turbulent combustion. *Progress in energy and combustion science*, 10(3):319–339, 1984.

[21] DC Haworth, MC Drake, SB Pope, and RJ Blint. The importance of time-dependent flame structures in stretched laminar flamelet models for turbulent jet diffusion flames. In *Symposium (International) on Combustion*, volume 22, pages 589–597. Elsevier, 1989.

[22] Pascale Domingo, Luc Vervisch, and Ken Bray. Partially premixed flamelets in les of nonpremixed turbulent combustion. *Combustion Theory and Modelling*, 6(4):529–551, 2002.

[23] A Yu Klimenko and SB Pope. The modeling of turbulent reactive flows

based on multiple mapping conditioning. *Physics of Fluids (1994-present)*, 15(7):1907–1925, 2003.

[24] Kenneth K Kuo. Principles of combustion. 1986.

[25] S Balachandar. A scaling analysis for point–particle approaches to turbulent multiphase flows. *International Journal of Multiphase Flow*, 35(9):801–810, 2009.

[26] Romain Monchaux, Mickael Bourgoin, and Alain Cartellier. Analyzing preferential concentration and clustering of inertial particles in turbulence. *International Journal of Multiphase Flow*, 40:1–18, 2012.

[27] Jun Xia, Hua Zhao, Athanasios Megaritis, Kai H Luo, Alasdair Cairns, and Lionel C Ganippa. Inert-droplet and combustion effects on turbulence in a diluted diffusion flame. *Combustion and Flame*, 160(2):366–383, 2013.

[28] CT Crowe, TR Troutt, and JN Chung. Numerical models for two-phase turbulent flows. *Annual Review of Fluid Mechanics*, 28(1):11–43, 1996.

[29] Robert W Bilger. A mixture fraction framework for the theory and modeling of droplets and sprays. *Combustion and Flame*, 158(2):191–202, 2011.

[30] Patrick Jenny, Dirk Roekaerts, and Nijso Beishuizen. Modeling of turbulent dilute spray combustion. *Progress in Energy and Combustion Science*, 38(6):846–887, 2012.

[31] HH Chiu and TM Liu. Group combustion of liquid droplets. *Combustion Science and Technology*, 17(3-4):127–142, 1977.

[32] Huei-Huang Chiu. Mesoscale structures of turbulent sprays. *Proceedings of the Combustion Institute*, 28(1):1095–1102, 2000.

[33] MRG Zoby, S Navarro-Martinez, A Kronenburg, and AJ Marquis. Evaporation rates of droplet arrays in turbulent reacting flows. *Proceedings of the Combustion Institute*, 33(2):2117–2125, 2011.

[34] Mariko Nakamura, Fumiteru Akamatsu, Ryoichi Kurose, and Masashi Katsuki. Combustion mechanism of liquid fuel spray in a gaseous flame. *Physics of Fluids (1994-present)*, 17(12):123301, 2005.

[35] Akira Umemura and Shoichi Takamori. Percolation theory for flame propagation in non-or less-volatile fuel spray: A conceptual analysis to group combustion excitation mechanism. *Combustion and flame*, 141(4):336–349, 2005.

[36] D Brian Spalding. Development of the eddy-break-up model of turbulent combustion. In *Symposium (International) on Combustion*, volume 16, pages 1657–1663. Elsevier, 1977.

[37] Bjørn F Magnussen and Bjørn H Hjertager. On mathematical modeling of turbulent combustion with special emphasis on soot formation and combustion. In *Symposium (International) on Combustion*, volume 16, pages 719–729. Elsevier, 1977.

[38] RS Cant and Epaminondas Mastorakos. *An introduction to turbulent reacting flows*. Imperial College Press, 2008.

[39] SP Burke and TEW Schumann. Diffusion flames. *Industrial & Engineering Chemistry*, 20(10):998–1004, 1928.

[40] A Kempf, H Forkel, J-Y Chen, A Sadiki, and J Janicka. Large-eddy simulation of a counterflow configuration with and without combustion. *Proceedings of the Combustion Institute*, 28(1):35–40, 2000.

[41] Norbert Peters. Local quenching due to flame stretch and non-premixed turbulent combustion. *Combustion Science and Technology*, 30(1-6):1–17, 1983.

[42] Valérie Favier and Luc Vervisch. Edge flames and partially premixed combustion in diffusion flame quenching. *Combustion and flame*, 125(1):788–803, 2001.

[43] H Pitsch. Improved pollutant predictions in large-eddy simulations of turbulent non-premixed combustion by considering scalar dissipation rate fluctuations. *Proceedings of the Combustion Institute*, 29(2):1971–1978, 2002.

[44] RW Bilger. The structure of turbulent nonpremixed flames. In *Symposium (International) on Combustion*, volume 22, pages 475–488. Elsevier, 1989.

[45] A Yu Klimenko. Multicomponent diffusion of various admixtures in turbulent flow. *Fluid Dynamics*, 25(3):327–334, 1990.

[46] RW Bilger. Conditional moment closure for turbulent reacting flow. *Physics of Fluids A: Fluid Dynamics (1989-1993)*, 5(2):436–444, 1993.

[47] Alex Y Klimenko and Robert William Bilger. Conditional moment closure for turbulent combustion. *Progress in energy and combustion science*, 25(6):595–687, 1999.

[48] RW Bilger, LR Saetran, and LV Krishnamoorthy. Reaction in a scalar mixing layer. *Journal of Fluid Mechanics*, 233:211–242, 1991.

[49] IS Kim and E Mastorakos. Simulations of turbulent non-premixed counterflow flames with first-order conditional moment closure. *Flow, Turbulence and Combustion*, 76(2):133–162, 2006.

[50] MR Roomina and RW Bilger. Conditional moment closure modelling of turbulent methanol jet flames. *Combustion Theory and Modelling*, 3(4):689–708, 1999.

[51] NSA Smith, RW Bilger, CD Carter, RS Barlow, and J-Y Chen. A comparison of cmc and pdf modelling predictions with experimental nitric oxide lif/raman measurements in a turbulent h2 jet flame. *Combustion science and technology*, 105(4-6):357–375, 1995.

[52] MR Roomina and RW Bilger. Conditional moment closure (cmc) predictions of a turbulent methane-air jet flame. *Combustion and flame*, 125(3):1176–1195, 2001.

[53] A Kronenburg, RW Bilger, and JH Kent. Second-order conditional moment closure for turbulent jet diffusion flames. In *Symposium (International) on Combustion*, volume 27, pages 1097–1104. Elsevier, 1998.

[54] A Kronenburg. Double conditioning of reactive scalar transport equations in turbulent nonpremixed flames. *Physics of Fluids (1994-present)*, 16(7):2640–2648, 2004.

[55] Chong M Cha, George Kosály, and Heinz Pitsch. Modeling extinction and reignition in turbulent nonpremixed combustion using a doubly-conditional

moment closure approach. *Physics of Fluids (1994-present)*, 13(12):3824–3834, 2001.

[56] A Kronenburg and AE Papoutsakis. Conditional moment closure modeling of extinction and re-ignition in turbulent non-premixed flames. *Proceedings of the Combustion Institute*, 30(1):759–766, 2005.

[57] César Dopazo and Edward E OBRIEN. Functional formulation of nonisothermal turbulent reactive flows. *Physics of Fluids*, 17(11):1968, 1974.

[58] César Dopazo and Edward E O'Brien. An approach to the autoignition of a turbulent mixture. *Acta Astronautica*, 1(9):1239–1266, 1974.

[59] Stephen B Pope. Pdf methods for turbulent reactive flows. *Progress in Energy and Combustion Science*, 11(2):119–192, 1985.

[60] AY Klimenko and Matthew J Cleary. Convergence to a model in sparse-lagrangian fdf simulations. *Flow, turbulence and combustion*, 85(3-4):567–591, 2010.

[61] Venkatramanan Raman, Heinz Pitsch, and Rodney O Fox. Hybrid large-eddy simulation/lagrangian filtered-density-function approach for simulating turbulent combustion. *Combustion and Flame*, 143(1):56–78, 2005.

[62] SB Pope. The probability approach to the modelling of turbulent reacting flows. *Combustion and Flame*, 27:299–312, 1976.

[63] Stephen Bailey Pope. A monte carlo method for the pdf equations of turbulent reactive flow. 1981.

[64] Robert Barlow and J Frank. Sandia/tud piloted ch4/air jet flames. *Sandia National Laboratories, Livermore, CA, http://www. sandia. gov/TNF/DataArch/FlameD. html*, 2003.

[65] Jun Xu and Stephen B Pope. Pdf calculations of turbulent nonpremixed flames with local extinction. *Combustion and Flame*, 123(3):281–307, 2000.

[66] J Janicka, W Kolbe, and W Kollmann. Closure of the transport equation for the probability density funcfion of turbulent scalar fields. *Journal of Non-Equilibrium Thermodynamics*, 4(1):47–66, 1979.

[67] S Subramaniam and SB Pope. A mixing model for turbulent reactive flows based on euclidean minimum spanning trees. *Combustion and Flame*, 115(4):487–514, 1998.

[68] S Subramaniam and SB Pope. Comparison of mixing model performance for nonpremixed turbulent reactive flow. *Combustion and Flame*, 117(4):732–754, 1999.

[69] BB Dally, DF Fletcher, and AR Masri. Flow and mixing fields of turbulent bluff-body jets and flames. *Combustion Theory and Modelling*, 2(2):193–219, 1998.

[70] AR Masri, SB Pope, and BB Dally. Probability density function computations of a strongly swirling nonpremixed flame stabilized on a new burner. *Proceedings of the Combustion Institute*, 28(1):123–131, 2000.

[71] DC Haworth. Progress in probability density function methods for turbulent reacting flows. *Progress in Energy and Combustion Science*, 36(2):168–259, 2010.

[72] Hudong Chen, Shiyi Chen, and Robert H Kraichnan. Probability distribution of a stochastically advected scalar field. *Physical review letters*, 63(24):2657, 1989.

[73] SB Pope. Mapping closures for turbulent mixing and reaction. *Theoretical and Computational Fluid Dynamics*, 2(5-6):255–270, 1991.

[74] MJ Cleary and A Kronenburg. Multiple mapping conditioning for extinction and reignition in turbulent diffusion flames. *Proceedings of the Combustion Institute*, 31(1):1497–1505, 2007.

[75] MJ Cleary and Alexander Y Klimenko. A generalised multiple mapping conditioning approach for turbulent combustion. *Flow, turbulence and combustion*, 82(4):477–491, 2009.

[76] MJ Cleary, AY Klimenko, J Janicka, and M Pfitzner. A sparse-lagrangian multiple mapping conditioning model for turbulent diffusion flames. *Proceedings of the Combustion Institute*, 32(1):1499–1507, 2009.

[77] A Kronenburg and MJ Cleary. Multiple mapping conditioning for flames with partial premixing. *Combustion and Flame*, 155(1):215–231, 2008.

[78] K Vogiatzaki, A Kronenburg, MJ Cleary, and JH Kent. Multiple mapping conditioning of turbulent jet diffusion flames. *Proceedings of the Combustion Institute*, 32(2):1679–1685, 2009.

[79] K Vogiatzaki, MJ Cleary, A Kronenburg, and JH Kent. Modeling of scalar mixing in turbulent jet flames by multiple mapping conditioning. *Physics of Fluids (1994-present)*, 21(2):025105, 2009.

[80] Andrew P Wandel and Alexander Y Klimenko. Testing multiple mapping conditioning mixing for monte carlo probability density function simulations. *Physics of Fluids (1994-present)*, 17(12):128105, 2005.

[81] Andrew P Wandel and R Peter Lindstedt. Hybrid binomial langevin-multiple mapping conditioning modeling of a reacting mixing layer. *Physics of Fluids (1994-present)*, 21(1):015103, 2009.

[82] AY Klimenko. Matching conditional moments in pdf modelling of nonpremixed combustion. *Combustion and flame*, 143(4):369–385, 2005.

[83] AY Klimenko. On simulating scalar transport by mixing between lagrangian particles. *Physics of Fluids*, 19(3):031702, 2007.

[84] Dudley Brian Spalding. *Some fundamentals of combustion*, volume 2. Academic Press, 1955.

[85] M Bini and WP Jones. Large eddy simulation of an evaporating acetone spray. *International Journal of Heat and Fluid Flow*, 30(3):471–480, 2009.

[86] S Ukai, A Kronenburg, and OT Stein. Large eddy simulation of dilute acetone spray flames using cmc coupled with tabulated chemistry. *Proceedings of the Combustion Institute*, 35(2):1667–1674, 2015.

[87] GF Carrier. Shock waves in a dusty gas. *Journal of Fluid Mechanics*, 4(04):376–382, 1958.

[88] Frank E Marble. Dynamics of dusty gases. *Annual Review of Fluid Mechanics*, 2(1):397–446, 1970.

[89] Jim Ferry and S Balachandar. A fast eulerian method for disperse two-phase flow. *International journal of multiphase flow*, 27(7):1199–1226, 2001.

[90] MW Reeks. The transport of discrete particles in inhomogeneous turbulence. *Journal of aerosol science*, 14(6):729–739, 1983.

[91] Jim Ferry and S Balachandar. Equilibrium expansion for the eulerian velocity of small particles. *Powder Technology*, 125(2):131–139, 2002.

[92] CT Crowe, M Sommerfeld, and Y Tsuji. Multiphase flows with particles and droplets, 1998.

[93] OA Druzhinin and S Elghobashi. Direct numerical simulations of bubble-laden turbulent flows using the two-fluid formulation. *Physics of Fluids*, 10(3):685–697, 1998.

[94] Pierre Fevrier, Olivier Simonin, and Kyle D Squires. Partitioning of particle velocities in gas–solid turbulent flows into a continuous field and a spatially uncorrelated random distribution: theoretical formalism and numerical study. *Journal of Fluid Mechanics*, 533:1–46, 2005.

[95] Rodney O Fox, Frédérique Laurent, and Marc Massot. Numerical simulation of spray coalescence in an eulerian framework: direct quadrature method of moments

and multi-fluid method. *Journal of Computational Physics*, 227(6):3058–3088, 2008.

[96] S Elghobashi. Particle-laden turbulent flows: direct simulation and closure models. *Applied Scientific Research*, 48(3-4):301–314, 1991.

[97] James J Riley and GS Patterson Jr. Diffusion experiments with numerically integrated isotropic turbulence. *The Physics of Fluids*, 17(2):292–297, 1974.

[98] Kyle D Squires and John K Eaton. Particle response and turbulence modification in isotropic turbulence. *Physics of Fluids A: Fluid Dynamics*, 2(7):1191–1203, 1990.

[99] MR Maxey. The gravitational settling of aerosol particles in homogeneous turbulence and random flow fields. *Journal of Fluid Mechanics*, 174:441–465, 1987.

[100] Kyle D Squires and John K Eaton. Preferential concentration of particles by turbulence. *Physics of Fluids A: Fluid Dynamics (1989-1993)*, 3(5):1169–1178, 1991.

[101] S Elghobashi and GC Truesdell. On the two-way interaction between homogeneous turbulence and dispersed solid particles. i: Turbulence modification. *Physics of Fluids A: Fluid Dynamics (1989-1993)*, 5(7):1790–1801, 1993.

[102] Antonino Ferrante and Said Elghobashi. On the physical mechanisms of two-way coupling in particle-laden isotropic turbulence. *Physics of Fluids (1994-present)*, 15(2):315–329, 2003.

[103] John R Fessler, Jonathan D Kulick, and John K Eaton. Preferential concentration of heavy particles in a turbulent channel flow. *Physics of Fluids (1994-present)*, 6(11):3742–3749, 1994.

[104] Patrick C Le Clercq and Josette Bellan. Direct numerical simulation of gaseous mixing layers laden with multicomponent-liquid drops: liquid-specific effects. *Journal of Fluid Mechanics*, 533:57–94, 2005.

[105] Julien Reveillon and Luc Vervisch. Analysis of weakly turbulent dilute-spray flames and spray combustion regimes. *Journal of Fluid Mechanics*, 537:317–347, 2005.

[106] Andrew P Wandel, Nilanjan Chakraborty, and E Mastorakos. Direct numerical simulations of turbulent flame expansion in fine sprays. *Proceedings of the Combustion Institute*, 32(2):2283–2290, 2009.

[107] K Luo, H Pitsch, MG Pai, and O Desjardins. Direct numerical simulations and analysis of three-dimensional n-heptane spray flames in a model swirl combustor. *Proceedings of the Combustion Institute*, 33(2):2143–2152, 2011.

[108] Giulio Borghesi, Epaminondas Mastorakos, and R Stewart Cant. Complex chemistry dns of n-heptane spray autoignition at high pressure and intermediate temperature conditions. *Combustion and Flame*, 160(7):1254–1275, 2013.

[109] Suresh Menon and Nayan Patel. Subgrid modeling for simulation of spray combustion in large-scale combustors. *AIAA journal*, 44(4):709–723, 2006.

[110] Parviz Moin and Sourabh V Apte. Large-eddy simulation of realistic gas turbine combustors. *AIAA journal*, 44(4):698–708, 2006.

[111] WP Jones, AJ Marquis, and K Vogiatzaki. Large-eddy simulation of spray combustion in a gas turbine combustor. *Combustion and Flame*, 161(1):222–239, 2014.

[112] M Bini and WP Jones. Particle acceleration in turbulent flows: A class of nonlinear stochastic models for intermittency. *Physics of Fluids (1994-present)*, 19(3):035104, 2007.

[113] WP Jones, S Lyra, and S Navarro-Martinez. Numerical investigation of swirling kerosene spray flames using large eddy simulation. *Combustion and Flame*, 159(4):1539–1561, 2012.

[114] Jacek Pozorski and Sourabh V Apte. Filtered particle tracking in isotropic turbulence and stochastic modeling of subgrid-scale dispersion. *International Journal of Multiphase Flow*, 35(2):118–128, 2009.

[115] E Loth. Numerical approaches for motion of dispersed particles, droplets and bubbles. *Progress in Energy and Combustion Science*, 26(3):161–223, 2000.

[116] TL Bocksell and E Loth. Stochastic modeling of particle diffusion in a turbulent boundary layer. *International journal of multiphase flow*, 32(10):1234–1253, 2006.

[117] Santanu De, KN Lakshmisha, and Robert W Bilger. Modeling of nonreacting and reacting turbulent spray jets using a fully stochastic separated flow approach. *Combustion and Flame*, 158(10):1992–2008, 2011.

[118] Santanu De and Seung Hyun Kim. Large eddy simulation of dilute reacting sprays: Droplet evaporation and scalar mixing. *Combustion and Flame*, 160(10):2048–2066, 2013.

[119] Stephen B Pope. Turbulent flows, 2001.

[120] RO Fox. Computational methods for turbulent reacting flows, 2003.

[121] S Balachandar and John K Eaton. Turbulent dispersed multiphase flow. *Annual Review of Fluid Mechanics*, 42:111–133, 2010.

[122] Prosenjit Bagchi and S Balachandar. Response of the wake of an isolated particle to an isotropic turbulent flow. *Journal of Fluid Mechanics*, 518:95–123, 2004.

[123] Tristan M Burton and John K Eaton. Fully resolved simulations of particle-turbulence interaction. *Journal of Fluid Mechanics*, 545:67–111, 2005.

[124] R Stauch and U Maas. The ignition of methanol droplets in a laminar convective environment. *Combustion and Flame*, 153(1):45–57, 2008.

[125] MRG Zoby, S Navarro-Martinez, A Kronenburg, and AJ Marquis. Turbulent mixing in three-dimensional droplet arrays. *International Journal of Heat and Fluid Flow*, 32(3):499–509, 2011.

[126] Randall T Imaoka and William A Sirignano. Vaporization and combustion in three-dimensional droplet arrays. *Proceedings of the Combustion Institute*, 30(2):1981–1989, 2005.

[127] Takeo Kajishima, Satoshi Takiguchi, Hiroyuki Hamasaki, and Yutaka Miyake. Turbulence structure of particle-laden flow in a vertical plane channel due to vortex

shedding. *JSME International Journal Series B Fluids and Thermal Engineering*, 44(4):526–535, 2001.

[128] Jiacai Lu and Gretar Tryggvason. Numerical study of turbulent bubbly downflows in a vertical channel. *Physics of Fluids (1994-present)*, 18(10):103302, 2006.

[129] Y Pan and S Banerjee. Numerical investigation of the effects of large particles on wall-turbulence. *Physics of Fluids (1994-present)*, 9(12):3786–3807, 1997.

[130] John K Dukowicz. A particle-fluid numerical model for liquid sprays. *Journal of Computational Physics*, 35(2):229–253, 1980.

[131] BM Franchetti, F Cavallo Marincola, S Navarro-Martinez, and AM Kempf. Large eddy simulation of a pulverised coal jet flame. *Proceedings of the Combustion Institute*, 34(2):2419–2426, 2013.

[132] MC Yuen and LW Chen. On drag of evaporating liquid droplets. 1976.

[133] Dudley Brian Spalding. The combustion of liquid fuels. In *Symposium (international) on combustion*, volume 4, pages 847–864. Elsevier, 1953.

[134] WE Ranz and WR Marshall. Evaporation from drops. *Chemical Engineering Progress*, 48(3):141446, 1952.

[135] Y. Ge, M.J. Cleary, and A.Y. Klimenko. A comparative study of sandia flame series (dâĂŞf) using sparse-lagrangian {MMC} modelling. *Proceedings of the Combustion Institute*, 34(1):1325 – 1332, 2013.

[136] S Ukai, A Kronenburg, and OT Stein. Les-cmc of a dilute acetone spray flame. *Proceedings of the Combustion Institute*, 34(1):1643–1650, 2013.

[137] Hiroshi Nomura, Yasushige Ujiie, Hans J Rath, Jun'ich Sato, and Michikata Kono. Experimental study on high-pressure droplet evaporation using microgravity conditions. In *Symposium (International) on Combustion*, volume 26, pages 1267–1273. Elsevier, 1996.

[138] Daniel L Dietrich, JB Haggard, Frederick L Dryer, Vedha Nayagam, Benjamin D Shaw, and Forman A Williams. Droplet combustion experiments in spacelab. In *Symposium (International) on Combustion*, volume 26, pages 1201–1207. Elsevier, 1996.

[139] DG Goodwin and DG Cantera. Object-oriented software for reacting flows, 2002.

[140] BJ McBride, S Gordon, and MA Reno. Coefficients for calculating thermodynamic and transport properties of individual species, nasa, report no. *TM-4513*, 1993.

[141] Isao Kataoka. Local instant formulation of two-phase flow. *International Journal of Multiphase Flow*, 12(5):745–758, 1986.

[142] Mikael Mortensen and Robert W Bilger. Derivation of the conditional moment closure equations for spray combustion. *Combustion and Flame*, 156(1):62–72, 2009.

[143] Joseph Smagorinsky. General circulation experiments with the primitive equations: I. the basic experiment*. *Monthly weather review*, 91(3):99–164, 1963.

[144] Massimo Germano, Ugo Piomelli, Parviz Moin, and William H Cabot. A dynamic subgrid-scale eddy viscosity model. *Physics of Fluids A: Fluid Dynamics (1989-1993)*, 3(7):1760–1765, 1991.

[145] Clayton T Crowe, M Pt Sharma, and David E Stock. The particle-source-in cell (psi-cell) model for gas-droplet flows. *Journal of Fluids Engineering*, 99(2):325–332, 1977.

[146] Giulio Borghesi, Epaminondas Mastorakos, Cécile B Devaud, and Robert W Bilger. Modeling evaporation effects in conditional moment closure for spray autoignition. *Combustion Theory and Modelling*, 15(5):725–752, 2011.

[147] Colin Heye, Venkat Raman, and Assaad R Masri. Les/probability density function approach for the simulation of an ethanol spray flame. *Proceedings of the Combustion Institute*, 34(1):1633–1641, 2013.

[148] S James, MS Anand, and SB Pope. The lagrangian pdf transport method for simulations of gas turbine combustor flows. *AIAA Paper (2002-4017)*, 2002.

[149] Michael Stöllinger, Bertrand Naud, Dirk Roekaerts, Nijso Beishuizen, and Stefan Heinz. Pdf modeling and simulations of pulverized coal combustion–part 1: Theory and modeling. *Combustion and Flame*, 160(2):384–395, 2013.

[150] Michael Stöllinger, Bertrand Naud, Dirk Roekaerts, Nijso Beishuizen, and Stefan Heinz. Pdf modeling and simulations of pulverized coal combustion–part 2: Application. *Combustion and Flame*, 160(2):396–410, 2013.

[151] RL Curl. Dispersed phase mixing: I. theory and effects in simple reactors. *AIChE journal*, 9(2):175–181, 1963.

[152] K_R Sreenivasan. Fractals and multifractals in fluid turbulence. *Annual Review of Fluid Mechanics*, 23(1):539–604, 1991.

[153] Jerome H Friedman, Jon Louis Bentley, and Raphael Ari Finkel. An algorithm for finding best matches in logarithmic expected time. *ACM Transactions on Mathematical Software (TOMS)*, 3(3):209–226, 1977.

[154] Metin Muradoglu, Stephen B Pope, and David A Caughey. The hybrid method for the pdf equations of turbulent reactive flows: consistency conditions and correction algorithms. *Journal of Computational Physics*, 172(2):841–878, 2001.

[155] AR Masri and JD Gounder. Turbulent spray flames of acetone and ethanol approaching extinction. *Combustion Science and Technology*, 182(4-6):702–715, 2010.

[156] M Klein, A Sadiki, and J Janicka. A digital filter based generation of inflow data for spatially developing direct numerical or large eddy simulations. *Journal of computational Physics*, 186(2):652–665, 2003.

[157] S Pichon, G Black, N Chaumeix, M Yahyaoui, JM Simmie, HJ Curran, and R Donohue. The combustion chemistry of a fuel tracer: Measured flame speeds and ignition delays and a detailed chemical kinetic model for the oxidation of acetone. *Combustion and Flame*, 156(2):494–504, 2009.

[158] Cheng Tung Chong and Simone Hochgreb. Measurements of laminar flame speeds of acetone/methane/air mixtures. *Combustion and Flame*, 158(3):490–500, 2011.

[159] A Sandu, JG Verwer, JG Blom, EJ Spee, GR Carmichael, and FA Potra. Benchmarking stiff ode solvers for atmospheric chemistry problems ii: Rosenbrock solvers. *Atmospheric environment*, 31(20):3459–3472, 1997.

[160] F Salehi, MJ Cleary, AR Masri, Y Ge, and AY Klimenko. Sparse-lagrangian mmc simulations of an n-dodecane jet at engine-relevant conditions. *Proceedings of the Combustion Institute*, 2016.

[161] Adriaan Daniël Fokker. Die mittlere energie rotierender elektrischer dipole im strahlungsfeld. *Annalen der Physik*, 348(5):810–820, 1914.

[162] Max Planck. *Über einen Satz der statistischen Dynamik und seine Erweiterung in der Quantentheorie*. Reimer, 1917.

[163] James William Thomas. *Numerical partial differential equations: finite difference methods*, volume 22. Springer Science & Business Media, 2013.

[164] Son Vo, OT Stein, A Kronenburg, and MJ Cleary. Assessment of mixing time scales for a sparse particle method. *Combustion and Flame*, 179:280–299, 2017.

[165] Colin Heye, Venkat Raman, and Assaad R Masri. Influence of spray/combustion interactions on auto-ignition of methanol spray flames. *Proceedings of the Combustion Institute*, 35(2):1639–1648, 2015.